UNIVERSITY OF OKLAHOMA

GRADUATE COLLEGE

EVOLUTION OF BIOMASS BURNING AEROSOL PROPERTIES DURING TRANSPORT IN THE SOUTHEAST ATLANTIC REGION

A THESIS

SUBMITTED TO THE GRADUATE FACULTY

in partial fulfillment of the requirements for the

Degree of

MASTER OF SCIENCE

By

ABDULAMID FAKOYA

Norman, Oklahoma

2023

Downloaded from SHAREOK. Persistent Handle URL: https://hdl.handle.net/11244/337650

EVOLUTION OF BIOMASS BURNING AEROSOL PROPERTIES
DURING TRANSPORT IN THE SOUTHEAST ATLANTIC REGION

A THESIS APPROVED FOR THE
SCHOOL OF METEOROLOGY

BY THE COMMITTEE CONSISTING OF

Dr. Jens Redemann, Chair

Dr. Marcela Loria-Salazar

Dr. Connor Flynn

© Copyright by ABDULAMID FAKOYA 2023

All Rights Reserved.

Acknowledgment

My first expression of gratitude goes to Dr. Jens Redemann, my academic advisor and thesis committee chair, whose mentorship, scientific expertise, and consistent support have been pivotal to my research success. His meticulous attention to detail, insightful comments, and constructive feedback have played an integral role in shaping the direction and scope of my research.

My profound gratitude extends to the members of my thesis committee, Dr. Marcela S. Loria-Salazar, who have made invaluable contributions to my research endeavors and Dr. Connor J. Flynn, whose expertise, critiques, and suggestions have been instrumental in shaping my research questions, methodology, and analysis, and have inspired me to push the boundaries of scientific inquiry.

I would like to express my appreciation to collaborators, Dr. Pablo E. Saide, Calvin Howes, and the Weather Research and Forecasting (WRF) team at UCLA for generously providing resources utilized in this thesis. My sincere thanks also go to Dr. Lan Gao for providing the codes that formed the basis of the model-observation comparison and Dr. Ian Chang for the collaborative opportunity that has broadened my scientific horizons and allowed me to refine my analytical skills.

Furthermore, I must thank my colleagues in the CLoud CLimatE Aerosol Radiation (CL2EAR) research group with whom I have had the privilege to collaborate. Their constructive feedback and encouragement have been integral to my scientific accomplishments, strengthening my research skills, and broadening my scientific perspectives.

I would like to acknowledge the internal funding through the graduate research assistantship at the University of Oklahoma and the OU Scholarship Office for their support throughout this journey. I would also like to acknowledge the faculty and staff members at the OU School of Meteorology who have provided me with a stimulating academic environment that has instilled in me a sense of dedication and enthusiasm towards scientific research.

Lastly, I wish to express my heartfelt appreciation for the unwavering support, love, and encouragement given to me by my family and friends as I pursue my graduate studies. Their presence in my life has been a constant source of motivation and inspiration, and I am indebted for their understanding and patience during my thesis research.

The contributions of this community of scientists, mentors, colleagues and loved ones to my life and career are something for which I will forever be grateful.

Dedication

- *To my mom*

List of Tables

Table 1: Summary of ORACLES science questions and specific objectives……22

Table 2: Site information for AERONET stations used in this study……29

Table 3: Mean SSA values from model and observation for AERONET and 4STAR…….48

Table 4: Summary of the statistics of model-observation comparison……..48

List of Figures

Figure 1.1: Different sources of atmospheric aerosols. top: biomass burning, dust storm, industrial plant. Bottom: vehicular emissions, sea spray, domestic cooking……3

Figure 1.2: The average annual Earth's energy budget (adapted from Trenberth et al., 2009)……7

Figure 1.3: An overview of the aerosol-radiation interactions showing the impact of non-absorbing (a, b) and absorbing (c, d) aerosols. Graphics from Chapter 7; Clouds and Aerosols, IPCC AR5 (Boucher et al., 2013)……...9

Figure 1.4: An overview of aerosol-cloud interactions (ACI), showing how they affect climate. (a) shows a clean low-level cloud, (b) shows a polluted low-level cloud. Figure adapted from Boucher et al. (2013) (Chapter 7; Clouds and Aerosols, IPCC AR5 report)…..……...12

Figure 1.5: Change in effective radiative forcing by climate drivers, showing contributions from aerosol-radiation interactions and aerosol-cloud interactions. From Forster et al. (2021) (Fig 7.6, Chapter 7, IPCC AR6 report)…….13

Figure 1.6: (a): Map of the SEA region showing the wind vectors following BBA transport. Adapted from Zuidema et al., 2016 (b): Illustration of the activities in the SEA, showing aerosol-radiation, aerosol-cloud interactions as well as the schematic of observational instruments used in the ObseRvations of Aerosols above CLouds and their intEractionS (ORACLES) mission……...……19

Figure 1.7: Overview of SEA region showing the international field missions and the study area of the ORACLES deployments. AERONET sites are indicated with letter A and the red dots are showing active fires from NASA VIIRS (Redemann et al., 2021)……21

Figure 1.8: ORACLES flight tracks (2016 ER-2 in green, 2016 P-3 in red, 2017 P-3 in orange, 2018 P-3 in blue) overlaying the Sc cloud deck over the study area. The deployment base for 2016 is labeled as Walvis Bay and for 2017 and 2018 as São Tomé (Redemann et al., 2021)…..…….23

Figure 1.9: Lifecycle of BBA showing the controls on particle properties on different time scales. Figure by Tiffany Bowman. Adapted from Sedlacek et al., (2022)……..25

Figure 2.1: A typical CIMEL Electronique CE-318 sun photometer used in the AERONET mission. (Image credit: Dong, 2020)…….30

Figure 2.2: Location of AErosol RObotics NETwork (AERONET) stations used in this study. Adapted from Google Earth……...30

Figure 2.3. The Spectrometer for Sky Scanning Sun-Tracking Atmospheric Research (4STAR): Schematic and components (left), Physical look (right)……33

Figure 2.4: Collocation of the model outputs with AERONET and 4STAR observations……...40

Figure 3.1(a): Statistical summary and comparison of model-derived against observation SSA for the entire ORACLES campaign…….46

Figure 3.1(b): The longitudinal dependence of modeled SSA from all AERONET station……46

Figure 3.2: Scatterplot and histogram showing the comparison of WRF-CAM5 SSA against (a) AEROENT SSA and (b) 4STAR SSA for the entire ORACLES campaign…….47

Figure 3.3(a): WRF-AAM curtain plot showing the mean plume age forecast (shading) along the P-3 flight track (red line) for October 17, 2018. Figure credit: Pablo Saide …….49

Figure 3.3(b): WRF-AAM curtain plot showing the extinction forecast (shading) along the P-3 flight track (red line) for October 17, 2018. Figure credit: Pablo Saide…….49

Figure 3.4: Map of the SEA region, showing the extinction-weighted aerosol age at Ascension Island and individual 4STAR sky scans during the three ORACLES deployments…….50

Figure 3.5: Statistics of the extinction-weighted aerosol age for all data points used in this study..51

Figure 3.6: Scatterplot showing the relationship between SSA (markers), EAE (shading), and aerosol age in the total atmospheric column (TC)…….52

Figure 3.7: The evolution of SSA with age in the total column (TC), filtered with (a) EAE >= 0.75, (b) EAE >= 1, (c) EAE >= 1.2, (d) EAE >= 1.4……..54

Figure 3.8: The mean total column TC SSA for all age bins across the four thresholds……55

Figure 3.9: Model-derived fraction of FT AOD to TC AOD from WRF-AAM. A fraction of 1 means that aerosol loading is completely in the FT……56

Figure 3.10: Map showing the FT AOD over the SEA region. All individual 4STAR sky scans are shown while the mean aerosol age is represented for Ascension Island……57

Figure 3.11: Comparison of EAE in the total column (TC) and free troposphere (FT) over the southeast Atlantic (SEA)……58

Figure 3.12: Scatterplot showing the relationship between SSA (markers), EAE (shading), and aerosol age in the free troposphere (FT)……59

Figure 3.13: The evolution of SSA with age in the free troposphere (FT), filtered with (a) EAE >= 0.75, (b) EAE >= 1, (c) EAE >= 1.2, (d) EAE >= 1.4……60

Figure 3.14: The mean free tropospheric FT SSA for all age bins across the four thresholds……61

Table of Contents

Acknowledgement...……**iv**

Dedication……**vi**

List of Tables ..…….....**vii**

List of Figures ……...**viii**

Abstract.....**xii**

Chapter 1 – Introduction.……...……**1**

1.1 – Sources and Emission of Aerosols……...2

1.2 – Absorbing and Non-absorbing Aerosols……..4

1.3 – Aerosol & Climate……7

1.3.1 – Aerosol-Radiation Interactions (ARI); Direct and Semi-Direct Effects……8

1.3.2 – Aerosol-Cloud Interactions (ACI); Indirect Effects……..11

1.4 – Aerosol Properties; Physical, Chemical, and Optical Properties……..14

1.4.1 – Physical Properties of Aerosols .....……..14

1.4.2 – Chemical Properties of Aerosols....……...14

1.4.3 – Optical and Radiative Properties. . . .. .15

1.5 – Southern Africa BB Season and the Southeast Atlantic Climate System ……..... . . . …18

1.6 – ORACLES - ObseRvations of Aerosols above CLouds and their intEractionS..……22

1.7 - Motivation and Thesis Statement …….24

Chapter 2 – Data and Methods……..**27**

2.1 – Instruments and Data Sources……..27

2.1.1 – AErosol RObotics NETwork (AERONET)……..27

2.1.2 – 4STAR……..31

2.2 – Weather Research and Forecasting (WRF) Model Output……..34

2.2.1 – WRF-CAM5: Concept and Configuration……34

2.2.2 – WRF-AAM……36

2.3 – Plume Age Derivation……..37

2.4 – Collocation and Analysis……..39

2.5 – Boundary Layer (BL) and Free Troposphere (FT) Partitioning……...42

2.6 – Extinction Ångstrom Exponent (EAE) Thresholds……..44

Chapter 3 – Results ……**45**

3.1 – Model Representation of Single Scattering Albedo…….45

3.2 – Estimates of Biomass Burning Aerosol Age……49

3.3 – Evolution of Biomass Burning Aerosols Single Scattering Albedo (SSA) with Age……..52

3.3.1 – Attempts to separate BL contributions from TC observations……..53

3.3.2 – Application of EAE thresholds……..53

3.3.2 – Applying model partition ratio to vertically resolved observations …….....56

Chapter 4 – Discussion ..… ... …….. … ….……..**62**

4.1 – Discussion; Model Representation of Single Scattering Albedo ...……...……62

4.2 – Discussion; Estimates of Biomass Burning Aerosol Age … ..…… 65

4.3 – Discussion; Evolution of Biomass Burning Aerosols Single Scattering Albedo (SSA) with Age ……..…..67

4.3.1 – Attempts to separate BL contributions from TC observations ..……...68

4.4 – Conclusion …..……..……72

4.5 – Future Work …….……....75

References……..……..…**77**

Abstract

Biomass burning (BB) is a major source of absorbing aerosols globally and accounts for about 40% of black carbon in the atmosphere. The Southern African region contributes approximately 35% of the planet's BB aerosol emissions. During the austral winter and spring, smoke is transported westward towards the southeast Atlantic Ocean, where it overlies and interacts with a quasi-permanent stratocumulus (Sc) cloud deck. Aerosol-cloud-climate interactions contribute the largest uncertainty to model estimates of anthropogenic forcing. The SEA region thus exhibits a large model-to-model divergence of climate forcing due to aerosols. This makes studies in the region particularly valuable for understanding these interactions. Previous studies focusing on Southern Africa BB have explored the distribution of aerosol loading. However, changes in aerosol optical properties during transport are not well documented.

This study aims to use remotely sensed observations to investigate the evolution of BB aerosol optical properties after emission within continental Africa, during transport over land, and over the Atlantic Ocean. Measurements taken from a collection of remote-sensing instruments during the ORACLES campaign are combined with results from two regional models, the WRF-AAM and WRF-CAM5, to explore the changes in the optical properties of smoke plumes as they age. The aerosol age is modeled using tracers from the WRF-AAM configured over the region's spatial domain (14 ºN – 41 ºS, 34 ºW – 51 ºE). The study conducted an analysis of extinction, single scattering albedo (SSA), and extinction Angstrom exponent (EAE) in relation to aerosol age. Additionally, observations from airborne 4STAR, ground-based AERONET were compared with model results using WRF-CAM5.

The analysis revealed that aerosol age varied distinctly with longitude and the physical and chemical processes associated with the transport drive changes in the optical properties. The aerosols sampled closest to the source exhibited lower SSA values relative to particles sampled along the coastline. Along the coastline, free tropospheric SSA peaked at about 5-6 days, before gradually decreasing over the ocean, with a minimum value observed after approximately 12 days. SSA was underestimated by WRF-CAM5, and the modeled values are constrained to a narrower range than observations highlighting the importance of improving the representation of mass absorption and extinction in regional climate models.

Chapter 1

Introduction

Atmospheric aerosols are tiny solid or liquid particles suspended in the Earth's atmosphere (Boucher, 2015; Tomasi and Lupi, 2017). Aerosols are ubiquitous in the atmosphere. They can have significant impacts on a local, regional, and global scale. At the local and regional levels, urban air pollution emitted from vehicular and industrial sources leads to a reduction in visibility (Mayer, 1999; Boucher, 2015) and poses a potential threat to human health (Nel, 2005; Nichols et al., 2013). On a global scale, aerosols play significant roles in climate change. They influence the Earth's climate through their interaction with solar radiation and their role in the cloud life cycle (Ramanathan et al., 2001; IPCC, 2013). Aerosols exhibit spatial and temporal variability and are characterized based on size, shape, source, location, type of emission, chemical composition, and radiative properties. (Boucher, 2015; Ramachandran, 2018). Aerosols exist in the atmosphere in sizes spanning several orders of magnitude from a few nanometers to about 100 μm (McMurry, 2003; Bilal et al., 2019). The lifetime of aerosols in the atmosphere varies over a scale of a few days to a few weeks depending on composition and size. They are removed through wet deposition during precipitation and dry deposition on surfaces.

1.1 Sources and Emission of Aerosols

Aerosols are emitted into the atmosphere from both anthropogenic and natural sources. Anthropogenic sources include human activities such as biomass burning, fossil fuel combustion, and vehicular emissions. Natural sources include sea spray and sea salt particles, soil dust and vegetation as well as wildfires and volcanic eruptions. (Boucher, 2015; Tariq et al, 2022). Aerosols are also classified based on their emission, which may be through direct injection into the atmosphere (primary aerosols) or from precursors through the condensation of vapor on existing gases as well as the nucleation of new particles (secondary aerosols) (Turpin et al., 1991). Since aerosol properties can vary spatially, they can be further classified based on the environment type and region of emissions, such as marine aerosols, desert aerosols, urban aerosols, tropospheric or stratospheric aerosols, etc. The emission source of aerosol particles not only controls the spatial and temporal variability but also influences the physical properties and chemical composition of these particles and, as such, affects their ability to interact with solar radiation. Other controls on the distribution and mass loading of aerosols include regional meteorological factors and atmospheric dynamics. Aerosols are also classified based on their composition. Organic or carbonaceous aerosols are used to describe aerosols containing organic carbon (OC) and black carbon (BC).



Fig 1.1: Different sources of atmospheric aerosols. Top: biomass burning, dust storm, industrial plant. Bottom: vehicular emissions, sea spray, domestic cooking.

1.2 Absorbing and Non-absorbing Aerosols

Virtually all atmospheric aerosols interact with solar radiation. Most aerosols reflect or scatter sunlight, while some also absorb it. The extent of these interactions depends on their properties like shape, size, and composition. Both translucent and dark aerosols scatter sunlight, but only dark aerosols absorb light appreciably. Light-absorbing aerosols contribute significantly to the uncertainty estimates of radiative forcing. Their absorption of solar radiation in the atmosphere and on the surface, e.g., on snow or ice, greatly influences Earth's radiation budget. Black Carbon (BC), Brown Carbon (BrC) / Organic Aerosols (OA), and **Mineral Dust** are the three main absorbing aerosol types, although their sources and distribution in the atmosphere differ. BC and **Mineral Dust** are mainly primary aerosols. BC emission comes from biomass burning, industrial processes, wildfires, and fossil fuel combustion, whereas **Mineral Dust** is emitted when the wind blows over arid, desert regions lifting dry soil particles into the atmosphere. BrC, on the other hand, is produced in the atmosphere from chemical transformation as secondary organic aerosols.

Black Carbon (BC), also known as soot, comprises microscopic carbon particles and is formed from the incomplete combustion of fossil fuel biofuels (Boucher et al., 2013; Bond et al., 2013). BC as part of particulate matter, has been associated with human cardiovascular and respiratory diseases. This dark aerosol has a high absorptivity that spans the entire solar spectrum (Bergstrom et al., 2007). This absorptivity depends on the mixing state with and morphologies of BC and the host aerosols (Bond and Bergstrom, 2006; Bond et al., 2013). BC also affects ice by reducing the albedo and hastening ice melting. This is particularly relevant for the Arctic, where deposits of black carbon on ice and snow contribute to shrinking the ice cover and exacerbating

global warming. In its emitted form, BC is hydrophobic but becomes hydrophilic when mixed or coated with other aerosols.

Brown Carbon (BrC), a yellowish-brown aerosol type is a component of organic carbon (OC) that has strong absorption at short visible and near-ultraviolet wavelengths (Bond, 2001; Andrea and Gelencser, 2006; Laskin et al., 2015). The absorption efficiency of BrC varies based on the emission source with absorptivity increasing with decreasing wavelength (Feng et al., 2013; Laskin et al., 2015). While the absorptivity of BrC is much lower than BC's, BrC is more abundant in the atmosphere, and as such, its total absorption in a region can be significant (Feng et al., 2013). Due to the complexity of the composition of BrC, being a mixture of multiple organic compounds, and its ability to undergo processes such as oxidation which can affect its absorptivity, there is high uncertainty in its radiative properties as well as its lifetime in the atmosphere. Various studies have estimated the lifetime of BrC to range from minutes to days (Lee et al., 2014; Wang et al., 2016; Cappa et al., 2020).

Mineral Dust aerosols are tiny soil particles suspended in the atmosphere that plays a vital role in the Earth's system (Gouldie and Middleton, 2006). They account for over 65% of global aerosol loading, thereby constituting the largest single component of the primary natural aerosols (Adebiyi et al., 2023). Due to long-range transport, their significance extends far beyond desert regions (Schepanski, 2018). The emission of these particles depends on the environment and the meteorological conditions. Mineral dust aerosols usually contain elements from the Earth's crust, such as iron, aluminum, potassium, and silicon, and generally tend to have a short lifetime in the atmosphere.

Pure scattering aerosols such as nitrates, sulfates and sea salt aerosols are very important due to their prevalence within the environment. Nitrate aerosols can be formed from the heterogeneous reactions of other aerosol types, such as mineral dust or sea salts entrained in the atmosphere with nitrogen oxides (Gibson et al., 2006; Bauer et al., 2007).

Sulfate aerosols have both natural and anthropogenic origins, e.g., volcanic eruptions, fossil fuel combustion, and traffic emissions, and can also be produced in the atmosphere by chemical reactions from gaseous precursors, namely sulfur dioxide (SO2) and dimethyl sulfide (DMS). Sulfate aerosols can also cause acid rain and act as cloud condensation nuclei (CCN) or ice nuclei (IN), therefore influencing the climate (Takemura, 2020; Lin et al., 2022).

Sea-salt aerosols are a non-absorbing coarse aerosol type that is highly hygroscopic (Tang et al., 1997). The ability to take on water makes them effective CCNs. Sea salt can be formed from the action of wind and the dispersal of sea spray from the ocean surface, with sizes ranging from about 0.5 μm to 10 μm (Reid et al., 2001; Ramachandran, 2018). Sea-salt aerosols are the main sources of CCN over the ocean, and they affect the microphysical properties of marine clouds (Kommalapati and Valsaraj, 2009; Chen et al., 2020).

1.3 Aerosol & Climate

Atmospheric aerosols are an integral part of the earth's climate system. They interact with solar energy reaching the planet, therefore impacting the global energy budget and, by extension, influencing the climate. (Haywood and Boucher, 2000; Boucher et al., 2013). On average, the Earth receives 341 Wm-2 of solar irradiance, of which approximately 22.8% is attenuated in the atmosphere and roughly 23% is scattered back into space by gases, aerosol particles, and clouds in the atmosphere (Trenberth et al., 2009).

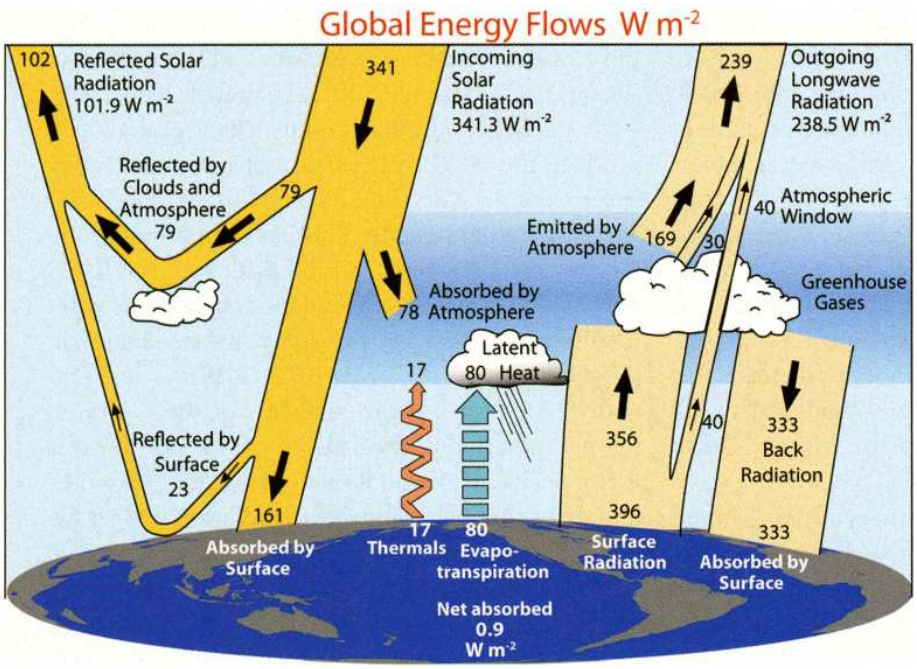

Fig 1.2: The Earth's diurnal average energy budget (adapted from Trenberth et al., 2009)

The effects of aerosols on climate vary depending on the type, location, concentration, and property of aerosols in the atmosphere. While some aerosols purely scatter solar radiation, resulting in the counteracting of greenhouse gas-induced warming and subsequent cooling of the planet, others can absorb sunlight, contributing to the heating of the troposphere and decreasing

relative humidity, thus hindering cloud formation, and consequently promoting a warming effect on the planet. The radiative impact of a specific type of aerosol is dependent on its surrounding environment, which could potentially result in varying effects. The scattering and absorption of sunlight by atmospheric aerosols is known as the “direct effect” and are often referred to as Aerosol-Radiation Interactions (ARI) (Ackerman et al., 2000; Boucher, 2015). Aerosols also act as CCN or IN, influencing the formation, microphysical and optical properties, and atmospheric lifetime of clouds. This is known as the aerosol indirect effect or, more recently as Aerosol-Cloud Interactions (ACI) (Kaufman et al., 2002; Pöschl 2005; Kanakidou, 2013; Boucher, 2015).

1.3.1 Aerosol-Radiation Interactions (ARI); Direct and Semi-Direct Effects

Aerosols scatter and absorb incoming solar radiation, affecting Earth's energy budget (Figure 1.3). The extent of scattering depends on the aerosols' size, shape, and composition, as well as their concentration and vertical distribution in the atmosphere. Both scattering and absorption by aerosols alter the amount of radiation that reaches the Earth’s surface, however, absorption by BC or BrC traps sunlight within the atmosphere, causing local heating within the layer where the aerosol is, thereby modifying the vertical temperature structure (Santer et al., 1996).

The nature and magnitude of this effect are usually contingent on the interplay between the brightness of the aerosols and that of the underlying surface. Scattering aerosols have a greater impact on increasing the regional albedo over dark surfaces as compared to bright surfaces. Conversely, absorbing aerosols have a larger effect in reducing the regional albedo over bright surfaces while their impact is relatively lower over dark surfaces. (Bellouin et al., 2020).

Absorbing aerosols alter the atmospheric temperature profile and may affect cloud distribution. When suspended near clouds, they tend to induce cloud evaporation by warming the surrounding air. This is known as the first semi-direct effect. (Hansen et al., 1997; Koch and Genio, 2010). Cloud loss can further promote absorption by the surface in a positive feedback loop (Jacobson, 2002). The semi-direct effect can also result in cloud enhancement by increasing atmospheric stability, depending on the region and type of cloud. Evaporation of low-to-mid level clouds results in positive radiative feedback, causing warming, whereas the case is the opposite for cirrus clouds. (Chen et al., 2000)

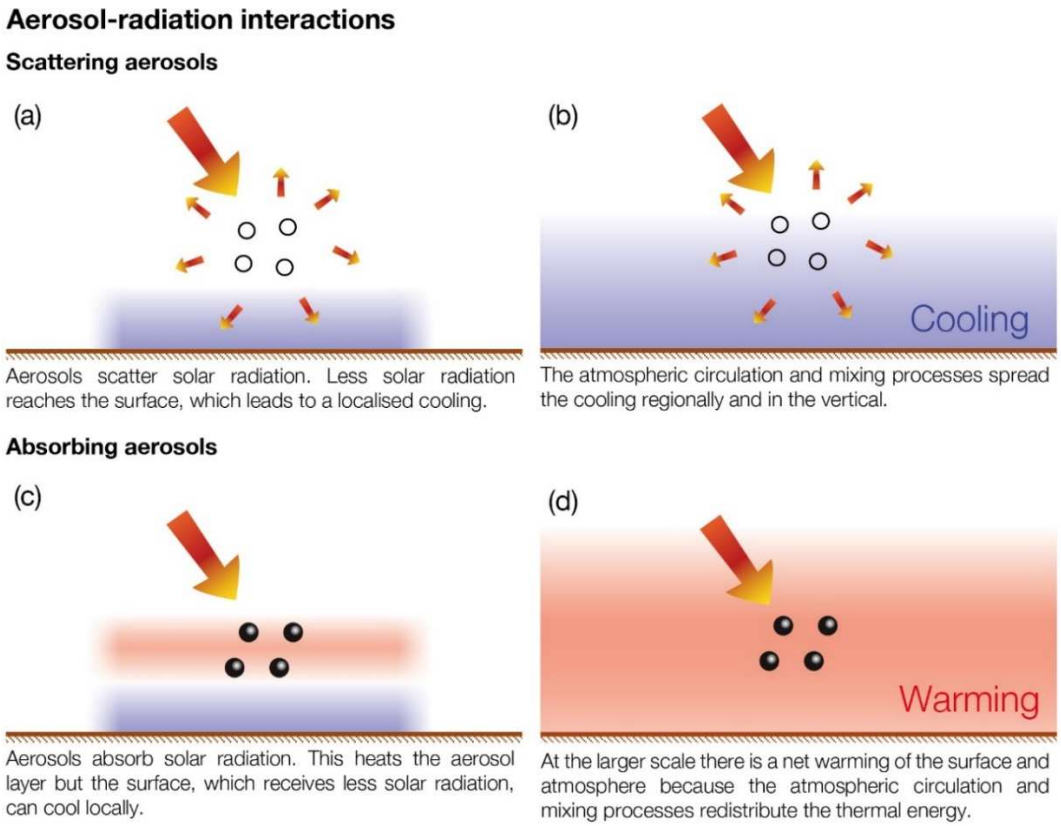

Fig 1.3: An overview of the aerosol-radiation interactions showing the impact of non-absorbing (a, b) and absorbing (c, d) aerosols. Graphics from Chapter 7; Clouds and Aerosols, IPCC AR5 (Boucher et al., 2013)

The aerosol direct effect is often described with Mie theory, a physical model that describes light scattering and absorption by spherical particles. The theory expresses light scattering as a function of the refractive index of the particle and its size compared to the wavelength of light. The refractive index measures how much a material slows down light as it passes through it and is defined as the ratio of the speed of light in a vacuum to the speed of light in the material. The imaginary component of the refractive index is responsible for absorption. This theory is used to derive the scattering efficiency given as:

$$Q_s = \frac{2}{x^2}\sum_{n=1}^{\infty}(2n+1)[|a_n|^2 + |b_n|^2] \quad Equation\ 1.1$$

Where a_n & b_n are the Mie scattering coefficients and x is the size parameter (defined as $2 * \pi * r / \lambda$, where r is the radius of the particle and λ is the wavelength of the light), n is the complex refractive index of the particle. Due to their size, most aerosols are within Mie scattering regime for solar radiation, which favors enhanced forward scattering.

Extinction efficiency Q_e which describes the total light extinction by aerosols is the sum of scattering and absorption efficiencies.

$$Q_e = Q_s + Q_a \quad Equation\ 1.2$$

where Q_a is the absorption efficiency.

Another fundamental equation used to describe the effect of aerosols on radiation is the Beer-Lambert law, which states that the amount of radiation attenuated by a substance is proportional to the concentration of the substance and the path length of the radiation through the substance. Mathematically, the equation is expressed as:

$$I = I_0 * e^{(-\tau m)} \quad Equation\ 1.3$$

Where I is the intensity of the radiation after passing through the substance layer, I_0 is the initial intensity of the radiation, I/I_0 is the transmission, τ is the extinction coefficient (a measure of the absorbing and scattering properties of the aerosols), and m is the path length of the radiation through the substance.

Radiative forcing (RF) is a measure of the impact of a particular atmospheric constituent (such as aerosols and GHGs) on the radiative balance between incoming and outgoing energy in the Earth's atmosphere. It is expressed in units of Watts per square meter (W/m^2) and it can be used to estimate the change in the Earth's average surface temperature resulting from such climatic perturbation (Boucher et al., 2013; Ramachandran, 2018). It is defined as input minus output such that a positive radiative forcing results in an imbalance; with more energy being trapped in the Earth's atmosphere, leading to a warming effect. A negative radiative forcing results in a decrease in the amount of energy being trapped, leading to a cooling effect.

Effective radiative forcing (ERF) measures the change in net energy flux at the TOA after considering the complex interactions between the various forcing agents and the Earth's climate system, known as adjustments, including temperature, clouds, and water vapor. ERF is not a direct measure of the Earth's surface temperature change but rather an estimate of the potential temperature change. ERFari is used to describe ERF due to aerosols-radiation interactions and is estimated at medium confidence to be –0.3 ± 0.3 Wm^-2 according to the latest IPCC report (Forster et al., 2021).

1.3.2 Aerosol-Cloud Interactions (ACI); Indirect Effects

Aerosol-cloud interactions refer to how aerosols affect clouds, mainly by acting as cloud condensation nuclei (CCN), altering cloud drop size distributions, and changing cloud albedo and

lifetime (Figure 1.5). Understanding these interactions is important because clouds strongly regulate the Earth's temperature, reflecting more solar radiation than aerosols (Twomey, 1974).

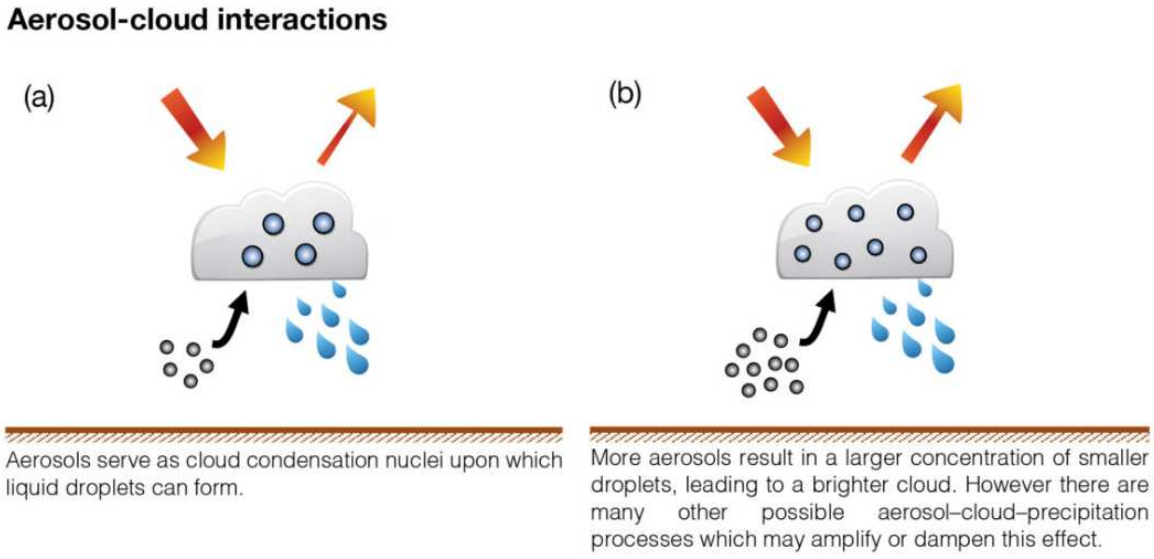

Fig 1.4: An overview of aerosol-cloud interactions (ACI), showing how they affect climate. (a) shows a clean low-level cloud, (b) shows a polluted low-level cloud. Figure adapted from Boucher et al., 2013 (Chapter 7; Clouds and Aerosols, IPCC AR5 report)

These interactions are also sources of uncertainty to the estimates of RF due to the feedback loop between aerosol impacts on clouds and cloud effects on aerosols (Boucher et al., 2013). CCN are particles around which water vapor and low-volatile gases can condense to form cloud droplets (Andreae and Rosenfeld, 2008; Colbeck and Lazaridis, 2014). Aerosols can act as CCN if they are hygroscopic, meaning they can absorb water. The supersaturation of water vapor influences aerosol to act as CCN. The Koehler theory explains the hygroscopic growth of aerosols to become cloud droplets (Koehler, 1936; Seinfeld & Pandis, 2018). The number concentration of CCN can influence the number of cloud droplets, i.e., an increase in CCN concentration will generally cause

an increase in droplets which can lead to an overall increase in cloud reflectivity. This is the first indirect or cloud-albedo effect, otherwise known as the Twomey effect (Twomey, 1977). Another way aerosols can affect clouds is the second indirect effect, or the Albrecht effect, which describes the modification of cloud drop size distribution. Small cloud droplets formed in regions of small-sized aerosols are less likely to coalesce and fall out of the cloud, resulting in longer cloud lifetimes and delayed precipitation (Albrecht, 1989; Rosenfeld, 1999). The complexity of aerosol-cloud interactions makes it challenging to understand these processes and to adequately represent them in models, which is why the ACI contributes the largest uncertainty to estimates of RF.

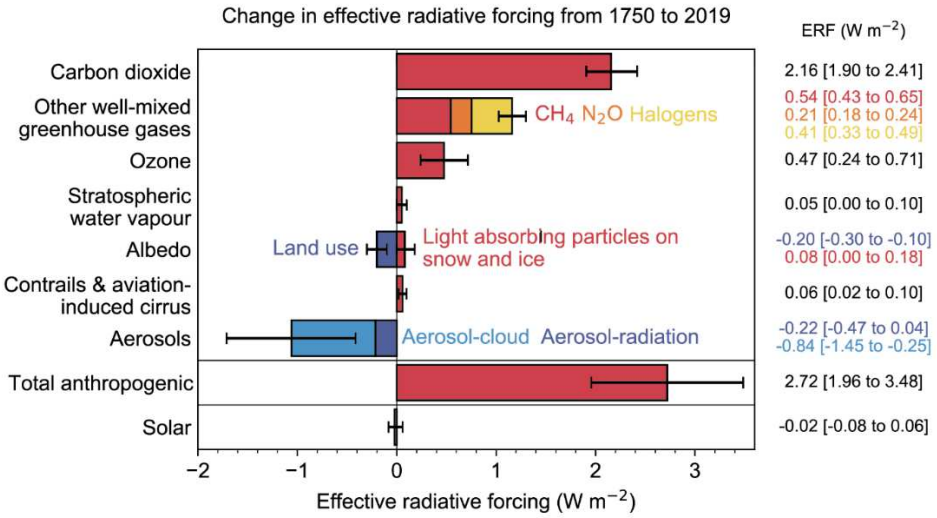

Fig 1.5: Change in effective radiative forcing by climate drivers, showing contributions from aerosol-radiation interactions and aerosol-cloud interactions. From Forster et al., 2021 (Fig 7.6, Chapter 7, IPCC AR6 report)

1.4 Aerosol Properties; physical, chemical, and optical properties

Aerosols can vary in terms of their properties; thus, the study of their physical, chemical, optical, and radiative properties is critical to understanding their nature and interactions (Ghan and Schwartz, 2007)

1.4.1 Physical Properties of Aerosols

Size Distribution, Shape, and Density: The size of aerosol particles is a crucial physical property that affects their behavior in the atmosphere. Aerosols are typically classified into three size ranges: Aitken or nucleation mode (0.001 μm - 0.1 μm), large particles or accumulation mode aerosols (0.1 μm – 1.0 μm), and the giant particles or coarse mode (>1.0 μm) (Junge, 1958). On a global scale, aerosol size distribution variability is high as different atmospheric processes may cause these modes to overlap. However, the Junge categorization provides a suitable method for understanding aerosol size distribution. The shape of particles plays a role in the ARI. Spherical particles have a smaller surface area to volume ratio than irregularly shaped particles, affecting their ability to scatter light and interact with radiation. Particle shape and density can influence their settling velocities which play a key role in cloud scavenging and dry deposition (Pilinis & Pandis, 1995).

1.4.2 Chemical Composition of Aerosols

Composition: The composition of aerosols is derived from a wide range of chemical substances, including inorganic compounds, such as silicates, sulfates, nitrates, soot, and organic compounds such as polycyclic aromatic hydrocarbons (PAHs) and volatile organic compounds (VOCs). The chemical composition of aerosols can affect their behavior in the atmosphere, including their lifetime and ability to scatter light. Other chemical properties include hygroscopicity and chemical

reactivity. Hygroscopicity refers to the ability of aerosol particles to take up water from the atmosphere. Hygroscopic aerosols can play a significant role in cloud formation and precipitation. The chemical reactivity of atmospheric aerosols is also an important property that affects their behavior in the atmosphere and impacts air quality. For example, VOCs can react with ozone and other pollutants to form secondary pollutants. This reactivity can also influence the formation of haze and smog, which can have adverse impacts on human health.

1.4.3 Optical and Radiative Properties

The interaction between atmospheric aerosols and solar radiation is represented by the scattering (β_{sca}) and absorption (β_{abs}) coefficients. The extent of these interactions can also depend on the refractive index of the particle which describes how light is bent as it passes through the particle (Cotterell et al., 2020). β_{sca} and β_{abs} are referred to as extensive properties as they can be directly measured in the atmosphere and they are used to derive other intensive optical properties such as the single scattering albedo (SSA), Ångstrom exponent (AE or α) and asymmetry parameter (g). The extensive property relates to aerosol concentration while the intensive properties can be used to determine particle sizes and shape (Rajesh and Ramachandran, 2020).

1.4.3.1 Aerosol Optical Depth

Aerosol Optical Depth (AOD) is a key parameter used in radiative transfer calculations and climate change assessment and it represents the abundance of aerosol in a vertical column of air (Remer et al 2005; Sa'id & Garba, 2018). AOD, an intensive property is an indicator of aerosol loading (Li et al., 2021) and it is mathematically expressed as the vertical integral of extinction coefficient β_{ext} (Boucher, 2015)

$$\tau = \int_{\text{SFC}}^{\text{TOA}} \beta_{ext} dz \;\; Equation\ 1.4$$

where τ is the AOD, TOA means the top of the atmosphere, SFC refers to the surface, and β_{ext} means the extinction coefficient.

1.4.3.2 Single Scattering Albedo

The aerosol single scattering albedo (SSA) is a measure of the fraction of light that is scattered by an aerosol particle in a single interaction, relative to the total amount of light that is incident upon the particle. SSA, an intensive property, can be used to quantify the contribution of aerosols to planetary albedo (Chýlek and Wong, 1995; Russell et al., 2002). It is expressed as the ratio of scattering coefficient β_{sca} to extinction coefficient β_{ext} (which is a sum of absorption and scattering coefficients), i.e., $\beta_{sca} + \beta_{abs}$ (Moosmüller et al., 2012).

$$SSA = \frac{\beta_{sca}}{\beta_{ext}} \;\; Equation\ 1.5$$

SSA is a dimensionless quantity and together with the surface albedo, can be used to determine the sign of radiative forcing (Bergstrom et al., 2007). SSA values range from 0 to 1, where a value of 0 indicates total light absorption by the particle, causing warming and a value of 1 indicates that all the incident light is scattered by the particle, causing cooling. An SSA value of 0 would imply pure black aerosol while a value of 1 would mean a pure white aerosol (Mitchell, 2022; Moosmüller et al., 2012).

1.4.3.3 Ångstrom Exponent: Extinction (EAE)

Extinction Ångstrom Exponent (EAE) is a measure of the wavelength dependence of extinction and is relatable to particle sizes. It is essentially the negative of the slope of extinction against wavelength when plotted on a log scale. Knowing the spectral dependence of aerosol extinction is fundamental for estimating aerosol forcing and analyzing aerosol microphysical properties (Eck et al., 1999; Levy et al., 2007). EAE has been used in several studies to determine aerosol size and type (Eck et al., 1999; Schuster et al., 2006; Aladodo et al., 2022). EAE is an intensive parameter and is expressed by:

$$EAE = -\frac{ln\frac{\tau_{\lambda 1}}{\tau_{\lambda 2}}}{ln\frac{\lambda 1}{\lambda 2}} \quad Equation\ 1.6$$

EAE < 1 would imply the optical dominance of coarse particles (e.g., dust, sea spray) while EAE > 1 would indicate dominance of fine particles (e.g., smoke).

1.4.3.4 Ångstrom Exponent: Absorption (AAE)

The absorption Ångstrom exponent (AAE) is similar to the EAE, only for the absorption component of extinction (Luo et al., 2020). For aerosols with sizes less than 50 nm, the AAE of pure BC is estimated to be 1.0, while BrC usually exhibits higher AAE values (It is mathematically defined as:

$$AAE = -\frac{ln\frac{\tau_{abs_{\lambda 1}}}{\tau_{abs_{\lambda 2}}}}{ln\frac{\lambda 1}{\lambda 2}} \quad Equation\ 1.7$$

1.5 Southern Africa BB Season and the Southeast Atlantic Climate System

Biomass burning (BB), the burning of vegetation, including forests, farmlands, and savannas, is the largest source of carbonaceous aerosol globally (Bowman et al., 2009; Vermote et al., 2009; Bond et al., 2013). These smoke emissions release large quantities of methane, carbon dioxide, carbon monoxide, BC, and BrC into the atmosphere (Andreae & Gelencser, 2006; Hopkins et al., 2007). While the chemical composition of these particles is dependent on the fire conditions as well as the kind of burning materials, OC and BC are the dominant aerosol types (Ramaswamy et al., 2001; Chylek et al., 2019) and account for approximately 40% of BC, the strongest light-absorbing aerosol component, in the atmosphere (Bond et al., 2004). Southern Africa contributes approximately 35% of Earth's biomass burning aerosol (BBA) emissions (van der Werf et al., 2010; Granier et al., 2011; Redemann et al., 2021). During the austral winter and spring, which coincides with the BB season in Africa and the period of highest cloud coverage in the southeast Atlantic (SEA) region, smoke is transported westward from continental southern Africa by the convective circulation of the African easterly jet towards the southeast Atlantic Ocean where it overlies a persistent stratocumulus (Sc) cloud deck (Waquet et al., 2013; Adebiyi & Zuidema, 2016; Zuidema et al., 2016).

This type of cloud covers approximately 20% of Earth's surface and is prominent in regions of oceanic upwelling, mostly on the west coast of continents (Wood, 2012; Dobracki, 2018). The upwelling brings cool water to the surface, which limits convection and improves the stability of the marine boundary layer (MBL). The SEA region is characterized by heavy periodic loads of BBA which accounts for the global maximum of aerosols above clouds (Waquet et al., 2013; Adebiyi et al., 2015). BBA in this region can modify the vertical distribution of clouds, leading to

changes in cloud cover and cloud thickness. In addition, these particles are often in direct contact with the MBL and interact with the Sc cloud deck, strengthening it and leading to higher cloud reflectivity.

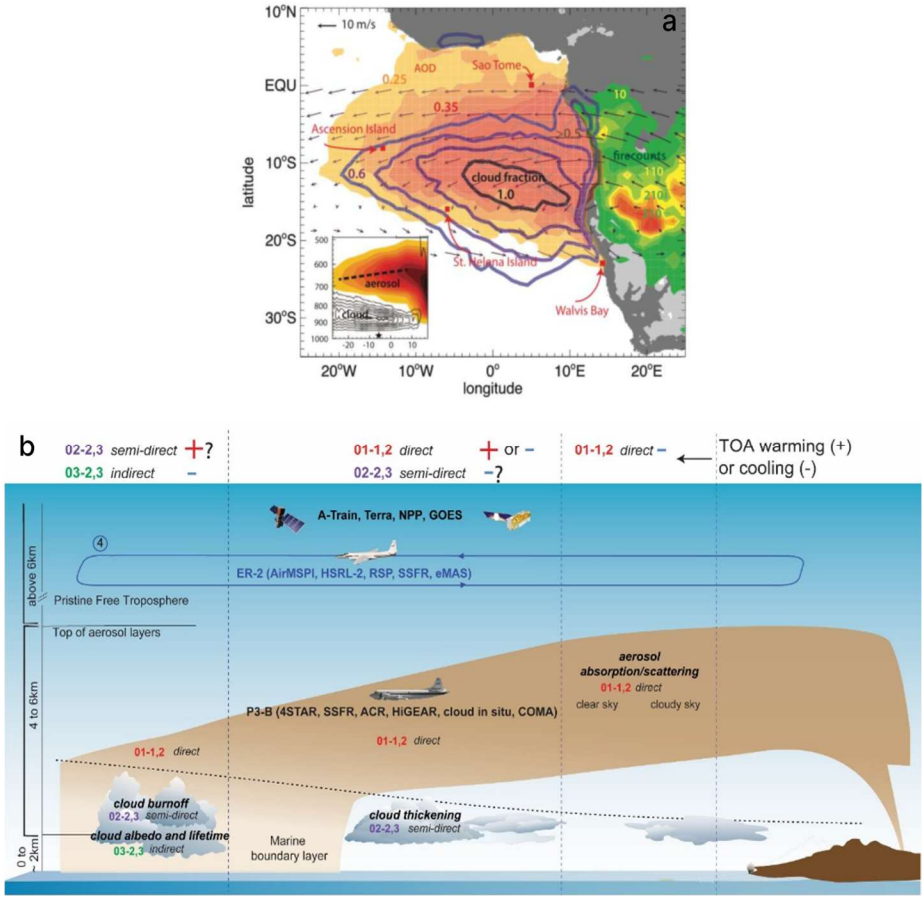

Fig 1.6: (a): Map of the SEA region showing the wind vectors following BBA transport. Adapted from Zuidema et al. 2016 (b): Illustration of the activities in the SEA, showing aerosol-radiation, aerosol-cloud interactions as well as the schematic of observational instruments used in the ObseRvations of Aerosols above CLouds and their intEractionS (ORACLES) mission.

Studies have shown that BBA have high efficiency to act as CCN, and they account for about 65% of total CCN in the Sc cloud deck of the SEA (Andreae & Rosenfeld, 2008; Che et al., 2021). Since aerosol-cloud interactions contribute the largest uncertainty to model estimates of anthropogenic forcing, the SEA region exhibits a large model-to-model divergence of climate forcing due to aerosols (Sakeada et al., 2011; Stier et al., 2013; Mallet et al., 2020; Che et al., 2021; Haywood et al., 2021). The region is particularly valuable for studying and understanding these BBA interactions and the effect of the highly absorbing BBA on regional climate. This has recently been the subject of international large-scale field campaigns, including the CLoud–Aerosol–Radiation InteRactions and Forcing for Year 2017 (CLARIFY-2017) (Zuidema et al., 2016; Haywood et al., 2021), Layered Atlantic Smoke Interactions with Clouds (LASIC) (Zuidema et al., 2018), AErosols, RadiatiOn and CLOuds in southern Africa (AEROCLO-sA) (Formenti et al., 2019) and the ObseRvations of Aerosols above CLouds and their intEractionS (ORACLES) (Redemann et al., 2021).

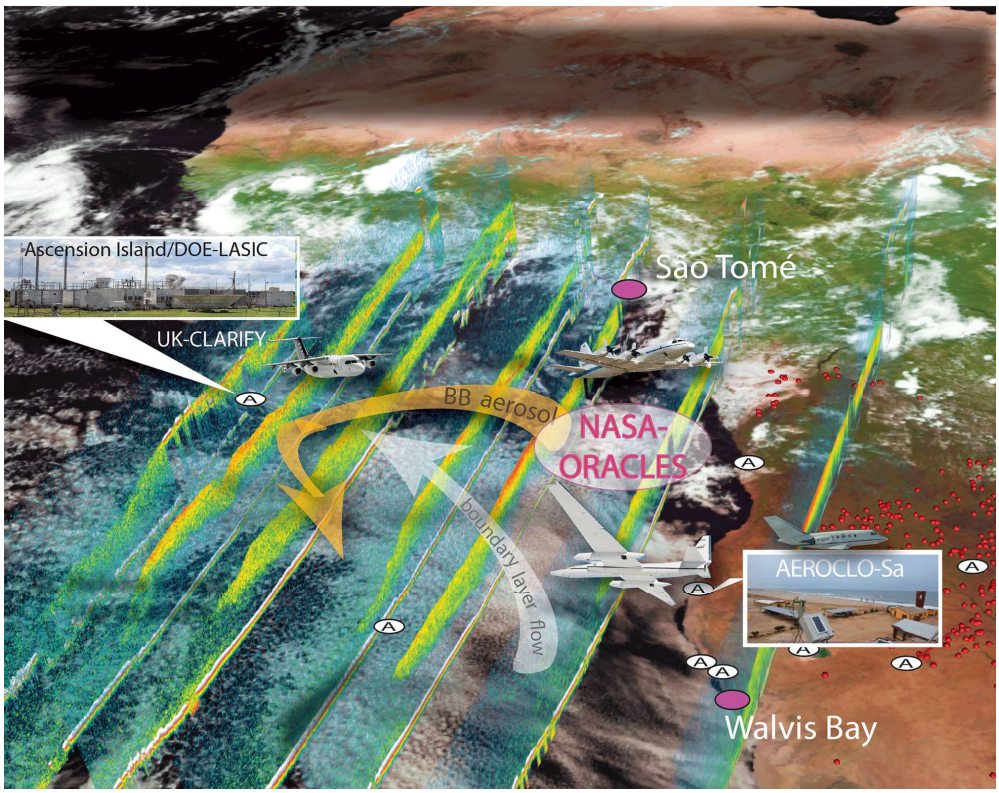

Fig 1.7: Overview of SEA region showing the international field missions and the study area of the ORACLES deployments. AERONET sites are indicated with the letter A and the red dots are showing active fires from NASA VIIRS (Redemann et al., 2021)

1.6 ORACLES - ObseRvations of Aerosols above CLouds and their intEractionS

The complexities in the ARI and ACI by absorbing aerosols and low Sc clouds in the SEA region continue to serve as the impetus for field studies which include the recently concluded multiyear suborbital airborne ORACLES campaign. ORACLES, a project involving five NASA centers and eight US universities, was aimed at providing significant measurements of aerosol radiative effects in the SEA and bridging the gap in parameterizing ACI and ARI in earth system models. (Redemann et al., 2021). The goals of the campaign were to determine the influence of BB aerosol from continental Africa on cloud properties and the energy balance in the SEA region, through state-of-the-art in situ and remote-sensing observations and to acquire a process-level understanding of ARI and ACI and their resulting cloud adjustments that can be applied in global models. A summary of the campaign's specific objectives is shown in the table:

Table 1: Summary of ORACLES science questions and objectives. (Redemann et al., 2021)

Science questions	Related science objectives
Q1: what is the direct radiative effect of the African biomass burning (BB) aerosol layer in clear- and cloudy-sky conditions over the SE Atlantic?	O1-1 (aerosol spatial evolution): determine the evolution of the BB aerosol microphysical and spectral radiative properties as the aerosol is transported across the South Atlantic. O1-2 (aerosol-induced radiative fluxes): measure aerosol-induced spectral radiative fluxes as a function of cloud albedo and aerosol properties. O1-3 (seasonal aerosol variation): assess the key factors that control the seasonal variation in aerosol direct effects.
Q2: how does absorption of solar radiation by African biomass burning (BB) aerosol change atmospheric stability, circulation, and ultimately cloud properties?	O2-1 (relative vertical distribution): determine the seasonally varying relative vertical distributions of aerosol and cloud properties as a function of distance from shore. O2-2 (aerosol–cloud heating rates): constrain aerosol-induced heating rates for aerosol layers above, within, and below cloud. O2-3 (cloud changes due to aerosol-induced heating): investigate the sensitivity of cloud structure and condensate to aerosol-induced heating rates.
Q3: how do BB aerosols affect cloud droplet size distributions, precipitation, and the persistence of clouds over the SE Atlantic?	O3-1 (mixing survey): survey the location and extent of aerosol mixing into the boundary layer (BL) and its seasonal variation. O3-2 (cloud changes due to aerosol mixing): measure changes in cloud microphysical properties, albedo, and precipitation as a function of aerosol mixing into the BL. O3-3 (cloud changes due to aerosol-suppressed precipitation): investigate the sensitivity of cloud structure and condensate to aerosol-induced suppression in precipitation.

The campaign lasted three years (2016 – 2018), with field deployments from Walvis Bay, Namibia in September 2016 and São Tomé, São Tomé and Príncipe in August 2017 and October 2018. Each deployment featured a host of remote sensing and in situ instruments, including the Spectrometer for Sky-Scanning, Sun-Tracking Atmospheric Research - 4STAR (further discussed in Section 2.2), and other in situ probes aboard the NASA P-3 research aircraft (N426NA) and the ER-2 high-flying aircraft (N809NA). A total of 27 (12 ER-2, 15 P-3) research flights collected a significant amount of data on aerosol optical properties. (Pistone et al., 2019).

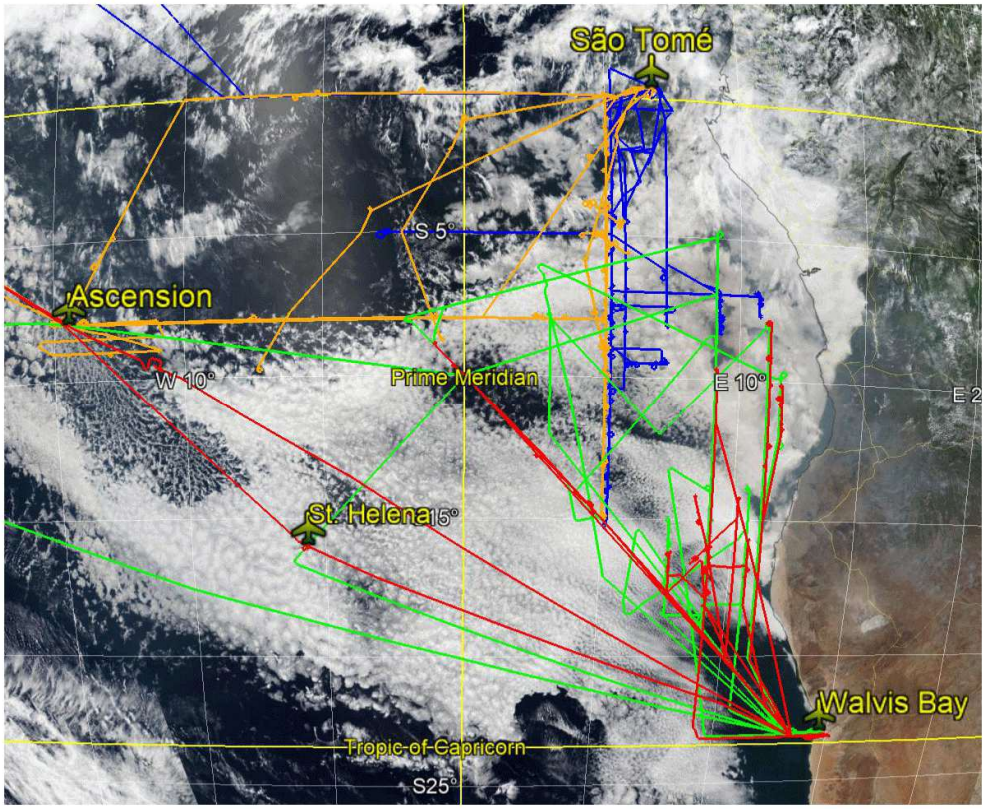

Fig 1.8: ORACLES flight tracks (2016 ER-2 in green, 2016 P-3 in red, 2017 P-3 in orange, 2018 P-3 in blue) overlaying the Sc cloud deck over the study area. The deployment base for 2016 is labeled as Walvis Bay and for 2017 and 2018 as São Tomé (Redemann et al., 2021)

1.7 Motivation and Thesis Statement

The annual pattern of BBA advection from continental Africa over the Southeast Atlantic Ocean and the accompanying aerosol-cloud-climate interactions make the SEA region a natural laboratory for understanding the radiative effects of BBA. In previous climatological studies, aerosol optical properties have been shown to shift during the July-October BB season (Adebiyi et al., 2015; Redemann et al., 2021), with maximum aerosol loading in September while SSA increases throughout the burning season. According to recent studies, the aerosols in this region demonstrate an unusually high ability to absorb sunlight (Chylek et al., 2019; Pistone et al., 2019; Shinozuka et al., 2020; Holanda et al., 2020). BBA in this region usually have SSA values less than 1, often ranging between 0.7 and 0.95 as highlighted in (Dubovick et al., 2002; Eck et al., 2013; Pistone et al., 2019) These low SSA values shows that BBA has strong implication for radiative warming. This warming effect of BBA is not well represented in Earth System Models (ESMs) (Stier et al., 2013; Haywood et al., 2021).

Quantifying the extent of this warming is important for understanding the energy balance in the region. The southern African smoke aerosol transport into the Amazonian basin is among the longest transatlantic aerosol transport patterns and has been documented in recent studies (Zheng et al., 2020; Holanda et al., 2020; Baars et al., 2021). However, the evolution of these BB aerosols in terms of their chemical, optical, and physical properties during transport is not well-documented despite their significance and associated impacts on climate. A recent study by Sedlacek et al., 2022 attempted to characterize the lifecycle of BBA using the mixing state of BC. Figure 1.9 shows the many processes that govern the evolution of these particles on different temporal scales.

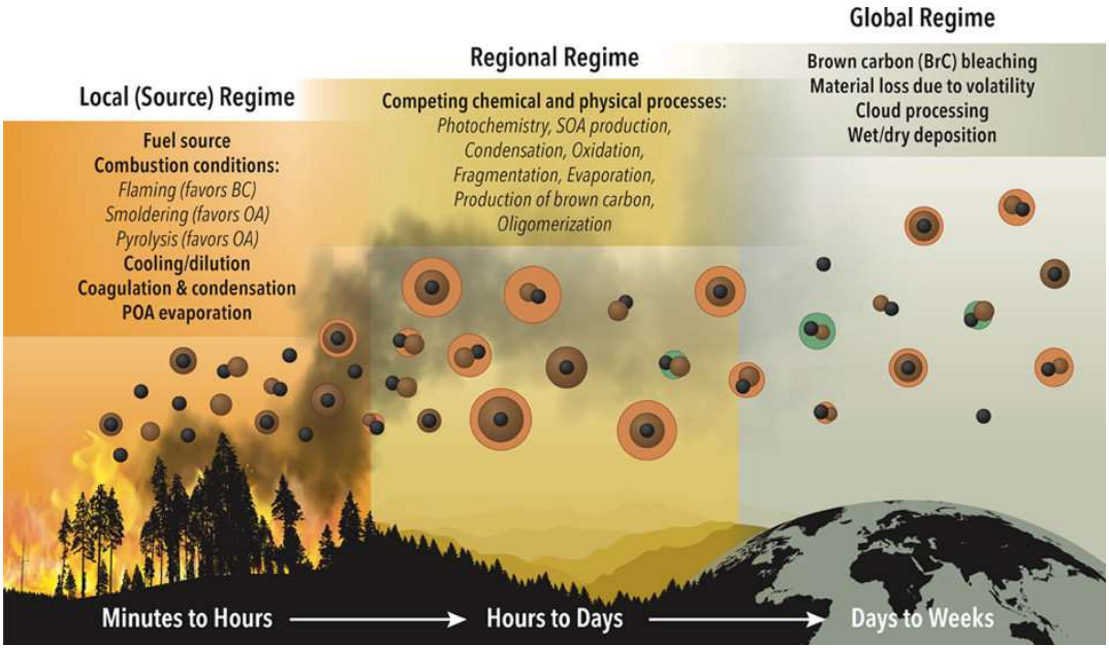

Fig 1.9: Lifecycle of BBA showing the controls on particle properties on different time scales. Figure by Tiffany Bowman. Adapted from Sedlacek et al. (2022).

Although the aging and lifecycle of BBA are becoming introduced in global climate models (Konovalov et al., 2021; Nascimento et al., 2021), the complexities in the chemical and physical processes involved in their evolution make it difficult to adequately represent the optical and microphysical properties of these particles in models as most evolution and aging studies have focused on near-source emissions or laboratory experiments on short time scales. However, we need to bridge a knowledge gap by understanding the changes in the optical properties of these particles as they age on a larger temporal scale, such as during their long-range transport. This serves as the fundamental basis for this thesis research.

This study's overarching goal is to investigate the evolution of BBA optical properties from emission within continental Africa, during transport over land, and then over the Atlantic using remote-sensing observations. This study focuses on the BB season in the SEA and features data

from the ground-based Aerosol Robotics Network (AERONET) and the NASA ORACLES campaign. The specific science questions to be answered are:

1. What discernible changes in biomass burning aerosol optical properties can be identified across the southeast Atlantic region using a combination of ground-based AERONET and airborne 4STAR observations?
2. To what extent does the regional model, WRF-CAM5, accurately depict the optical properties of biomass burning aerosols within the southeast Atlantic region?

Chapter 2

Data and Methods

2.1 Instruments and Data Sources

In order to investigate changes in the optical properties of smoke plumes as they age, we used a combination of airborne in situ and remote-sensing instruments including 4STAR (Spectrometer for Sky-Scanning, Sun-Tracking Atmospheric Research), as well as ground-based AERONET data. We then combined these with output from two regional models, the WRF-AAM and WRF-CAM5, during the three years of ORACLES.

We analyzed these datasets to investigate changes in extinction, single scattering Albedo (SSA), and Ångstrom exponent (AE) with age, as well as to compare observations with model results.

2.1.1 AErosol RObotics NETwork (AERONET)

AERONET is a global federated network of ground-based sky-scanning sunphotometers. It was established by the National Aeronautics and Space Administration (NASA) in collaboration with PHOTONS (PHOtométrie pour le Traitement Opérationnel de Normalisation Satellitaire). With more than 800 stations globally, across all continents and many oceanic islands, the AERONET project provides long-term, continuous, publicly accessible data of aerosol microphysical, optical, and radiative properties for aerosol characterization and in the validation of satellite retrievals (Holben et al., 1998). The key instrument at each station is the CIMEL Electronique CE-318 sun-sky radiometer, shown in Figure 2.1, which measures direct solar beam at a 1.2 full field of view (FOV) every 15 minutes across eight wavelengths; 340, 380, 440, 500,

670, 870, 1020, 1640 nm for the retrieval of aerosol microphysics. The sampling rate varies from station to station, with some stations measuring every 3 minutes or approximately 5 minutes. Direct sun measurements are taken at all wavelengths to measure the optical attenuation by the atmosphere which is then used to infer AOD at each wavelength -except for the 940 nm channel-, which is used to retrieve total column water vapor. The computed AOD uncertainty, mainly due to calibration uncertainty, is approximately 0.010-0.021 for field instruments, with higher errors in the UV (Eck et al., 1999). A study by Schmid et al. (1999) compared AOD from four solar radiometers, including an AERONET sun-sky radiometer, and found that the AOD from 380 to 1020 nm agreed within a root mean square (RMS) difference of 0.015, which is similar to the estimated level of uncertainty in AOD measurements for field instruments. The calibration of sky radiances is done against frequently characterized integrating spheres at the National Aeronautics and Space Administration (NASA) Goddard Space Flight Center, achieving an absolute accuracy of approximately 5% or better, as stated by Holben et al. (1998).

In this research, we employ the quality-assured AERONET Version 3 products, derived using an algorithm that offers automatic cloud screening, instrument anomaly quality controls (Giles et al., 2019), and improved retention of high AOD values that were frequently disregarded in prior iterations (Bhattacharjee et al., 2023). Sinyuk et al. (2020) provide a comprehensive examination of the Version 3 inversion retrieval algorithm and a comparison of the Version 3 product to Version 2. The CIMEL instruments perform almucantar sky radiance scans at fixed elevation angles matching the solar elevation, with sequential azimuthal sweeps at four wavelengths (440, 675, 870, and 1,020 nm). These scans are carried out in both morning and afternoon (Eck et al., 2019). Hybrid sky scans with the new CIMEL C318-T are also used for AERONET retrievals. The hybrid sky scan method moves simultaneously in both the azimuthal

and zenith angle directions, creating an intermediate scan between the almucantar and principal plane, which varies the zenith angle while maintaining a fixed azimuth (Eck et al., 2019). The selection of four AERONET stations: Mongu_Inn (hereafter referred to as Mongu), Huambo, Namibe, Ascension Island (see Figure 2.2) used in this study is strategic and based on the transport trajectory of biomass burning (BB) aerosols from continental Africa and over the ocean. Detailed information on each of the AERONET stations is provided in table 2.

Table 2: Site information for AERONET stations used in this study

AERONET Site	**Longitude/Latitude**	**Elevation (m)**	**Valid Observation (N)**
Ascension Island	14.41° W - 7.97° S	30	92
Namibe	12.17° E - 15.15° S	11	535
Huambo	15.70° E - 12.86° S	1070	769
Mongu_Inn	23.13° E - 15.26° S	1040	187



Figure 2.1: A typical CIMEL Electronique CE-318 sun photometer used in the AERONET mission. (Image credit: Dong, 2020)

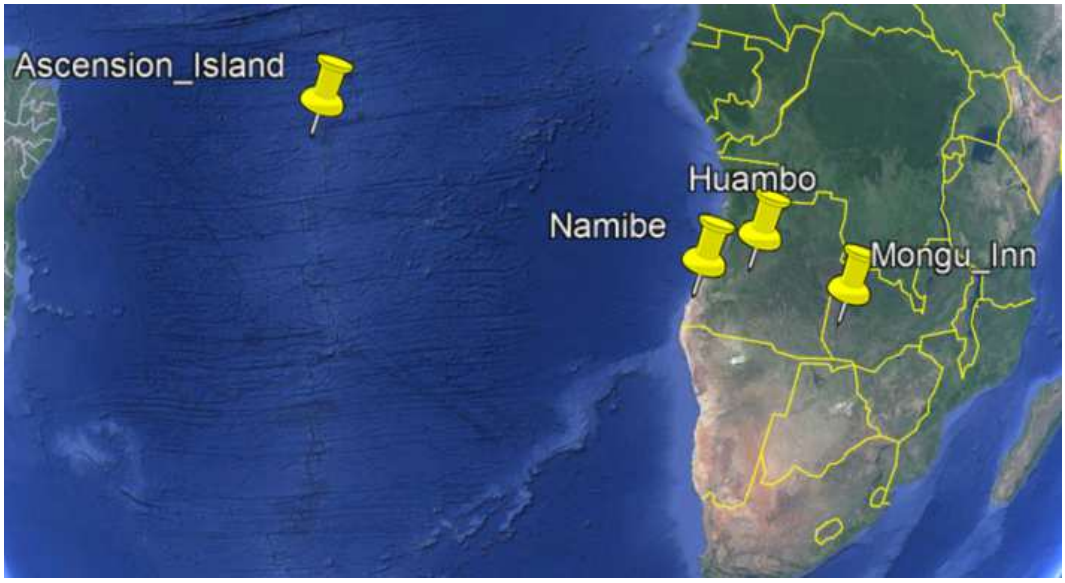

Figure 2.2: Location of AErosol RObotics NETwork (AERONET) stations used in this study. Adapted from Google Earth.

2.1.2 4STAR

The 4STAR – Spectrometers for Sky-Scanning, Sun-Tracking Atmospheric Research, is an airborne spectrometer that measures direct solar beam and sky radiances similar to AERONET. It also provides hyperspectral retrievals of columnar aerosol optical properties, and trace gas constituents including AOD, ozone, and water vapor (Dunagan et al., 2013; Segal-Rosenheimer et al., 2014). 4STAR, a multiple-use instrument illustrated in Figure 2.3, can operate in three modes; a sun-tracking mode (Segal-Rosenheimer et al., 2014; Leblanc et al., 2020) which involves actively following the motion of the sun and using measurements of the amount of direct sunlight passing through the atmosphere to determine the optical depth of various atmospheric components; a sky-scanning mode (Pistone et al., 2019). The third mode is a zenith mode for below cloud measurements of cloud parameters such as cloud optical depth, droplet size, and thermodynamic phase as in LeBlanc et al. (2015).

4STAR uses two grating spectrometers that measure direct solar irradiance and angular resolved sky radiance across a range of wavelengths from 350nm to 1700nm. The first spectrometer covers the UV-VIS-NIR bands with a spectral resolution of 2-3nm (< 1000 nm), while the second spectrometer covers the SWIR band with a spectral resolution of 3-7 nm (>1000 nm) at a sampling rate of 1Hz (Leblanc et al., 2020). 4STAR was integrated into the NASA P-3 aircraft and active in all three years of ORACLES.

4STAR is particularly unique and valuable as it replicates AERONET measurement from an aircraft. Additionally, 4STAR offers a more comprehensive observation experience through its auto-collocation with in situ measurements. This study will focus on observations combining the sun-tracking mode with the sky-scanning mode in which, similar to AERONET, the 4STAR makes

almucantar (ALM) and principal plane (PPL) mode scanning using its ability to measure the angular distribution of brightness in the sky. ALM scanning involves 4STAR scanning in clockwise (CW) and counterclockwise (CCW) directions on either side of the sun. The two ALM legs are then evaluated for sky symmetry, with ALM scans that pass this test having the potential for higher quality assurance/quality control than PPL scans (Pistone et al., 2019). However, determining an ALM average for the two legs may be challenging if there is non-uniformity in the ALM scan that fails the sky symmetry test (Mitchell, 2022).

This study considers both principal plane and almucantar scans when specific quality control (QC) criteria are met. We do this because the 4STAR sky scans were mostly conducted around solar noon during ORACLES flights, which limits the available angular range for almucantar scans. In processing the 4STAR sky scans, quality control criteria similar to those employed by AERONET were applied. The QC applied in this study (as initiated by Pistone et al. (2019) and modified and implemented by Mitchell (2022)) includes; sky scans conducted below 3000m altitude, a polynomial fit AOD at 400nm greater than 0.2, an altitude difference below 50m and sky error less than 10%. The scattering angle used spans from 3.5-50°, with at least 6 Scattering Angles in the critical 3.5-30° range.

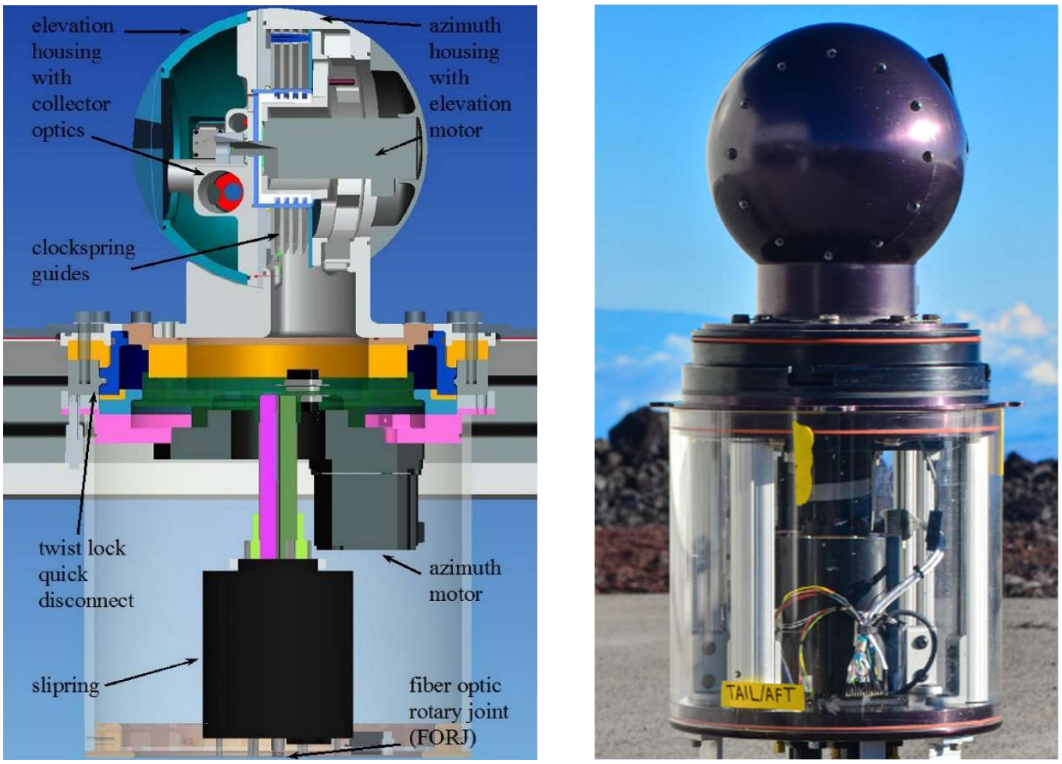

Figure 2.3. The Spectrometer for Sky Scanning Sun-Tracking Atmospheric Research (4STAR): Schematic and components (left), Physical look (right)

2.2 Weather Research and Forecasting (WRF) Model Output

The output from two regional models, WRF-AAM and WRF-CAM5, are used to estimate aerosol optical properties in the SEA region. WRF-AAM was used to estimate the age of the aerosol plumes and WRF-CAM5 was used for the horizontal and vertical distribution of aerosol optical depth and single scattering albedo.

2.2.1 WRF-CAM5: Concept and Configuration

The Weather Research and Forecasting (WRF) model is a numerical weather prediction system that simulates atmospheric processes, provides weather and air quality forecasts, and can be used to study aerosol effects at grid-scale and subgrid-scale resolution (Glotfelty et al., 2019). WRF-CAM5 is an adaptation of the WRF-Chem model (Grell et al., 2005), coupled with the physics and aerosol packages of the global Community Atmosphere Model version 5 (CAM5). This coupling was first implemented by Ma et al. (2014) and subsequently improved by Zhang et al. (2015a). In contrast to other online-coupled models, this model is specifically developed for studying atmospheric processes in a multi-scale context and provides a modeling structure for assessing physics and aerosol parameterizations utilized in global climate models (Wang et al., 2018). The model has been used to replicate and analyze the relationship between air quality and climate over Asia and the United States, as described in Campbell et al. (2017), Wang et al. (2018), and Zhang et al. (2015b).

The WRF-CAM5 model incorporates advanced cloud schemes, including the Morrison two-moment cloud microphysics scheme (Morrison & Gettelman, 2008), the shallow cumulus scheme of Bretherton and Park, (2009), the University of Washington (UW) turbulence parameterization (Bretherton & Park, 2009; Shinozuka et al., 2020), the Zhang-MacFarlane (ZM)

convective cloud scheme (Zhang & McFarlane, 1995), and a two-moment parameterization for convective clouds which includes explicit feedback between aerosols and convective clouds, as described by Song and Zhang (2011) and modified by Lim et al. (2014).

The model also features an up-to-date ice-nucleation parameterization for mixed-phase and ice clouds, developed by Niemand et al. (2012), and a modal aerosol module (MAM3) with three modes: Aitken, accumulation, and coarse as in Liu et al. (2012), coupled with the Zaveri and Peters, (1999) gas-phase chemistry scheme which is used for determination of aerosol (including smoke) properties. The WRF-Chem routines (Fast et al., 2006) are used to calculate aerosol optical properties by transforming the three modes of MAM3 into eight size categories ranging from 39 nm to 10 μm, followed by a Mie theory calculation. The refractive indices for organic aerosols and black carbon (BC) are assumed to be constant at 1.45+0i (without accounting for brown carbon) and 1.85+0.71i, respectively, across the shortwave radiation spectrum (Shinozuka et al., 2020). The cloud droplet activation scheme, developed by Fountoukis and Nenes (2005) and implemented by Zhang et al. (2015a), takes into consideration the activation of giant cloud condensation nuclei (CCN) as well as insoluble particles like dust and black carbon.

In this study, the WRF-CAM5 model uses a 36 km x 36 km horizontal resolution and 74 vertical layers, with varying resolutions ranging from 10 to 500 m over the spatial domain 41◦S-14◦N, 34◦W-51◦E. The resolution tends to be finer at lower altitudes. The model is initialized every five days using data from the National Centers for Environmental Prediction Final Operational Global Analysis (NCEP FNL) and CAMS reanalysis and run for seven days, with the first two days used for spin-up (Skinozuka et al., 2020; Doherty et al., 2022). The model is provided with smoke emissions initialized daily from version 2 of the Quick-Fire Emissions Dataset (QFED2) (Darmenov & Da Silva, 2015). According to Doherty et al. (2022), in an inter-model assessment

study, it was found that the WRF-CAM5 model is one of the best-performing models when it comes to smoke concentrations, optical properties, and the vertical location of the BBA plume over the SEA.

2.2.2 WRF-AAM

The Thompson aerosol-aware microphysics (AAM) scheme (Thompson & Eidhammer, 2014) is one of the parameterization schemes introduced into the WRF model, allowing for regional and case-specific microphysical parameterization of cloud condensation nuclei (CCN) and cloud droplet interactions. In addition to various types of hydrometeors such as water, ice, snow, graupel, and rain, the model also accounts for the transport of two aerosol species: hygroscopic and ice-nucleating. The AAM (Aerosol-Aware Microphysics) configuration was recently updated to include aerosol-radiation interactions (Saide et al., 2016).

2.3 Plume Age Derivation

All ORACLES research flights were conducted over the southeast Atlantic (SEA) ocean, away from the fire sources in continental Africa (refer to figure 1.8). To estimate the physical age of the aerosols, researchers often rely on the simulation of tracers in models. In this study, WRF-AAM was run in forecasting mode to estimate the aerosol time since emission, with maximum aerosol age of 14 days.

The model attaches age tracers to carbon monoxide (CO) released from biomass burning emission sources. The tracers are tagged for each day and are tracked for up to two weeks, allowing sufficient time for the smoke to travel to the southeast Atlantic Ocean. These tracers are treated as inert gases, and they do not react with any other species or evolve chemically. Every day, the tracers from the previous day are moved to the next older tracer bin. This means that the tracer is initially emitted at age 0 days with CO from the fires, then after one simulated day, the tracer is shifted to the 1-day aged bin while new emissions from the fires become 0-day aged. The process continues until the tracers reach the age of 14 days, at which point they remain in the oldest size bin and continue to accumulate as additional tracers are aged into that bin. The smoke plume age is calculated as the average of the tracer concentration distribution. Hence, the accuracy of smoke at the upper end of the age estimate range is compromised. Even if a parcel of smoke comprises an equally concentrated mixture of tracers that have been out for different lengths of time beyond the 14-day tracking period, it would still be averaged as 14 days old.

The model set up for this study is similar to the configuration in a previous study by Saide et al., 2016, with a horizontal resolution of 12 km covering the region (41◦S-14◦N, 34◦W-51◦E), a domain size that is extensive enough to encompass nearly all fires across the African continent.

The fire source for the model is derived from a burned area product with a spatial resolution of 500 m obtained from MODIS (Giglio et al., 2006). However, this product may underrepresent the total burned area coming from smaller fires by up to 40%, as per recent research by Ramo et al. (2021). According to previous research by Val Martin et al. (2010), it has been suggested that bigger fires in the boreal northern hemisphere are responsible for a significant portion of the emissions that reach higher altitudes. However, it remains unclear whether this vertical redistribution pattern applies to the relatively smaller agricultural fires commonly found in southern Africa (Dobracki et al., 2022). The NCEP Global Forecasting System (GFS) meteorology is the driving force behind the WRF-AAM model and incorporates daily smoke emissions from the QFED2, which is then advected and adjusted to correspond with satellite-derived aerosol optical depth using a near real-time inversion algorithm described in Saide et al., (2016). Since observations from AERONET and 4STAR are columnar integrated and point-based measurements, in order to estimate the effective aerosol age in the model at each of the valid retrievals of AERONET and 4STAR, the extinction-weighted mean aerosol age is calculated by weighting the assigned plume age by the corresponding extinction coefficient and averaging over all the measurements taken at that site and time, i.e., across all the vertical layers (See equation 2.1)

$$Aerosol\ age = \frac{\int_{s_{elv}}^{toa} \beta_{ext} * \ plume\ age\ dz}{\int_{s_{elv}}^{toa} \beta_{ext}\ dz} \quad Equation\ 2.1$$

Where s_{elv} is the elevation of the station or the flight altitude for AERONET (Ascension Island) and 4STAR respectively.

2.4 Collocation and Analysis

The temporal resolution of WRF model output, 4STAR, and AERONET observations differs, so it becomes necessary to interpolate or average the model output to match. The output from both regional models, WRF-CAM5 and WRF-AAM, are averaged and produced on a 3-hour temporal basis in a NetCDF format covering the entire spatial domain (41◦S-14◦N, 34◦W-51◦E). Output from the WRF-CAM5 is provided in 72 vertical layers between the surface and about 10km to account for BL and FT. The WRF-AAM uses 20m vertical spacing, 501 vertical layers from the surface to 10,000 meters, and the output includes datasets for all three years of ORACLES, while the WRF-CAM5 output is only available for 2016 and 2017.

Columnar retrievals of Single Scattering Albedo (SSA), Aerosol Optical Depth (AOD), and Extinction Ångstrom Exponent (EAE) were obtained from AERONET at Mongu, Huambo, Namibe, and Ascension Island. Due to sparse data availability for Level 2 at Ascension Island, we downloaded all point observations of the inversion product at Level 1.5 and Level 2 (INV_Level2_All_Points_V3 and INV_Level15_All_Points_V3) for all stations in a text format from the AERONET website (https://aeronet.gsfc.nasa.gov/). Valid 4STAR retrievals of SSA, AOD, EAE, and asymmetry parameter after QC (Mitchell, 2022) was obtained from the ORACLES website for all three deployments https://espo.nasa.gov/oracles/archive/browse/

Data from AERONET was filtered to only focus on the period of ORACLES in all three years, i.e.:

- ORACLES_2016: 27th August 2016 – 27th September 2016
- ORACLES_2017: 9th August 2017 – 2nd September 2017
- ORACLES_2018: 24th September 2018 – 25th October 2018

providing about 1600 valid retrievals for all three deployments across all stations as in table 2.

There are several methods for collocating model output and observations, including point-to-point collocation, area-to-point collocation, and area-to-area collocation. However, because AERONET and 4STAR provide point-based retrievals, here we use point-to-point collocation. We match all available AERONET observations temporally and spatially within each of the aggregated WRF output files. Similarly, we conduct the same collocation for 4STAR observations. The workflow of this collocation strategy is shown in Figure 2.4.

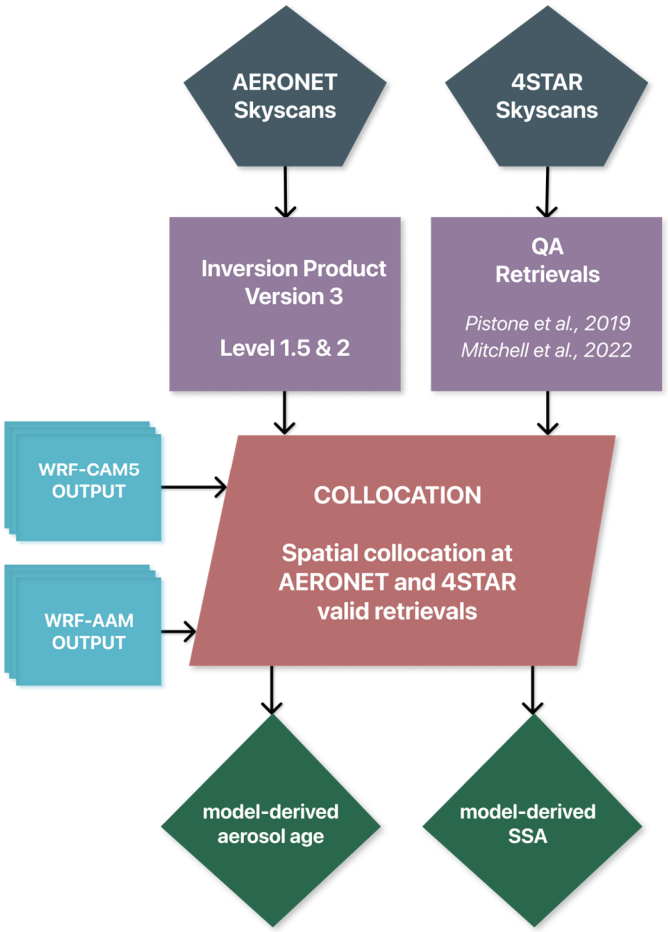

Figure 2.4: Collocation of the model outputs with AERONET and 4STAR observations.

The collocation technique yields two results, with the first output being the effective aerosol age determined from the WRF-AAM model. The second result is the optical properties obtained from the WRF-CAM5 model, which includes the model-estimated aerosol optical depth (AOD) and the effective single scattering albedo (SSA_{eff}) calculated as the extinction-weighted average of the vertically resolved model-estimated SSA (SSA_m), employing an equation similar to equation 2.1 but for SSA (see equation 2.2).

$$SSA_{eff} = \frac{\int_{s_{elv}}^{toa} \beta_{ext} * SSA_m \, dz}{\int_{s_{elv}}^{toa} \beta_{ext} \, dz} \quad Equation\ 2.2$$

To compare the model-derived aerosol properties against observation, we had to interpolate the observation wavelength to match the WRF_CAM5 model output at 500 nm using the linear interpolation equation:

$$SSA_{\lambda} = SSA_{\lambda_1} + \frac{(\lambda - \lambda_1) * (SSA_{\lambda_2} - SSA_{\lambda_1})}{\lambda_2 - \lambda_1} \quad Equation\ 2.3$$

where λ = 500 nm, λ_1 = 440 nm, and λ_2 = 675 nm.

We investigated the relationship between the WRF-CAM5-simulated SSA and observations using Pearson's (r) and Spearman's rank (ρ) correlation. Additionally, the uncertainties in the model's predictions were assessed using root mean bias (RMB), and root-mean-square error (RMSE)

$$RMB = \frac{\overline{modeled_x}}{\overline{observed_x}} \quad Equation\ 2.4$$

$$RMSE = \sqrt{\frac{1}{n}\sum_{i=1}^{n}(modeled_x - observed_x)^2} \quad Equation\ 2.5$$

2.5 Boundary Layer (BL) and Free Troposphere (FT) Partitioning

The planetary boundary layer (PBL), as defined by Seidel et al. (2010), is the atmospheric layer that interacts directly with and is influenced by the surface. When ocean surface temperatures rise, the PBL becomes deeper, eventually resulting in its separation and deepening. This phenomenon is particularly prevalent in the southeast Atlantic (SEA), where stratocumulus clouds are often found in the upper part of decoupled PBLs. Smoke aerosols from biomass burning are injected into the atmosphere at high altitudes and advected by the free tropospheric (FT) wind (Ryoo et al., 2021). The dynamics of the atmosphere over the SEA and the evidence of smoke entrainment in the marine boundary layer as well as the mixing of marine aerosols with the biomass burning aerosols (BBA) over the southeast Atlantic (Zuidema et al., 2018), make it important to carefully diagnose the vertical distribution of smoke aerosols over the region. Climatological and campaign studies from (Adebiyi et al., 2015; Pistone et al., 2019; Redemann et al., 2021) have shown that the optical properties of aerosols over continental areas such as Mongu indicate strictly BBA. As one moves further away from the south African coast, the height of the PBL increases before transitioning to a cumulus-dominated cloud regime, as explained by Zhang and Zuidema (2019, 2021) and Ryoo et al. (2021).

To understand the evolution of these particles in the SEA region, especially where the mixing happens, we attempt to make distinct analyses with respect to the boundary layer (BL) and FT. Since AERONET provides total atmospheric column retrievals and 4STAR provides columnar retrievals for altitudes above flight level, but we are interested in the evolution of FT BBA, we seek to separate the BL from the FT using the extinction ratio of BL to total column (R_{m_BL}) and the extinction ratio of FT to total column (R_{m_FT}), respectively. The ratios are derived from the

WRF-AAM model. By utilizing the 501 vertical layers in the model and accounting for the elevation at each remote sensing retrieval, as well as approximating the boundary layer height (BLH) to be 1500m above surface elevation, we computed R_{m_BL} and R_{m_FT} using the equations 2.6 and 2.7. The value of 1500m for the planetary BLH is consistent with those simulated by WRF-CAM5, GEOS-CHEM, and MERRA_2 in the study by Chang et al. (2022).

$$R_{m_BL} = \frac{\int_{s_{elv}}^{BLH} \beta_{ext} dz}{\int_{s_{elv}}^{toa} \beta_{ext} dz} \quad Equation\ 2.6$$

$$R_{m_FT} = 1 - R_{m_{BL}} \quad Equation\ 2.7$$

These ratios are then used to partition the columnar AOD (AOD_{TC}) measurements from the remotely sensed observation as shown in equation 2.8 and equation 2.9.

$$AOD_{BL} = R_{m_BL} * AOD_{TC} \quad Equation\ 2.8$$

$$AOD_{FT} = R_{m_FT} * AOD_{TC} \quad Equation\ 2.9$$

where AOD_{BL} and AOD_{FT} are the partitioned AOD for BL and FT respectively for Ascension Island and 4STAR. The WRF-AAM model-derived extinction was calculated at 532 nm, hence, we linearly interpolated optical properties from the observation to match this wavelength.

We next calculate the SSA in FT as:

$$SSA_{FT} = \frac{(SSA_{TC} * AOD_{TC}) - (SSA_{BL} * AOD_{BL})}{AOD_{FT}} \quad Equation\ 2.10$$

while taking the assumption that the single scattering albedo within the marine boundary equals unity.

Similarly, we compute the aerosol age in the FT for over-the-ocean retrievals using:

$$Aerosol_{age_{FT}} = \frac{\int_{BLH}^{toa} \beta_{ext} * \ plume\ age\ dz}{\int_{BLH}^{toa} \beta_{ext}\ dz} \quad Equation\ 2.11$$

2.6 Extinction Ångstrom Exponent (EAE) Thresholds

Using Equation 1.6, we calculate the Extinction Ångstrom Exponent (EAE) at 440–870 and 440 – 675. The 440 – 870 nm is incorporated in the AERONET inversion products, while 440 – 675 is used in 4STAR retrievals. EAE is sensitive to the size distribution of aerosol particles. Smaller aerosol particles have a larger EAE than larger particles because exhibit stronger wavelength dependence on extinction. Furthermore, the EAE is related to the aerosol type, with fine-mode aerosols such as smoke aerosols having a higher EAE than coarse-mode aerosols such as dust and sea salt. This has been shown in global studies (Eck et al., 1999; Schuster et al., 2006). Therefore, in addition to the BL and FT partitioning described in section 2.5, to further separate biomass burning aerosols from marine aerosols, we establish four thresholds of EAE value: EAE > 0.75, EAE > 1, EAE > 1.2, EAE > 1.4. The setting of these threshold values followed the findings of Eck et al. (1999).

Chapter 3

Results

This chapter summarizes the findings of the study. Section 3.1 presents collocated results of the WRF-CAM5 model with observations, highlighting SSA. Section 2 presents analysis of extinction-weighted aerosol age. In section 4.3, insights into the evolution of biomass burning single scattering albedo and extinction Ångstrom exponent with age are presented, providing a better understanding of their behavior over time.

3.1 Model Representation of Single Scattering Albedo

After conducting spatial and temporal collocation of the datasets, as explained in section 2.4, we analyze how WRF-CAM5 represents single scattering albedo (SSA). We perform an interpolation of SSA to 500nm in both the model and AERONET datasets, as 4STAR provides retrievals at that wavelength. Figure 3.1 presents a box-whisker plot that displays a comparison of the distribution of SSA from both observation and the WRF-CAM5 model. The mean WRF-CAM5 SSA values at four AERONET stations (Ascension Island, Huambo, Mongu, and Namibe) and 4STAR sky scans and the corresponding mean values from observations are shown in Table 3. Both model and observation show the highest mean values of SSA at Ascension Island. The spatial pattern of SSA in the WRF-CAM5 model shows lower values than observation and are confined to a narrower range of 0.80-0.89

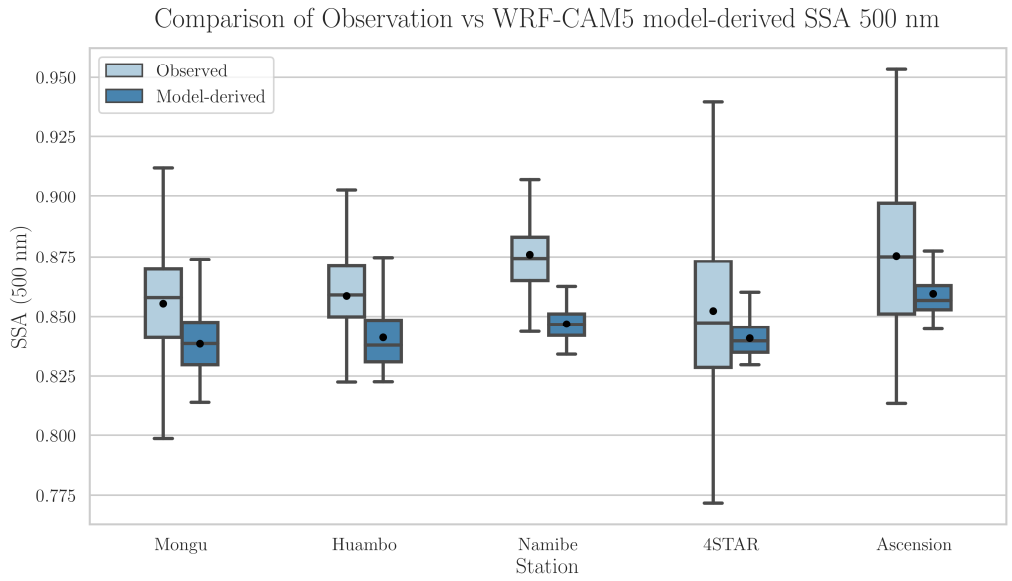

Figure 3.1(a): Statistical summary and comparison of model-derived against observation SSA for the entire ORACLES campaign. The box-whisker plot summarizes the 10th percentile (lower whisker), the 25th percentile (lower quartile), the 75th percentile (upper quartile), and the 90th percentile (upper whisker). The 50th percentile (median) is shown as the horizontal line within the box while the dark circle represents the mean SSA for each station.

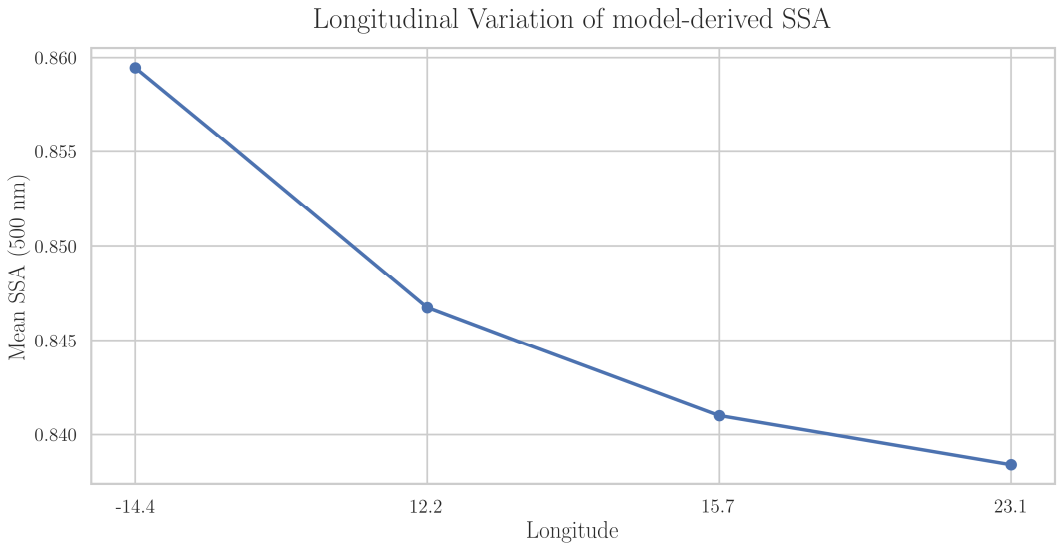

Figure 3.1(b): The longitudinal dependence of modeled SSA from all AERONET stations.

A combination of scatterplots and histograms is used to compare SSA from the model to the SSA from observation in Figure 3.2. The result of the comparison statistics is shown in table 3.

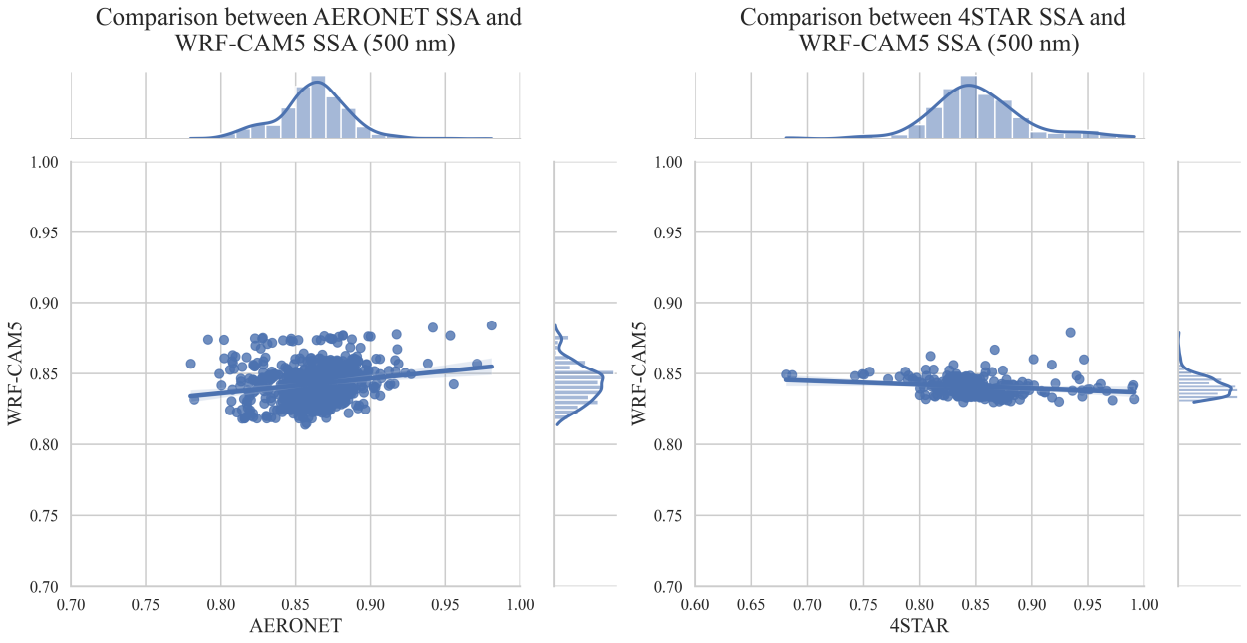

Figure 3.2: Scatterplot and histogram showing the comparison of WRF-CAM5 SSA against (a) AERONET SSA and (b) 4STAR SSA for the entire ORACLES campaign. The stacked histogram on either axis shows the bin distribution of the SSA values.

Table 3: Mean SSA values from model and observation for AERONET and 4STAR

Station/Data	**Mongu**	**Huambo**	**Namibe**	**4STAR**	**Ascension**
WRF-CAM5	0.838	0.841	0.846	0.84	0.859
Observation	0.855	0.86	0.87	0.85	0.875

Table 4: Summary of the statistics of model-observation comparison

Comparison	**Pearson (r)**	**Spearman (ρ)**	**MAE**	**RMB**	**RMSE**
WRF-CAM5 vs AERONET	0.19	0.2	0.027	0.977	0.03
WRF-CAM5 vs 4STAR	-0.18	-0.29	0.035	0.986	0.05

The comparison between WRF-CAM5 SSA and AERONET SSA showed a weak correlation, with Pearson's correlation $r = 0.19$ and Spearman's correlation $\rho = 0.2$, suggesting that the model may not accurately capture the observed variability in SSA. On the other hand, the correlation between WRF-CAM5 SSA and 4STAR SSA was negative, with $r = -0.18$ and $\rho = -0.29$, suggesting that the model tends to overestimate SSA when compared to 4STAR measurements. The statistical analysis revealed small systematic biases in both comparisons between the WRF-CAM5 model and the observations from AERONET and 4STAR. The root mean bias (RMB) values for the comparisons were 0.977 and 0.986, indicating a slight overall underestimation in the WRF-CAM5 model. Moreover, the mean absolute error (MAE) values were 0.027 and 0.035, representing the average difference between the model and observations. The root mean squared error (RMSE) values were 0.03 and 0.05, indicating the standard deviation of the differences between the model and observations.

3.2 Estimates of Biomass Burning Aerosol Age

This section presents the results of the aerosol age estimation using the WRF-AAM model, as mentioned in section 2.3. Figure 3.3 depicts the vertical profile of (a) the mean age of the plume, which was determined by evaluating the tracer concentration, and (b) the extinction, as curtain plots, which represent the distribution of aerosol age and aerosol extinction coefficients along the flight path of the P-3 aircraft for a single day case.

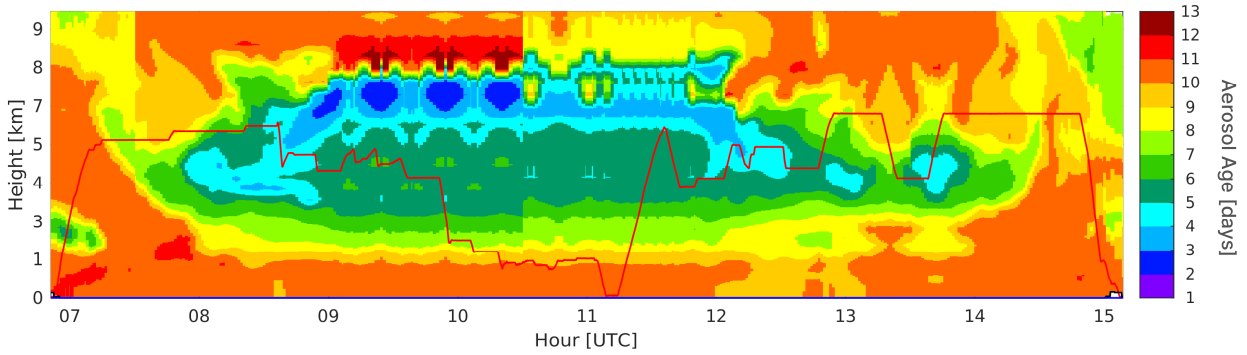

Figure 3.3(a): WRF-AAM curtain plot showing the mean plume age forecast (shading) along the P-3 flight track (red line) for October 17, 2018. Figure credit: Pablo Saide.

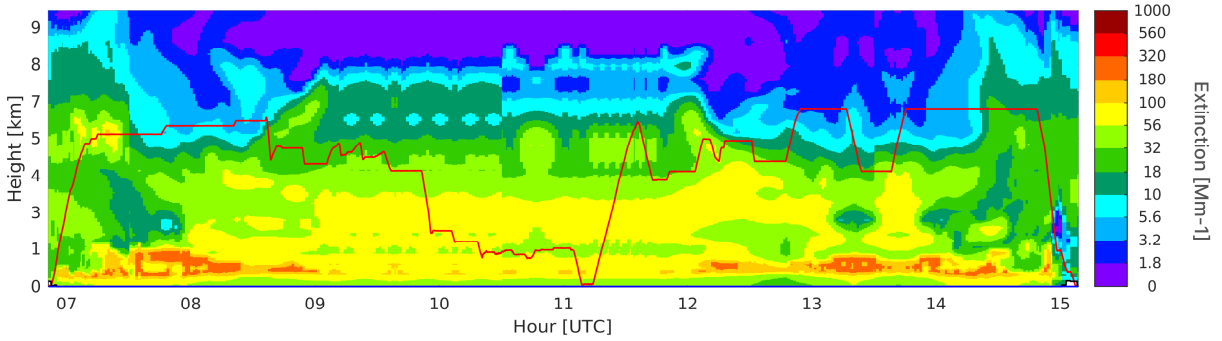

Figure 3.3(b): WRF-AAM curtain plot showing the extinction forecast (shading) along the P-3 flight track (red line) for October 17, 2018. Figure credit: Pablo Saide.

Figure 3.4 displays the distribution of extinction-weighted aerosol age over the southeast Atlantic, including aerosol age at all individual 4STAR sky scans and the mean aerosol age at Ascension Island for the three ORACLES deployment. Figure 3.5 illustrates the statistics for all observations, utilizing a box-whisker plot that enables an easy comparison of the distribution of effective aerosol age across all AERONET stations and 4STAR observations.

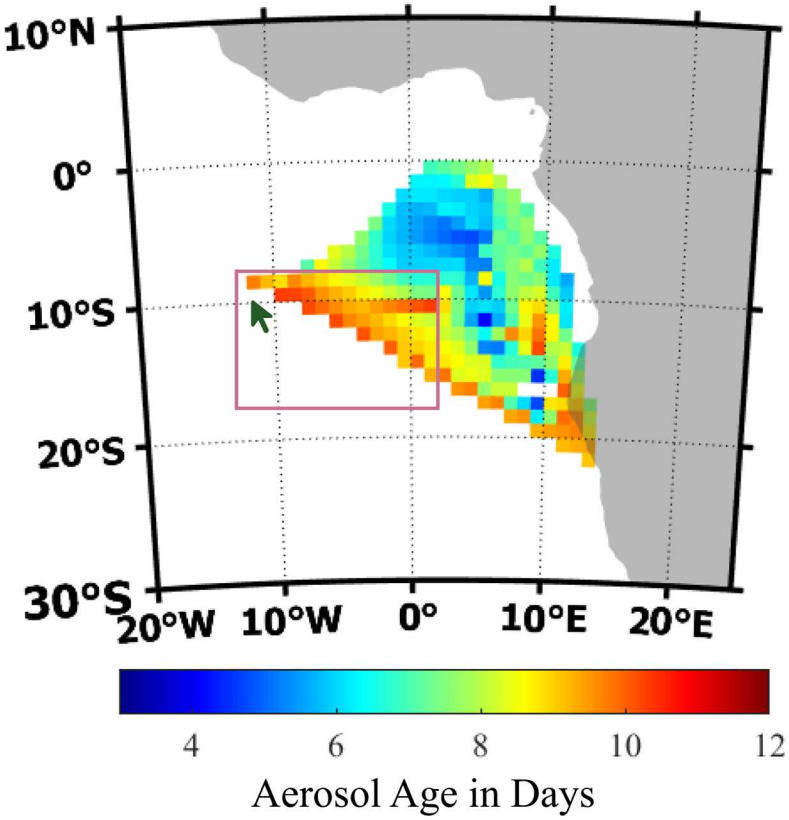

Figure 3.4: Map of the SEA region, showing the extinction-weighted aerosol age at Ascension Island and individual 4STAR sky scans during the three ORACLES deployments. The mean aerosol age is represented for Ascension Island (Green Arrow).

The results reveal that the plume sampled within the specified bounding box (23 S -10 S and 12 W – 5 E) had the highest aerosol age, ranging between 8 to 12 days, which is consistent with the range at Ascension Island where the mean age is 10 days. For 4STAR observations, the aerosol age ranged between approximately 3.5 to 11.5 days, with a mean age of 7 days. corresponding with the range at Ascension Island. At Mongu, Huambo, and Namibe, the extinction-weighted aerosol age ranged from approximately 1 to 6 days, 1 to 6 days, and 2.5 to 8 days, respectively, with mean ages of 3.7, 3.5, and 5.5 days. The variability in aerosol age shown here is further discussed in Section 4.2.

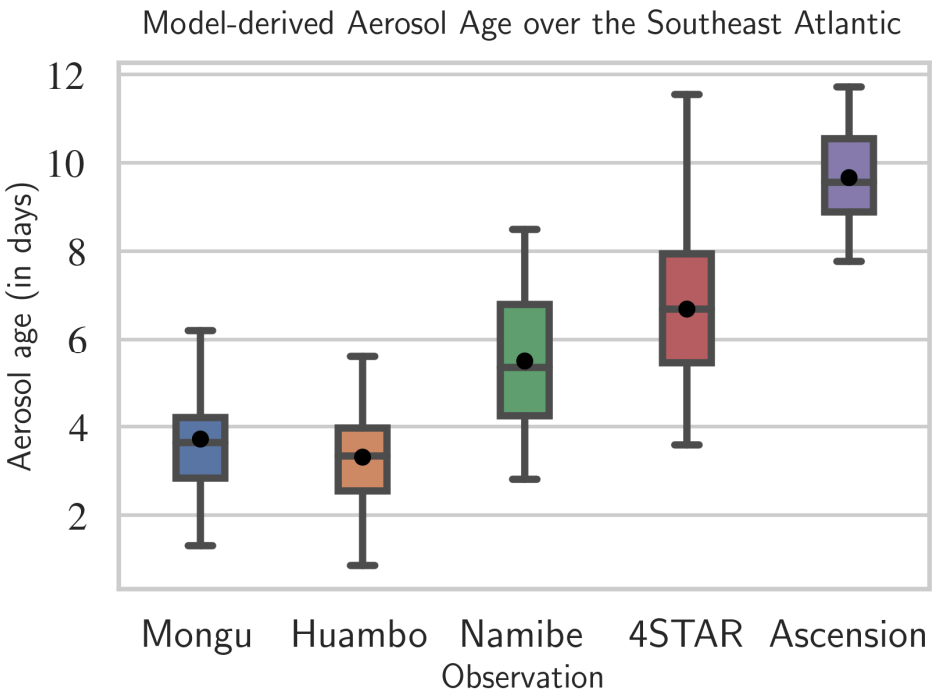

Figure 3.5: Statistics of the extinction-weighted aerosol age for all data points used in this study. The box-whisker plot shows the 10th (lower whisker), 25th (lower quartile), 50th (median), 75th (upper quartile), and 90th (upper whisker) percentiles of aerosol age. The dark circle represents the mean aerosol age.

3.3 Evolution of Biomass Burning Aerosols Single Scattering Albedo (SSA) with Age

We present here the relationship between, the single scattering albedo (SSA) and the model-derived age, stratified by the extinction Ångstrom exponent (EAE) in the total atmospheric column. Based on the results shown in Figure 3.6, the majority of samples collected at Mongu and Huambo exhibit the highest extinction Ångstrom exponent (EAE), which is visually represented by a clustered aggregation of yellow shading.

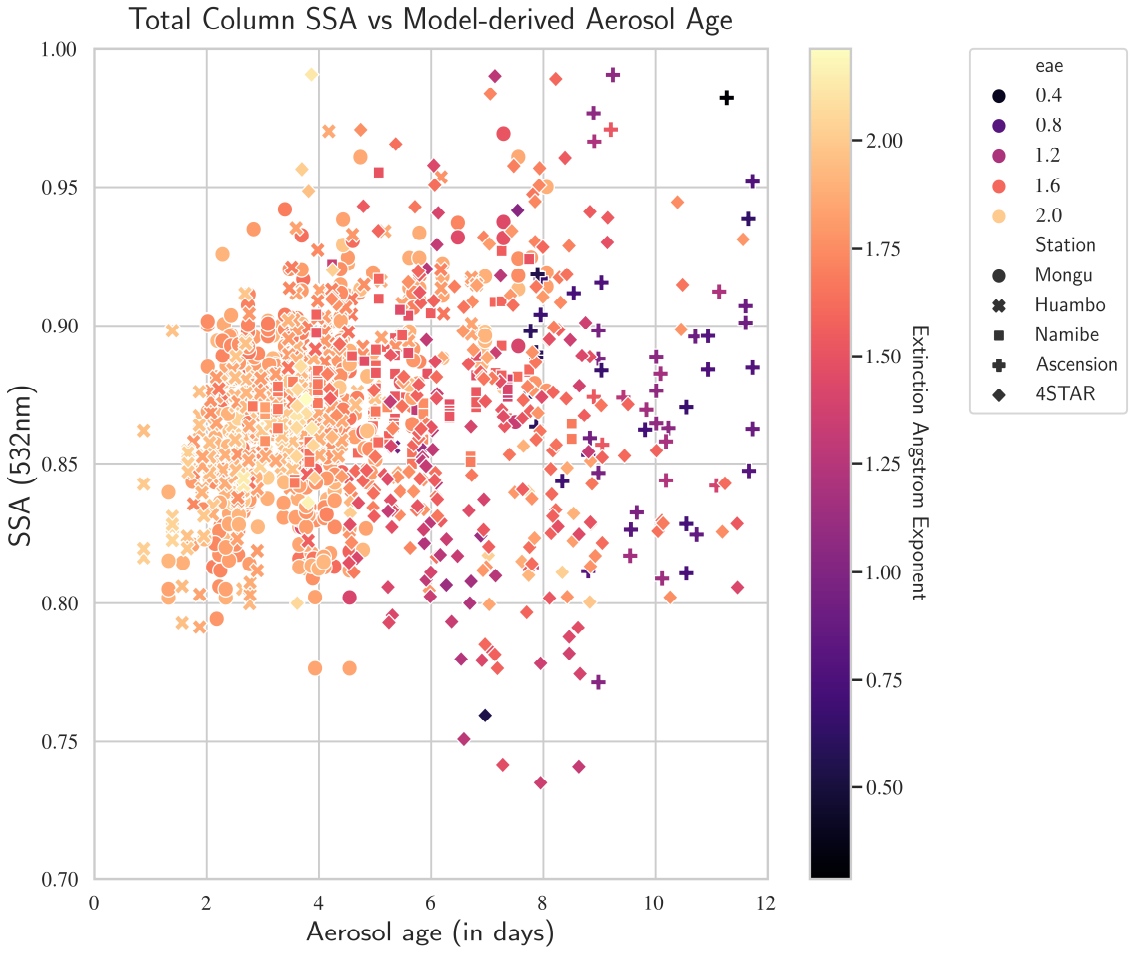

Figure 3.6: Scatterplot showing the relationship between SSA (markers), EAE (shading), and aerosol age in the total atmospheric column (TC). The different markers represent the stations while the colorbar shading represents the EAE.

The average EAE values for the samples at these two stations are 1.83 and 1.87, respectively, indicative of the prevalence of smaller-sized particles in the atmosphere over these regions. The measured single-scattering albedo (SSA) at these two stations ranges from 0.75 to 0.9, with only a few retrievals above 0.9. As the aerosol transport proceeds towards the west, a notable reduction in the EAE is observed, with a mean value of 1.5 at Namibe. Over the SEA, away from the coast, both Ascension Island and 4STAR observations showed a wide range of EAE values from 0.2 to 2.2, indicating the presence of different aerosol sizes within the vertical column.

3.3.1 Attempts to separate BL contributions from TC observations

We attempted to partition the BL from the TC to isolate only the FT BBA using two approaches, which we highlight here: first, filtering out the low EAE values by applying EAE thresholds, and second, applying the model-derived ratios of BL and FT.

3.3.2 Application of EAE thresholds

Figure 3.7 shows the progression of EAE thresholds applied to the entire observational campaign dataset. To determine an optimal EAE that would account for only fine particles in the SEA region, we initially removed all observations with EAE values less than 0.75, as illustrated in Figure 3.7(a). Subsequently, the threshold was gradually increased to filter out observations with EAE values less than 1 (b), 1.2 (c), and finally, 1.4 (d). We observe a gradual shift in the distribution of SSA for the age bins as we move across the four thresholds. To avoid discarding a significant portion of the Ascension Island measurements, where BBA may coexist with larger particles in the marine boundary layer (MBL), we chose lower values of EAE, despite Eck et al., (1999) suggesting EAE of 1.5 or higher above for BBA.

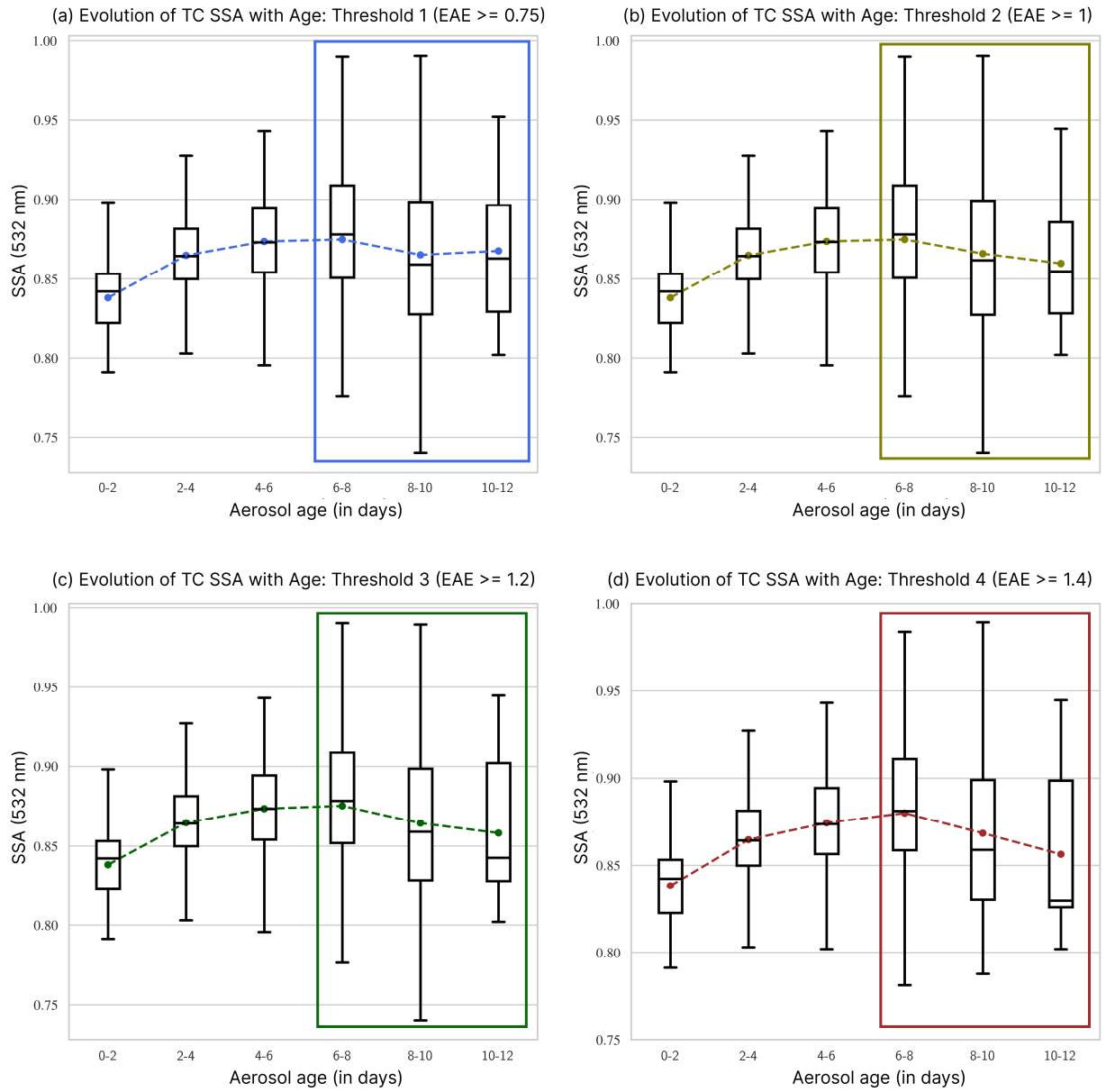

Figure 3.7: The evolution of SSA with age in the total column (TC), filtered with (a) EAE >= 0.75, (b) EAE >= 1, (c) EAE >= 1.2, (d) EAE >= 1.4. The box-whisker plot shows the 10th (lower whisker), 25th (lower quartile), 50th (median), 75th (upper quartile), and 90th (upper whisker) percentiles of TC SSA. Colored dots represent the mean SSA with the dashed lines connecting the mean across the age bins.

The aerosol age was grouped into bins of ([0-2], [2-4], [4-6], [6-8], [8-10], [10-12]), and the arithmetic mean of SSA for each bin was computed. The mean SSA for the initial two aerosol age bins remained constant at 0.838 and 0.864 across all four thresholds (Figure 3.8). For the [4-6] age bin, the mean SSA was constant at 0.873 in the first three thresholds but increased slightly to 0.874 in the last threshold. A shift in the mean SSA is observed for the (6-8), (8-10), and (10-12) age bins, as we move from one threshold to the next. The mean SSA values change from 0.875, 0.865, and 0.867 in the first threshold to 0.88, 0.87, and 0.85 in the final threshold. Further elaboration on these results is provided in section 4.3.1.

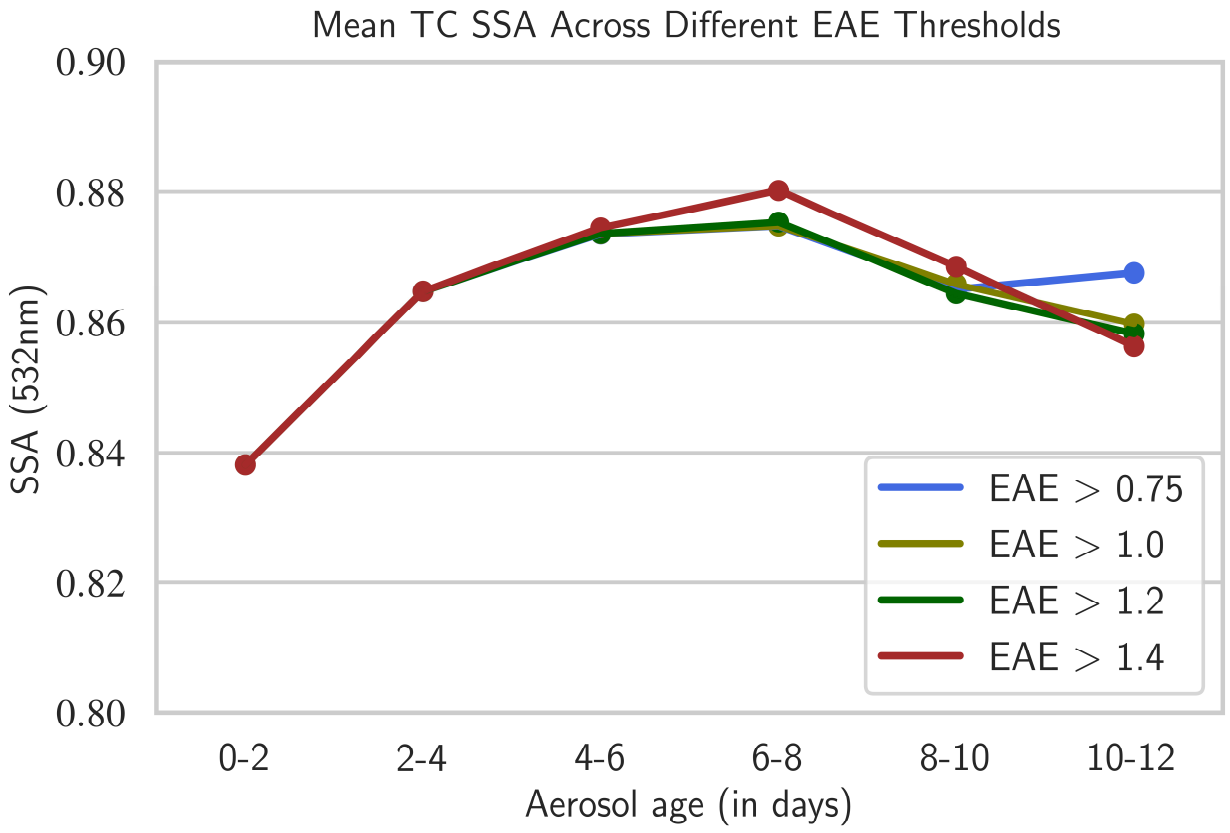

Figure 3.8: The mean total column TC SSA for all age bins across the four thresholds. The near-source observations in [0-2] and [2-4] age bins remained constant for all thresholds.

3.3.3 Applying model partition ratio to vertically resolved observations

After the discussion on the methodology to isolate contributions from the boundary layer (BL) to the total atmospheric column in section 2.5, we proceed in this section to present how SSA evolves with aerosol age in the free troposphere (FT).

The fraction of AOD in the free troposphere (FT AOD) relative to total column (TC) AOD over the SEA (as per Equations 2.6 and 2.7) derived from the WRF-AAM model is shown in Figure 3.8. Only 4STAR sky scans made at altitudes below 1500m were considered for the separation.

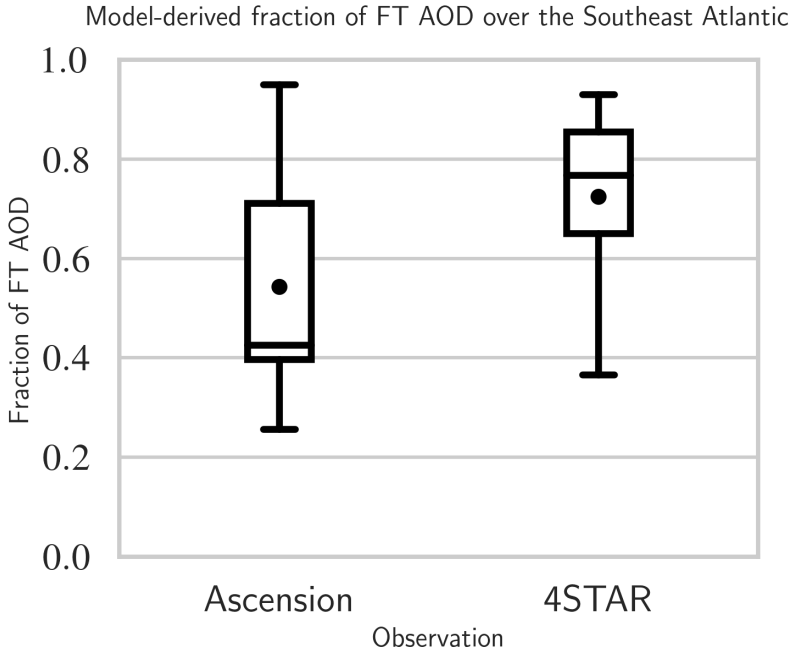

Figure 3.9: Model-derived fraction of FT AOD to TC AOD from WRF-AAM. A fraction of 1 means that aerosol loading is completely in the FT. The box-whisker plot shows the 10th (lower whisker), 25th (lower quartile), 50th (median), 75th (upper quartile), and 90th (upper whisker) percentiles of fraction of FT AOD. The dark circle represents the mean fraction.

We can infer from figure 3.9 that a majority of the Total Column (TC) Aerosol Optical Depth (AOD) is concentrated in the Free Troposphere (FT), exceeding 50%. Over the SEA region, the mean ratio of FT AOD to TC AOD represented by the model exhibits significant spatial variability for the entire campaign dataset. Subsequently, the model-derived ratio is employed to estimate the FT AOD contribution from the AERONET and 4STAR observations, which is shown in Figure 3.10. One distinct feature is the maximum loading between the bounding box (4 S - 10S and 7W - 4E). At Ascension Island, we observe a mean FT AOD of approximately 0.2 with considerably higher loading closer to the coast of Namibia.

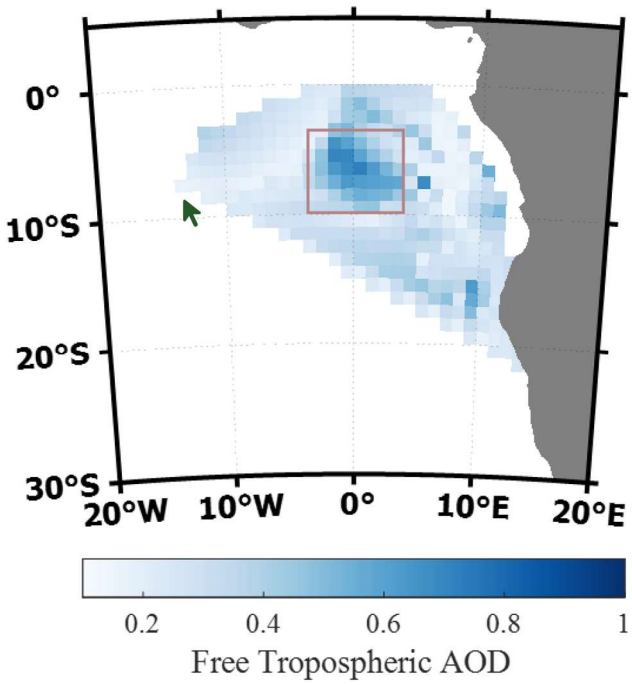

Figure 3.10: Map showing the FT AOD over the SEA region. All individual 4STAR sky scans are shown while the mean aerosol age is represented for Ascension Island (Green Arrow). The bounding box shows the region of maximum FT AOD

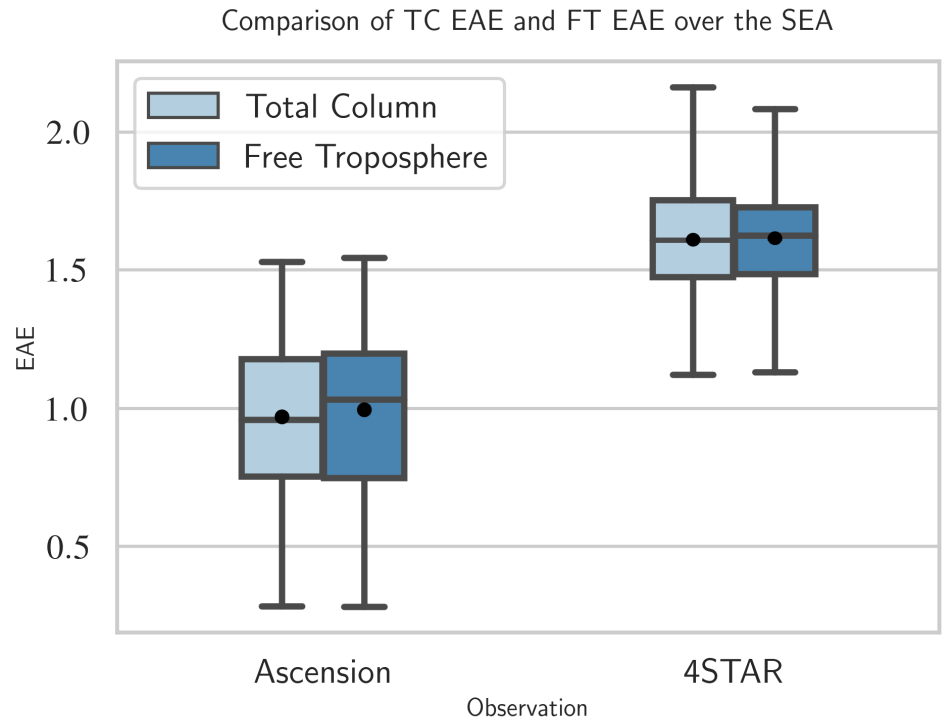

Figure 3.11: Comparison of EAE in the total column (TC) and free troposphere (FT) over the southeast Atlantic (SEA). The dark circle represents the mean EAE value.

Figure 3.12 shows the relationship between SSA, EAE, and aerosol age in the FT over the SEA, akin to the relationship illustrated in Figure 3.6. The FT SSA was calculated using Equation 2.10. After partitioning, the FT SSA values at Ascension Island ranged from 0.7 to 0.95, compared to the range of 0.8 to 1 observed in the total column, as shown in Figure 3. while the statistical pattern of EAE exhibited only a slight variation between the FT (mean = 1) and the TC (mean = 0.97). As the FT partitioning was limited to the SEA region, the statistics of the continental stations remained unchanged. To address the presence of large aerosol size and potentially other aerosol types in the FT indicated by observations with EAE < 1 and SSA > 0.9, the four EAE thresholds were employed to filter out such particles, results of which are shown in Figure 3.13.

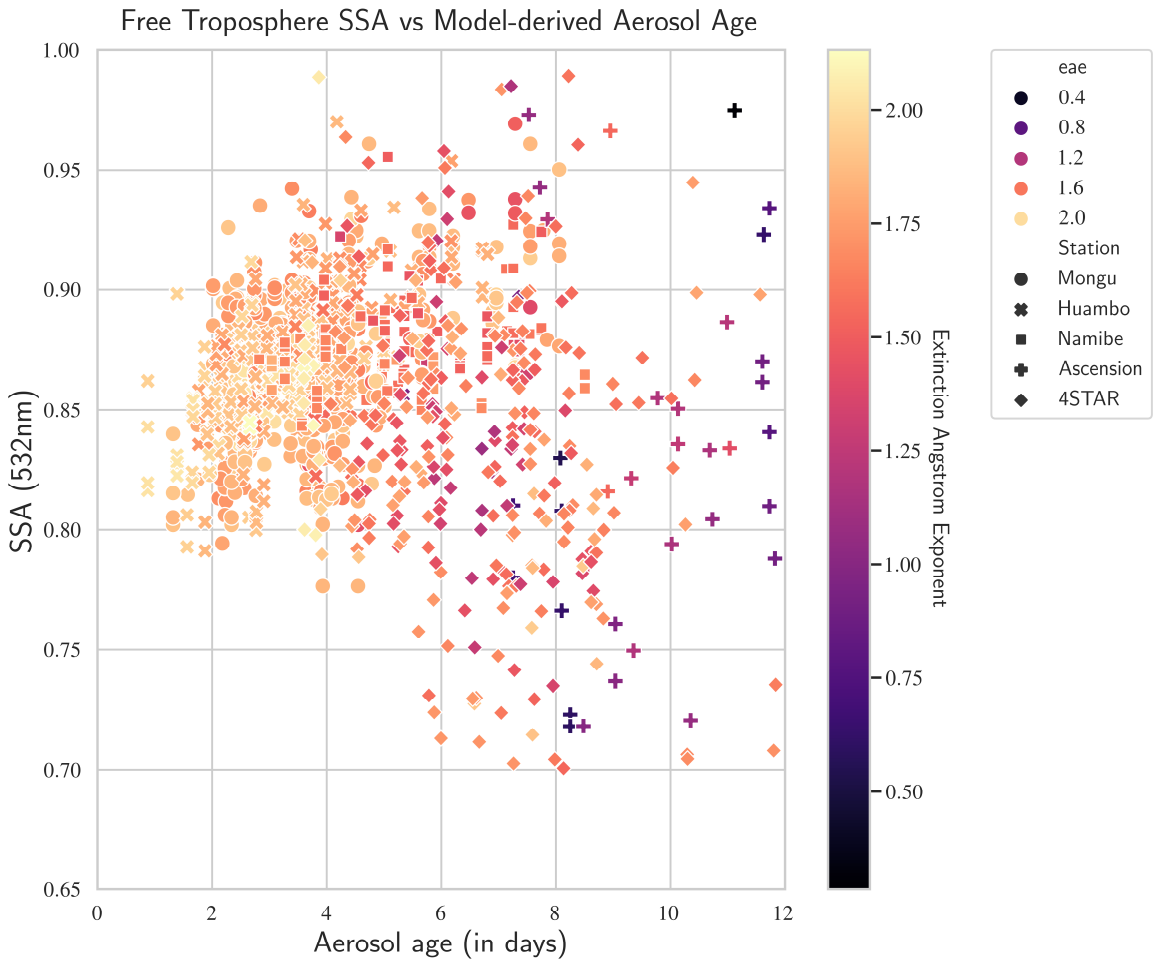

Figure 3.12: Scatterplot showing the relationship between SSA (markers), EAE (shading), and aerosol age in the free troposphere (FT). The different markers represent the stations while the colorbar shading represents the EAE.

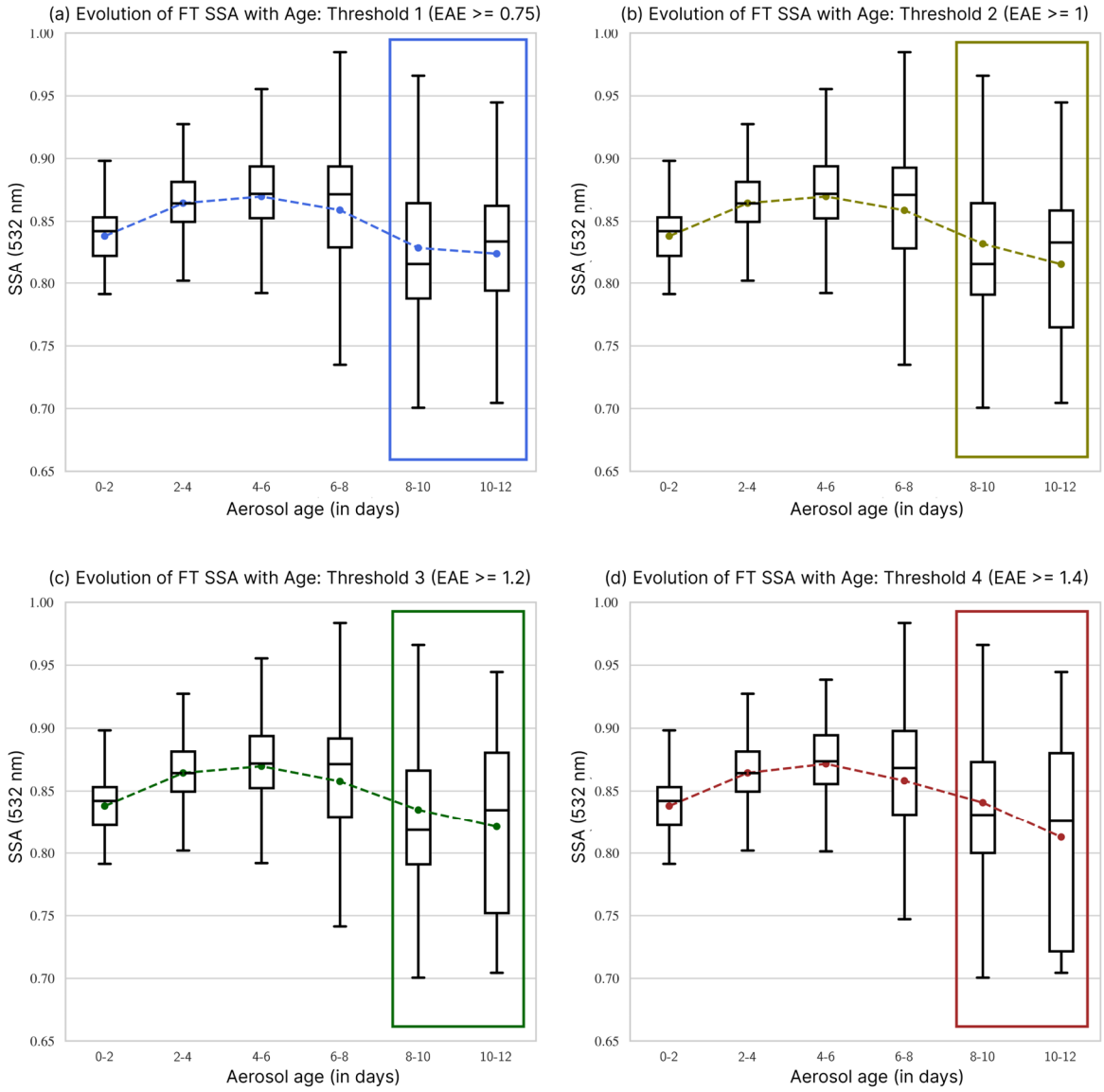

Figure 3.13: The evolution of SSA with age in the free troposphere (FT), filtered with (a) EAE >= 0.75, (b) EAE >= 1, (c) EAE >= 1.2, (d) EAE >= 1.4. The box-whisker plot shows the 10th (lower whisker), 25th (lower quartile), 50th (median), 75th (upper quartile), and 90th (upper whisker) percentiles of FT SSA. Colored dots represent the mean SSA with the dashed lines connecting the mean across the age bins.

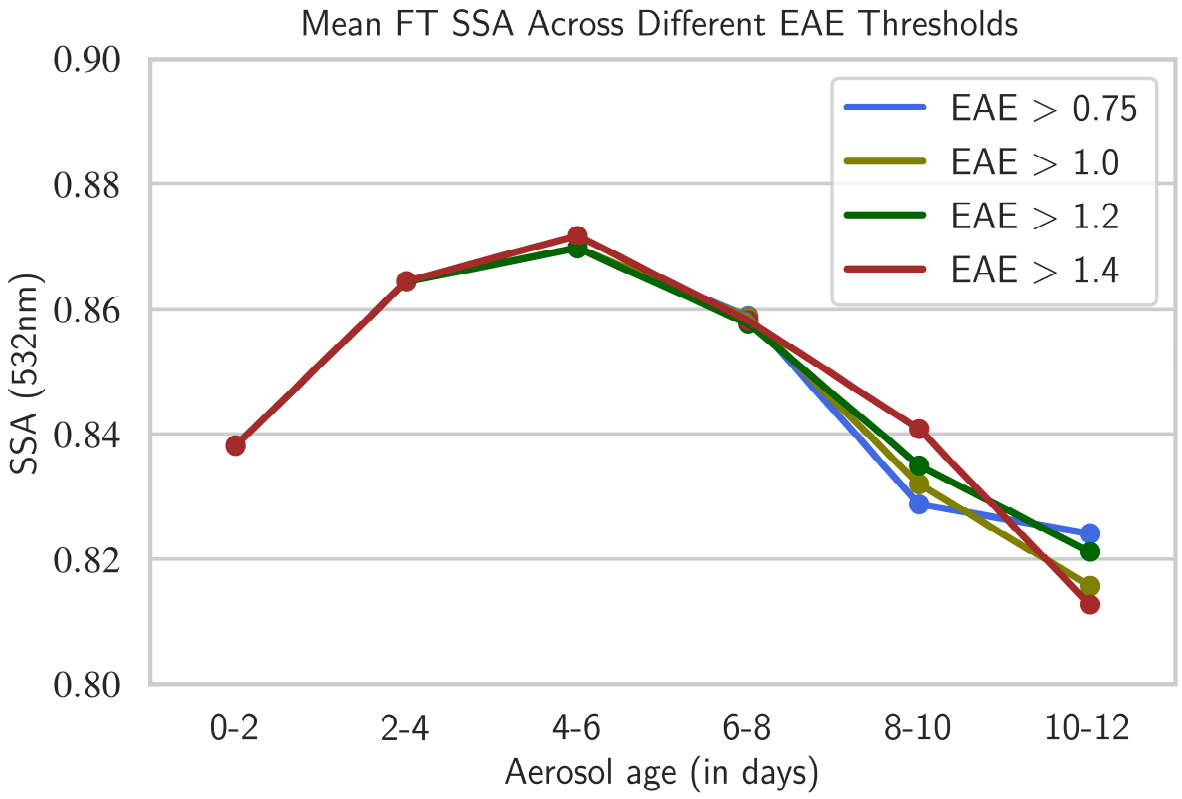

Figure 3.14: The mean free tropospheric FT SSA for all age bins across the four thresholds. The near-source observations in [0-2] and [2-4] age bins remained constant for all thresholds.

The mean FT SSA values for the first two aerosol age bins were constant at 0.838 and 0.86 for all four thresholds (Figure 3.14). For all thresholds, the [4-6] and [6-8] age bins exhibited only minor variations. It is, however, intriguing to observe a distinct temporal evolution of FT SSA for older aerosols, forming a clearly defined curve as we transition from the first threshold to the final threshold. The mean FT SSA for the 4th, 5^{th,} and 6th aerosol age bins are respectively 0.86, 0.84, and 0.81 in the final threshold. These values were slightly lower (2-5%) than the mean TC SSA values, suggesting a higher absorption capacity of biomass burning aerosols within the Free Troposphere (FT) in the Southeast Atlantic. This is further discussed in section 4.3.

Chapter 4

Discussion

4.1 Discussion; Model Representation of Single Scattering Albedo

Aerosol single scattering albedo (SSA) is an important parameter in deriving the radiative effects of aerosols (Chylek and Wong, 1995; Takemura et al. 2002; Satheesh et al. 2010) using columnar-resolved values of SSA. Climate models use SSA among other parameters to estimate the effective radiative forcing (ERF) of anthropogenic aerosols. However, there is significant disagreement between models, making these estimates of ERF from anthropogenic sources highly uncertain. There are many factors that can affect the accuracy of model simulations, such as emissions, aerosol mixing, and transport. By studying the differences between modeled and observed aerosol properties, we help modelers identify the sources of uncertainty and explore ways to reduce it. Evaluating these differences can ultimately improve the estimation of aerosol radiative forcing in climate models.

In this study, the regional model WRF-CAM5 was used to examine the representation of SSA in the southeast Atlantic region. The selection of WRF-CAM5 here was based on its advanced modeling features and improved parameterizations, whereas WRF-AAM, which is a simpler model, was only used to provide aerosol age estimate that is not achievable with WRF-CAM5. Figure 3.1a shows the comparison between modeled and observed total-column SSA over the study region.

Considering the mean of SSA derived from the model collocated with AERONET observations at Mongu, Huambo, Namibe, Ascension Island and from 4STAR observations respectively (shown in Table 3), we can see that the model slightly underestimates SSA on average. The biases between the modeled and observed SSA values are more pronounced over land. For instance, the model underestimated SSA values by 0.017 for Mongu and Huambo, 0.03 for Namibe, 0.016 at Ascension Island, and 0.011 from 4STAR observations on average.

The relatively low bias observed between WRF-CAM5 and observations could be attributed to the model's simulation of SSA at ambient relative humidity similar to observations from AERONET and 4STAR (Pistone et al., 2019; Doherty et al., 2022). We also looked at the longitudinal and latitudinal dependency of SSA. The model shows a slight longitudinal variation in average SSA (Figure 3.1b). Neither the model nor observations exhibited latitudinal dependence of SSA (not shown. Our model simulation focuses on the entire vertical column, however, the underestimation is consistent with the findings of Shinozuka et al., (2020) which showed that models underestimate SSA values in the free troposphere.

Another key detail is that the model-estimated SSA values were constrained within a narrow range of values from 0.80 - 0.89, compared to the wider range of 0.75 - 0.95 in the observations as in Figure 3.2. However, when we focus on AERONET stations individually, we observe that the model simulates a wider range of SSA (0.82 – 0.88) over land (Mongu and Namibe), compared to the narrower (0.84 – 0.88) SSA range at the coastal station, Namibe and over the southeast Atlantic Ocean (Ascension Island and 4STAR). Specifically, values of SSA from AERONET and 4STAR greater than 0.85 would be underestimated by WRF-CAM5 while values smaller are overestimated.

These results support the findings presented in section 4.3.1 of Doherty et al., (2022), which compared the model's predictions of aerosol properties to observational data along distinct flight paths during the ORACLES campaign. The report indicated that the WRF-CAM5 model estimated SSA values between 0.82-0.84 and 0.84-0.86 for the 2016 and 2018 missions, respectively. Doherty et al., (2022) suggest that the constraint of SSA by WRF-CAM5 is because the model does not account for the aging of organic aerosols and black carbon, and its estimated primary organic aerosol hygroscopicity is low ($\kappa = 0.1$). The correlation between the modeled SSA and observation is low (Table 4), suggesting that there is not a strong linear relationship between the two.

The behavior of the model agrees with results from similar model studies in the southern African region (Das et al., 2017; Shinozuka et al., 2020; Mallet et al., 2020; Doherty et al., 2022). The differences between modeled and observed SSA values may be attributed to inaccuracies in the model's parameterizations, which can include uncertainties in the aerosol size distribution or mixing state. While there is not yet a consensus in literatures on the cause of model bias, it is suggested that the underestimation is a result of discrepancies in emission inventories which impede the models from correctly representing the concentration, mass loading and properties of BBA (Mallet et al., 2020; Doherty et al., 2022). It is also possible that the models are not able to capture the true variability and complexity of the aerosol properties in the atmosphere, particularly in regards to effectively representing the long-range transport from continental Africa to the southeast Atlantic (Das et al., 2017; Doherty et al., 2022).

In order to reduce the bias between the models and observation, it is important to improve the model’s representation of aerosol size distribution, refractive indices, and mixing state as a

means to improve the quantification of aerosol mass extinction and absorption efficiency (Shinozuka et al., 2020).

4.2 Discussion; Estimates of Biomass Burning Aerosol Age

The mean aerosol age and extinction as forecast by the WRF-AAM model for a single day are shown in Figure 3.3 (a) and (b). Similar curtain plots were produced throughout the ORACLES campaign region during all three deployments. These daily forecasts were instrumental in the flight planning during ORACLES, with the team making opportunistic research flights that targeted specific smoke plumes and specific regions. Overlaying the curtain is the flight track of the P-3 aircraft. The figures provide information on the vertical variation in aerosol mean age and extinction across the region of observation and along each of the research flights.

The model simulates aerosol age at altitudes below 1000m to be significantly greater than in the free troposphere (FT), suggesting that these aerosols were not recently mixed from the burning source regions but have instead, taken a different transport pathway from the FT aerosols. In the FT, approximately above 1500m as discussed in section 2.5, the model simulates relatively younger aerosols with a mean age between 3 – 8 days in the lower FT (2 – 7 km) and up to 12 days in the mid FT (> 7km). The model shows maximum aerosol extinction in the lowest 1000m, which decreases with increasing height, reaching minimum extinction above 6km. This model representation of mean aerosol age and extinction is consistent across all three campaign years.

The map illustrated in Figure 3.4 shows the extinction-weighted average age at Ascension Island (identified with the green arrow cursor) and at the location of individual 4STAR sky scans across the three campaign deployments and does not represent the spatial or temporal variation as in the case of the curtain plots. The samples at Ascension Island constitute the oldest aerosols with

ages between 8 – 12 days. As mentioned earlier, the ORACLES team made specific flight plans to target younger, fresh smoke plumes, which we can see in the low aerosol age (3 – 6 days) for some individual 4STAR sky scans within the interior of the triangular flight region.

Over the continent, the model shows in Figure 3.5, the youngest aerosol age in southern Africa in the region of biomass burning, with samples ranging from less than a day, up to six days at Mongu and Huambo. The reason for the younger aerosols at Huambo compared to Mongu, despite the proximity of Mongu to intense burning sources, is that the model simulates smaller fires, which are located closer to Huambo but further away from the core of the burning. The average aerosol age along the Namibian coast is 5 days, which is consistent with the transport of smoke aerosols from the source region. This is further supported by the low active fire counts at Namibe during the campaign period. The wide range of extinction-mean aerosol age for 4STAR sky scans can be attributed to several factors, including geographical location, flight altitude, and flight objectives. The aerosol age tends to be higher when the 4STAR conducted sky scans at lower altitudes since the age is averaged vertically. Furthermore, sky scans made at farther distances from the coast showed aged aerosols. Most of the samples at Ascension Island showed well-aged aerosols both in the vertical column and the FT, consistent with the required long-range transport from the source region. This is further discussed in section 4.3 on the evolution of BBA as they age.

The findings presented here significantly contribute to our understanding of the dynamics in the SEA with regards to atmospheric aerosols. The results indicate that BBA particles transported over long distances from the source region have aged and may have undergone chemical or physical processes due to their prolonged exposure in the atmosphere.

4.3 Discussion; Evolution of Biomass Burning Aerosols Single Scattering Albedo (SSA) with Age

In the previous section, we showed how the model predicts biomass burning aerosols (BBA) age as they are transported from continental Africa to the southeast Atlantic (SEA). Subsequently, we investigated the changes in their optical properties during this transport and aging process. The analysis primarily focuses on single scattering albedo (SSA), due to its importance in the radiative balance and its relevance to the study's objective. We also apply the extinction Angstrom exponent (EAE) as an indicator of potential contributions to the total column of coarse mode aerosols whether from intrusion of giant-mode sea salt aerosols from the MBL or from transport of coarse-mode desert dust in the FT or elsewhere. SSA provides insights into the absorptivity of particles, while EAE provides insights into the size of particles.

From Figure 3.6, we see that fresh BBA samples ($\leq$ 4 days) exhibit high absorption, as indicated by their relatively low SSA values (0.8 – 0.9), consistent with previous research (Haywood et al., 2003; Abel et al., 2003; Leahy et al., 2007). The high EAE values observed within this age range are indicative of the predominance of fine aerosol particles. Aerosol samples with ages between 4-8 days, predominantly from 4STAR and Namibe, exhibit a wide range of SSA and EAE values, suggesting high variability in their properties (Figure 3.6). The oldest group of aerosol samples collected at Ascension Island also displays a broad range of SSA and EAE values, indicating the prevalence of larger particle sizes. There were instances where a small number of 4STAR retrievals showed both low SSA values ($<$ 0.8) and low EAE values ($\leq$ 1.0), suggesting the possibility of dust or a mixture of coarse marine aerosol particles with BBA. The measurements over the SEA indicate varying aerosol sizes and degrees of absorption, as evidenced by the broad range of SSA and EAE values obtained from 4STAR and Ascension Island observations.

4.3.1 Attempts to separate BL contributions from TC observations

With the low EAE values sampled in the total column over the SEA as shown in Figure 3.6, we need to accept the likelihood of mixing from the BL or sources that could influence the intensive properties of various types of aerosols within the atmospheric column. This is particularly important due to the mixing of BBA into the boundary layer over the SEA as reported in Zuidema et al. (2018) and Leblanc et al. (2020) and the occasional long-range transport of desert dust in the FT. In order to eliminate those observations indicating large particle sizes that may be related to coarse marine aerosols in the total atmospheric column, we use two techniques. First, we attempt to isolate the BL contributions, using a model-derived ratio of aerosol loading in the BL and FT as detailed in section 2.5. Secondly, we assessed varying EAE thresholds as a proven way to eliminate layers containing large particles as such layers would indicate a likelihood of coarse-mode aerosol contribution. In our analysis, we applied the EAE thresholds, first to the TC, to observe how the SSA changes after filtering different EAE values in the TC. We also applied the EAE thresholds to the FT observation after partitioning as we know that the model ratio can be subject to bias and the model cannot guarantee accurate representation of aerosol loading in the region.

The application of various EAE thresholds to the total column observations revealed a distinct change in the SSA with age. The box-whisker plot (Figure 3.7) displays consistent statistics across all four thresholds for the first three age bins ([0-2], [2-4], [4-6]), which represent near-source samples (Mongu, Huambo). The mean SSA values were approximately 0.84, 0.86, and 0.87, respectively (Figure 3.8). Since the distribution stayed the same across all thresholds for these three age bins, it means that the EAE of these samples is greater than 1.4, indicating the

biomass burning aerosols as suggested in Eck et al., 1999. The implementation of thresholds only influenced the distribution of the aged aerosols over the SEA. With each level of the EAE threshold, a change in the distribution of samples can be observed in the [6-8], [8-10], and [10-12] age categories. The shift in the distribution becomes more evident after the fourth threshold is applied. This result shows two things - Firstly, that there are coarse mode aerosol contributions in the atmospheric column over the SEA. Secondly, after excluding cases with coarse mode aerosols, there is noticeable evolution in the remaining BBA SSA as they age in the atmosphere. After applying the 4th threshold (as illustrated in Figure 3.7d), SSA peaks between 6 to 8 days, then decreases afterward. However, it should be noted that increasing the EAE threshold from 1.2 to 1.4 leads to a substantial decrease in the number of samples in the [10-12] age bin. This suggests that the recommendation of EAE of 1.5 and greater by Eck et al., 1999 for BBA may only apply to freshly emitted BBA as we have seen here and not to aged BBA.

With the model ratio applied to observations, we observed that typically over 50% of the aerosol AOD exists in the FT over the SEA, as shown in Figure 3.9. This includes all observations taken at Ascension Island and during 4STAR sky scans at lower altitudes (below 1500m). This fraction of FT AOD is consistent with findings from other models in Chang et al.'s 2022 study. According to Figure 8 from Leblanc et al.'s 2020 study, there appears to be limited spatial dependence of EAE above cloud in the SEA. As such, it is expected that the EAE estimated from FT AOD in this study will not significantly differ from the above cloud EAE values from 4STAR, reported in Leblanc et al.'s study. Although the EAE values estimated in the FT from 4STAR appear to be consistent with those in Leblanc et al.'s 2020 study, which was expected since 4STAR frequently sampled the FT, the unexpectedly good agreement between the EAE in the FT and EAE in the TC at Ascension Island shown in Figure 3.11 may be due to model uncertainties or the equal

partitioning of AOD at all wavelengths in our analysis. As evident from in situ and 4STAR observations during the ORACLES campaign (Pistone et al., 2019; Leblanc et al., 2020), the EAE values in the SEA region are predominantly indicative of biomass burning (≥ 1.2).

Comparing Figure 3.6 with Figure 3.12, there is a difference in the SSA and EAE of the samples aged around 10 days from Ascension Island. Figure 3.12 shows that after partitioning, these samples have significantly lower SSA and high EAE, indicating the desired isolation of fine-absorbing aerosols or BBA in the FT. The aged aerosols between [10-12] days with high SSA (> 0.90) with low EAE could be dust aerosols which were occasionally sampled at Ascension Island.

After considering the potential for the presence of other types of aerosols in the FT over Ascension Island, we proceeded to apply the EAE thresholds to the FT observations over the SEA region. Here we see a change in FT SSA values over the SEA as we vary the level of isolation of large particles (Figure 3.13). Average FT SSA peaks around 4-6 days along the coast before decreasing over the ocean for aerosols aged beyond 7 days, suggesting an elevated absorptivity of BBA in the FT over the ocean. The findings of this study are consistent with the results reported by Dobracki et al. (2022) for the ORACLES campaign region, highlighting the relationship between processes such as condensation, coagulation, aerosol age, and particle size. Dobracki et al. (2022) observed that the size of black carbon-containing BBA tends to increase with age, while the ratio of organic aerosols to black carbon (OA:BC) decreases. Their findings revealed a decrease in SSA from 0.89 to 0.865 following a 35% reduction in the OA:BC ratio. The results from our study presented here also agree with Sedlacek et al.'s (2022) study on the aging of particles containing black carbon (BC), which reported that BB-BC particles lose a significant portion of their coating material after aging for about 2-3 days, likely due to processes such as oxidation and

other secondary reactions (see Figure 1.9). These changes in coating thickness have a direct impact on the optical properties of BBA. This is according to Sedlacek et al. (2022) who observed an increase in BB SSA from ~0.8 to ~0.9 in the fest few hours, then a decrease in BB SSA from ~ 0.9 at 4 days old to ~0.83 after 10 days.

4.4 Conclusion

In this study, we introduced a novel approach to analyze the change in the optical properties of BBA associated with long-range transport from continental southern Africa to the SEA region. Our analysis combines data from ground-based AERONET and airborne 4STAR, gathered during the three deployments of ORACLES, with model output from WRF-CAM5 and WRF-AAM to investigate changes in SSA and EAE over time.

Previous studies on BBA from southern Africa have primarily focused on either continental southern Africa as in (Abel et al., 2003; Eck et al., 2003; Queface et al., 2011; Eck et al., 2013) or over the ocean in the SEA as in (Meyer et al., 2013; de Graaf et al., 2014; Zuidema et al., 2018; Pistone et al., 2019; Redemann et al., 2021). However, in this study, we take a more comprehensive approach by combining ground-based AERONET measurements from sites located in the source region of biomass burning with airborne 4STAR measurements over the ocean. This allows us to provide a more holistic study of the entire transportation pathway of BBA from the burning source to the SEA.

Through the use of model tracers in the WRF-AAM model, we calculated the aerosol age, which represents the time since the aerosols were emitted. This allows us to examine the changes in SSA of southern African BBA as they are transported over time, both in the total atmospheric column and in the free troposphere.

In general, the observations and WRF-CAM5 show a longitudinal variation in SSA that corresponds with the model-derived aerosol age and aligns with the pathway of transport from the continent. Aerosol age was calculated from model-released tracers that were tracked along a 14-day transport. Throughout 2016, 2017, and 2018, we observed a consistent variation in the mean

SSA, increasing away from the source region with the minimum value at Mongu and maximum mean SSA at Ascension Island. The representation of young aerosols, mostly below 5 days old, at Mongu and Huambo by WRF-AAM reveals that the model sufficiently captures the fires within the emission source regions. The oldest aerosols were sampled at Ascension Island.

Due to uncertainties regarding the regional model's ability to efficiently represent the properties of BBA over the ocean, we applied both a model-based BL-FT partitioning and EAE-based threshold approach to explain the evolution of SSA. Our aim was to isolate the potential contribution of BL marine aerosols to the total column, thereby focusing our study on the free tropospheric BBA. Applying EAE thresholds to the total column observations revealed a decrease in SSA over the ocean after reaching the peak along the coastline around 6-8 days. After model-based partitioning of BL from the TC, the analysis revealed a distinct evolution of SSA in the FT, going from ~0.84 in the first few days (< 2 days), reaching its maximum (~0.87) around 4-6 days, then decreasing to ~0.81 after 10 days which supports the findings from Dobracki et al., (2022) and Sedlacek et al., (2022). Although, there were still few cases of very high SSA with low EAE in locations where the model predicted aged aerosols. Either the presence of other aerosol types such as transported Saharan dust aerosols or uncertainty in the model simulations at Ascension Island can explain these scenarios.

These results allow us to address the first scientific question that asked to identify discernible changes in optical properties of BBA across the SEA region. The study region exhibits variations in the SSA of BBA that have significant implications for the radiation balance, with high absorptivity observed upon initial emission from Mongu or Huambo, followed by reduced absorptivity during intermittent stages of transport, and a subsequent increase in absorptivity over

the ocean. We suggest that the changes observed are primarily caused by chemical or physical processes in the atmosphere (Sedlacek et al., 2022), but we cannot identify which specific processes are contributing to the evolution found in this study.

To address science question 2, we compared WRF-CAM5's representation of SSA against observation and found low correlation values. The model showed only a slight bias (ranging from 0.01 to 0.03), which aligns with the uncertainty range observed in both 4STAR and AERONET retrievals. The underestimation and constraint of SSA by WRF-CAM5 highlight the importance of improving the representation of mass loading and extinction in regional climate models. This will enable better capture of the intensive properties of BBA in the SEA region.

One limitation of this analysis is the selection of 1500m to represent the BL height over the ocean. Despite being consistent with some models, we do not account for any spatial variation in BL height across the entire domain of the SEA that may be due to the changes in meteorological conditions and sea-surface temperature. Another important caveat to this study is the uncertainties in the model simulations. Over some parts of the SEA, WRF-AAM didn't accurately represent the vertical distribution of BBA and was unable to accurately account for the mixing of boundary layer aerosols. Having BBA with low EAE and high SSA in the FT would be considered implausible. Therefore, the FT partitioning from the model may have a lot of uncertainty. Also, this analysis adopted model parameters only pertaining to smoke aerosols and didn't consider the model simulation of other aerosol types over the ocean.

4.5 Future Work

One possible future direction would be to explore alternative approaches for separating the vertically resolved AERONET and 4STAR observations over the SEA. An option to consider is to obtain the WRF-CAM5 boundary layer products for partitioning, then compare the results from that study to the present findings. As a part of future research, I plan to investigate the changes in aerosol properties derived from five different models: WRF-CAM5, GEOS, ALADDIN, CESM, and E3SM. The primary objective of the analysis would be to determine whether these regional climate models can capture a similar evolution trend in optical properties, as demonstrated in this study.

The combination of observational data from various in situ instruments such as the Particle Soot Absorption Photometer (PSAP), Aerosol Mass Spectrometer (AMS), and Nephelometers would provide a distinct approach to augment this study. Using in situ observations could provide more accurate and detailed information on the changes in aerosol properties over time. Therefore, combining the findings presented here with analyses of satellite retrievals and in situ data, as well as data from other campaigns like CLARIFY and LASIC, could enhance our understanding of the evolution of BBA optical characteristics in the SEA region during the ORACLES campaign period.

The broader implications of this work are particularly to help improve model performance. As mentioned earlier, current models struggle to accurately place BBA in either the FT or BL. Hence, further analysis will provide insights into the spatial and temporal evolution of SSA which will help models better constrain aerosol properties. This knowledge can further explain aerosol-cloud interactions in the region, potentially bridging the gap in understanding why models continue

to struggle in replicating the BL-FT mixing. The results from the future work would be applied to the completion of a doctoral dissertation.

References

Ackerman, A. S., Toon, O. B., Taylor, J. P., Johnson, D. W., Hobbs, P. V., & Ferek, R. J. (2000). Effects of Aerosols on Cloud Albedo: Evaluation of Twomey's Parameterization of Cloud Susceptibility Using Measurements of Ship Tracks. *Journal of the Atmospheric Sciences*, *57*(16), 2684-2695. https://doi.org/10.1175/1520-0469(2000)057<2684:Eoaoca>2.0.Co;2

Adebiyi, A., Kok, J. F., Murray, B. J., Ryder, C. L., Stuut, J.-B. W., Kahn, R. A., Knippertz, P., Formenti, P., Mahowald, N. M., Pérez García-Pando, C., Klose, M., Ansmann, A., Samset, B. H., Ito, A., Balkanski, Y., Di Biagio, C., Romanias, M. N., Huang, Y., & Meng, J. (2023). A review of coarse mineral dust in the Earth system. *Aeolian Research*, *60*, 100849. https://doi.org/https://doi.org/10.1016/j.aeolia.2022.100849

Adebiyi, A. A., & Zuidema, P. (2016). The role of the southern African easterly jet in modifying the southeast Atlantic aerosol and cloud environments. *Quarterly Journal of the Royal Meteorological Society*, *142*(697), 1574-1589. https://doi.org/https://doi.org/10.1002/qj.2765

Adebiyi, A. A., Zuidema, P., & Abel, S. J. (2015). The Convolution of Dynamics and Moisture with the Presence of Shortwave Absorbing Aerosols over the Southeast Atlantic. *Journal of Climate*, *28*(5), 1997-2024. https://doi.org/10.1175/jcli-d-14-00352.1

Aladodo, S. S., Akoshile, C. O., Ajibola, T. B., Sani, M., Iborida, O. A., & Fakoya, A. A. (2022). Seasonal Tropospheric Aerosol Classification Using AERONET Spectral Absorption Properties in African Locations. *Aerosol Science and Engineering*, *6*(3), 246-266. https://doi.org/10.1007/s41810-022-00140-x

Albrecht, B. A. (1989). Aerosols, Cloud Microphysics, and Fractional Cloudiness. *Science*, *245*(4923), 1227-1230. https://doi.org/doi:10.1126/science.245.4923.1227

Andreae, M. O., & Gelencsér, A. (2006). Black carbon or brown carbon? The nature of light-absorbing carbonaceous aerosols. *Atmos. Chem. Phys.*, *6*(10), 3131-3148. https://doi.org/10.5194/acp-6-3131-2006

Andreae, M. O., & Rosenfeld, D. (2008). Aerosol–cloud–precipitation interactions. Part 1. The nature and sources of cloud-active aerosols. *Earth-Science Reviews*, *89*(1), 13-41. https://doi.org/https://doi.org/10.1016/j.earscirev.2008.03.001

Baars, H., Radenz, M., Floutsi, A. A., Engelmann, R., Althausen, D., Heese, B., Ansmann, A., Flament, T., Dabas, A., Trapon, D., Reitebuch, O., Bley, S., & Wandinger, U. (2021). Californian Wildfire Smoke Over Europe: A First Example of the Aerosol Observing Capabilities of Aeolus Compared to Ground-Based Lidar. *Geophysical Research Letters*, *48*(8), e2020GL092194. https://doi.org/https://doi.org/10.1029/2020GL092194

Bauer, S. E., Koch, D., Unger, N., Metzger, S. M., Shindell, D. T., & Streets, D. G. (2007). Nitrate aerosols today and in 2030: a global simulation including aerosols and tropospheric ozone. *Atmos. Chem. Phys.*, *7*(19), 5043-5059. https://doi.org/10.5194/acp-7-5043-2007

Bellouin, N., Quaas, J., Gryspeerdt, E., Kinne, S., Stier, P., Watson-Parris, D., Boucher, O., Carslaw, K. S., Christensen, M., Daniau, A.-L., Dufresne, J.-L., Feingold, G., Fiedler, S., Forster, P., Gettelman, A., Haywood, J. M., Lohmann, U., Malavelle, F., Mauritsen, T., . . . Stevens, B. (2020). Bounding Global Aerosol Radiative Forcing of Climate Change. *Reviews of Geophysics*, *58*(1), e2019RG000660. https://doi.org/https://doi.org/10.1029/2019RG000660

Bergstrom, R. W., Pilewskie, P., Russell, P. B., Redemann, J., Bond, T. C., Quinn, P. K., & Sierau, B. (2007). Spectral absorption properties of atmospheric aerosols. *Atmos. Chem. Phys.*, *7*(23), 5937-5943. https://doi.org/10.5194/acp-7-5937-2007

Bhattacharjee, P. S., Zhang, L., Baker, B., Pan, L., Montuoro, R., Grell, G. A., & McQueen, J. T. (2023). Evaluation of Aerosol Optical Depth Forecasts from NOAA's Global Aerosol Forecast Model (GEFS-Aerosols). *Weather and Forecasting*, *38*(2), 225-249. https://doi.org/https://doi.org/10.1175/WAF-D-22-0083.1

Bilal, M., Nichol, J. E., Nazeer, M., Shi, Y., Wang, L., Kumar, K. R., Ho, H. C., Mazhar, U., Bleiweiss, M. P., Qiu, Z., Khedher, K. M., & Lolli, S. (2019). Characteristics of Fine Particulate Matter (PM2.5) over Urban, Suburban, and Rural Areas of Hong Kong. *Atmosphere*, *10*(9), 496. https://www.mdpi.com/2073-4433/10/9/496

Bond, T. C. (2001). Spectral dependence of visible light absorption by carbonaceous particles emitted from coal combustion. *Geophysical Research Letters*, *28*(21), 4075-4078.

Bond, T. C., & Bergstrom, R. W. (2006). Light Absorption by Carbonaceous Particles: An Investigative Review. *Aerosol Science and Technology*, *40*(1), 27-67. https://doi.org/10.1080/02786820500421521

Bond, T. C., Doherty, S. J., Fahey, D. W., Forster, P. M., Berntsen, T., DeAngelo, B. J., Flanner, M. G., Ghan, S., Kärcher, B., Koch, D., Kinne, S., Kondo, Y., Quinn, P. K., Sarofim, M. C., Schultz, M. G., Schulz, M., Venkataraman, C., Zhang, H., Zhang, S., . . . Zender, C. S. (2013). Bounding the role of black carbon in the climate system: A scientific assessment. *Journal of Geophysical Research: Atmospheres*, *118*(11), 5380-5552. https://doi.org/10.1002/jgrd.50171

Bond, T. C., Streets, D. G., Yarber, K. F., Nelson, S. M., Woo, J.-H., & Klimont, Z. (2004). A technology-based global inventory of black and organic carbon emissions from combustion. *Journal of Geophysical Research: Atmospheres*, *109*(D14). https://doi.org/https://doi.org/10.1029/2003JD003697

Boucher, O. (2015). Atmospheric Aerosols. In *Atmospheric Aerosols: Properties and Climate Impacts* (pp. 9-24). Springer Netherlands. https://doi.org/10.1007/978-94-017-9649-1_2

Bowman, D. M. J. S., Balch, J. K., Artaxo, P., Bond, W. J., Carlson, J. M., Cochrane, M. A., D'Antonio, C. M., DeFries, R. S., Doyle, J. C., Harrison, S. P., Johnston, F. H., Keeley, J. E., Krawchuk, M. A., Kull, C. A., Marston, J. B., Moritz, M. A., Prentice, I. C., Roos, C. I., Scott, A. C., . . . Pyne, S. J. (2009). Fire in the Earth System. *Science*, *324*(5926), 481-484. https://doi.org/doi:10.1126/science.1163886

Bretherton, C. S., & Park, S. (2009). A New Moist Turbulence Parameterization in the Community Atmosphere Model. *Journal of Climate*, *22*(12), 3422-3448. https://doi.org/10.1175/2008jcli2556.1

Campbell, P., Zhang, Y., Wang, K., Leung, R., Fan, J., Zheng, B., Zhang, Q., & He, K. (2017). Evaluation of a multi-scale WRF-CAM5 simulation during the 2010 East Asian Summer Monsoon. *Atmospheric Environment*, *169*, 204-217. https://doi.org/https://doi.org/10.1016/j.atmosenv.2017.09.008

Cappa, C. D., Lim, C. Y., Hagan, D. H., Coggon, M., Koss, A., Sekimoto, K., de Gouw, J., Onasch, T. B., Warneke, C., & Kroll, J. H. (2020). Biomass-burning-derived particles from a wide variety of fuels – Part 2: Effects of photochemical aging on particle optical and chemical properties. *Atmos. Chem. Phys.*, *20*(14), 8511-8532. https://doi.org/10.5194/acp-20-8511-2020

Chang, I., Gao, L., Flynn, C. J., Shinozuka, Y., Doherty, S. J., Diamond, M. S., Longo, K. M., Ferrada, G. A., Carmichael, G. R., Castellanos, P., da Silva, A. M., Saide, P. E., Howes, C., Xue, Z., Mallet, M., Govindaraju, R., Wang, Q., Cheng, Y., Feng, Y., . . . Redemann, J. (2022). On the differences in the vertical distribution of modeled aerosol optical depth over the southeast Atlantic. *Atmos. Chem. Phys. Discuss.*, *2022*, 1-42. https://doi.org/10.5194/acp-2022-496

Che, H., Stier, P., Gordon, H., Watson-Parris, D., & Deaconu, L. (2021). Cloud adjustments dominate the overall negative aerosol radiative effects of biomass burning aerosols in UKESM1 climate model simulations over the south-eastern Atlantic. *Atmos. Chem. Phys.*, *21*(1), 17-33. https://doi.org/10.5194/acp-21-17-2021

Chen, T., Rossow, W. B., & Zhang, Y. (2000). Radiative Effects of Cloud-Type Variations. *Journal of Climate*, *13*(1), 264-286. https://doi.org/10.1175/1520-0442(2000)013<0264:Reoctv>2.0.Co;2

Chen, Y., Cheng, Y., Ma, N., Wei, C., Ran, L., Wolke, R., Größ, J., Wang, Q., Pozzer, A., Denier van der Gon, H. A. C., Spindler, G., Lelieveld, J., Tegen, I., Su, H., & Wiedensohler, A. (2020). Natural sea-salt emissions moderate the climate forcing of anthropogenic nitrate. *Atmos. Chem. Phys.*, *20*(2), 771-786. https://doi.org/10.5194/acp-20-771-2020

Chylek, P., Lee, J. E., Romonosky, D. E., Gallo, F., Lou, S., Shrivastava, M., Carrico, C. M., Aiken, A. C., & Dubey, M. K. (2019). Mie Scattering Captures Observed Optical Properties of Ambient Biomass Burning Plumes Assuming Uniform Black, Brown, and Organic Carbon Mixtures. *Journal of Geophysical Research: Atmospheres*, *124*(21), 11406-11427. https://doi.org/https://doi.org/10.1029/2019JD031224

Chylek, P., & Wong, J. (1995). Effect of absorbing aerosols on global radiation budget. *Geophysical Research Letters*, *22*(8), 929-931. https://doi.org/https://doi.org/10.1029/95GL00800

Cotterell, M. I., Szpek, K., Haywood, J. M., & Langridge, J. M. (2020). Sensitivity and accuracy of refractive index retrievals from measured extinction and absorption cross sections for mobility-selected internally mixed light absorbing aerosols. *Aerosol Science and Technology*, *54*(9), 1034-1057. https://doi.org/10.1080/02786826.2020.1757034

Dobracki, A., Zuidema, P., Howell, S., Saide, P., Freitag, S., Aiken, A. C., Burton, S. P., Sedlacek Iii, A. J., Redemann, J., & Wood, R. (2022). An attribution of the low single-scattering albedo of biomass-burning aerosol over the southeast Atlantic. *Atmos. Chem. Phys. Discuss.*, *2022*, 1-40. https://doi.org/10.5194/acp-2022-501

Doherty, S. J., Saide, P. E., Zuidema, P., Shinozuka, Y., Ferrada, G. A., Gordon, H., Mallet, M., Meyer, K., Painemal, D., Howell, S. G., Freitag, S., Dobracki, A., Podolske, J. R., Burton, S. P., Ferrare, R. A., Howes, C., Nabat, P., Carmichael, G. R., da Silva, A., . . . Redemann, J. (2022). Modeled and observed properties related to the direct aerosol radiative effect of biomass burning aerosol over the southeastern Atlantic. *Atmos. Chem. Phys.*, *22*(1), 1-46. https://doi.org/10.5194/acp-22-1-2022

Dong, Y. (2020). Untangling aerosols from the sky with sunphotometers. *Nature Reviews Earth & Environment*, *1*(8), 387-387. https://doi.org/10.1038/s43017-020-0086-2

Dubovik, O., Holben, B., Eck, T. F., Smirnov, A., Kaufman, Y. J., King, M. D., Tanré, D., & Slutsker, I. (2002). Variability of Absorption and Optical Properties of Key Aerosol Types Observed in Worldwide Locations. *Journal of the Atmospheric Sciences*, *59*(3), 590-608. https://doi.org/10.1175/1520-0469(2002)059<0590:Voaaop>2.0.Co;2

Dunagan, S. E., Johnson, R., Zavaleta, J., Russell, P. B., Schmid, B., Flynn, C., Redemann, J., Shinozuka, Y., Livingston, J., & Segal-Rosenhaimer, M. (2013). Spectrometer for Sky-Scanning Sun-Tracking Atmospheric Research (4STAR): Instrument Technology. *Remote Sensing*, *5*(8), 3872-3895. https://www.mdpi.com/2072-4292/5/8/3872

Eck, T. F., Holben, B. N., Giles, D. M., Slutsker, I., Sinyuk, A., Schafer, J. S., Smirnov, A., Sorokin, M., Reid, J. S., Sayer, A. M., Hsu, N. C., Shi, Y. R., Levy, R. C., Lyapustin, A., Rahman, M. A., Liew, S.-C., Salinas Cortijo, S. V., Li, T., Kalbermatter, D., . . . Aldrian, E. (2019). AERONET Remotely Sensed Measurements and Retrievals of Biomass Burning Aerosol Optical Properties During the 2015 Indonesian Burning Season. *Journal of Geophysical Research: Atmospheres*, *124*(8), 4722-4740. https://doi.org/https://doi.org/10.1029/2018JD030182

Eck, T. F., Holben, B. N., Reid, J. S., Mukelabai, M. M., Piketh, S. J., Torres, O., Jethva, H. T., Hyer, E. J., Ward, D. E., Dubovik, O., Sinyuk, A., Schafer, J. S., Giles, D. M., Sorokin, M., Smirnov, A., & Slutsker, I. (2013). A seasonal trend of single scattering albedo in southern African biomass-burning particles: Implications for satellite products and estimates of emissions for the world's largest biomass-burning source. *Journal of Geophysical Research: Atmospheres*, *118*(12), 6414-6432. https://doi.org/https://doi.org/10.1002/jgrd.50500

Eck, T. F. H., B.N.; Reid, J.S.; Dubovik, O.; Smirnov, A.; O'Neill, N.T.; Slutsker, I.; Kinne, S. (1999). Wavelength dependence of the optical depth of biomass burning, urban, and desert dust aerosols. *Journal of Geophysical Research: Atmospheres*, *104*(D24), 31333-31349. https://doi.org/https://doi.org/10.1029/1999JD900923

Fast, J. D., Gustafson Jr., W. I., Easter, R. C., Zaveri, R. A., Barnard, J. C., Chapman, E. G., Grell, G. A., & Peckham, S. E. (2006). Evolution of ozone, particulates, and aerosol direct radiative forcing in the vicinity of Houston using a fully coupled meteorology-chemistry-aerosol model. *Journal of Geophysical Research: Atmospheres*, *111*(D21). https://doi.org/https://doi.org/10.1029/2005JD006721

Feng, Y., Ramanathan, V., & Kotamarthi, V. R. (2013). Brown carbon: a significant atmospheric absorber of solar radiation? *Atmos. Chem. Phys.*, *13*(17), 8607-8621. https://doi.org/10.5194/acp-13-8607-2013

Formenti, P., D'Anna, B., Flamant, C., Mallet, M., Piketh, S. J., Schepanski, K., Waquet, F., Auriol, F., Brogniez, G., Burnet, F., Chaboureau, J.-P., Chauvigné, A., Chazette, P., Denjean, C., Desboeufs, K., Doussin, J.-F., Elguindi, N., Feuerstein, S., Gaetani, M., . . . Holben, B. (2019). The Aerosols, Radiation and Clouds in Southern Africa Field Campaign in Namibia: Overview, Illustrative Observations, and Way Forward. *Bulletin of the American Meteorological Society*, *100*(7), 1277-1298. https://doi.org/10.1175/bams-d-17-0278.1

Fountoukis, C., & Nenes, A. (2005). Continued development of a cloud droplet formation parameterization for global climate models. *Journal of Geophysical Research: Atmospheres*, *110*(D11). https://doi.org/https://doi.org/10.1029/2004JD005591

Ghan, S. J., & Schwartz, S. E. (2007). Aerosol Properties and Processes: A Path from Field and Laboratory Measurements to Global Climate Models. *Bulletin of the American Meteorological Society*, *88*(7), 1059-1084. https://doi.org/10.1175/bams-88-7-1059

Gibson, E. R., Hudson, P. K., & Grassian, V. H. (2006). Physicochemical Properties of Nitrate Aerosols: Implications for the Atmosphere. *The Journal of Physical Chemistry A*, *110*(42), 11785-11799. https://doi.org/10.1021/jp063821k

Giglio, L., van der Werf, G. R., Randerson, J. T., Collatz, G. J., & Kasibhatla, P. (2006). Global estimation of burned area using MODIS active fire observations. *Atmos. Chem. Phys.*, *6*(4), 957-974. https://doi.org/10.5194/acp-6-957-2006

Giles, D. M., Sinyuk, A., Sorokin, M. G., Schafer, J. S., Smirnov, A., Slutsker, I., Eck, T. F., Holben, B. N., Lewis, J. R., Campbell, J. R., Welton, E. J., Korkin, S. V., & Lyapustin, A. I. (2019). Advancements in the Aerosol Robotic Network (AERONET) Version 3 database – automated near-real-time quality control algorithm with improved cloud screening for Sun photometer aerosol optical depth (AOD) measurements. *Atmos. Meas. Tech.*, *12*(1), 169-209. https://doi.org/10.5194/amt-12-169-2019

Glotfelty, T., Alapaty, K., He, J., Hawbecker, P., Song, X., & Zhang, G. (2019). The Weather Research and Forecasting Model with Aerosol–Cloud Interactions (WRF-ACI): Development, Evaluation, and Initial Application. *Monthly Weather Review*, *147*(5), 1491-1511. https://doi.org/10.1175/mwr-d-18-0267.1

Granier, C., Bessagnet, B., Bond, T., D'Angiola, A., Denier van der Gon, H., Frost, G. J., Heil, A., Kaiser, J. W., Kinne, S., Klimont, Z., Kloster, S., Lamarque, J.-F., Liousse, C., Masui, T., Meleux, F., Mieville, A., Ohara, T., Raut, J.-C., Riahi, K., . . . van Vuuren, D. P. (2011). Evolution of anthropogenic and biomass burning emissions of air pollutants at global and regional scales during the 1980–2010 period. *Climatic Change*, *109*(1), 163. https://doi.org/10.1007/s10584-011-0154-1

Grell, G. A., Peckham, S. E., Schmitz, R., McKeen, S. A., Frost, G., Skamarock, W. C., & Eder, B. (2005). Fully coupled "online" chemistry within the WRF model. *Atmospheric Environment*, *39*(37), 6957-6975. https://doi.org/https://doi.org/10.1016/j.atmosenv.2005.04.027

Hansen, J., Sato, M., & Ruedy, R. (1997). Radiative forcing and climate response. *Journal of Geophysical Research: Atmospheres*, *102*(D6), 6831-6864. https://doi.org/https://doi.org/10.1029/96JD03436

Haywood, J., & Boucher, O. (2000). Estimates of the direct and indirect radiative forcing due to tropospheric aerosols: A review. *Reviews of Geophysics*, *38*(4), 513-543. https://doi.org/https://doi.org/10.1029/1999RG000078

Haywood, J. M., Abel, S. J., Barrett, P. A., Bellouin, N., Blyth, A., Bower, K. N., Brooks, M., Carslaw, K., Che, H., Coe, H., Cotterell, M. I., Crawford, I., Cui, Z., Davies, N., Dingley, B., Field, P., Formenti, P., Gordon, H., de Graaf, M., . . . Zuidema, P. (2021). The CLoud–Aerosol–Radiation Interaction and Forcing: Year 2017 (CLARIFY-2017) measurement campaign. *Atmos. Chem. Phys.*, *21*(2), 1049-1084. https://doi.org/10.5194/acp-21-1049-2021

Haywood, J. M., Osborne, S. R., Francis, P. N., Keil, A., Formenti, P., Andreae, M. O., & Kaye, P. H. (2003). The mean physical and optical properties of regional haze dominated by biomass burning aerosol measured from the C-130 aircraft during SAFARI 2000. *Journal of Geophysical Research: Atmospheres*, *108*(D13). https://doi.org/https://doi.org/10.1029/2002JD002226

Holanda, B. A., Pöhlker, M. L., Walter, D., Saturno, J., Sörgel, M., Ditas, J., Ditas, F., Schulz, C., Franco, M. A., Wang, Q., Donth, T., Artaxo, P., Barbosa, H. M. J., Borrmann, S., Braga,

R., Brito, J., Cheng, Y., Dollner, M., Kaiser, J. W., . . . Pöhlker, C. (2020). Influx of African biomass burning aerosol during the Amazonian dry season through layered transatlantic transport of black carbon-rich smoke. *Atmos. Chem. Phys.*, *20*(8), 4757-4785. https://doi.org/10.5194/acp-20-4757-2020

Holben, B. N. (1998). AERONET—A Federated Instrument Network and Data Archive for Aerosol Characterization. *Remote Sensing of Environment*, *66*, 1-16.

Hopkins, R. J., Lewis, K., Desyaterik, Y., Wang, Z., Tivanski, A. V., Arnott, W. P., Laskin, A., & Gilles, M. K. (2007). Correlations between optical, chemical and physical properties of biomass burn aerosols. *Geophysical Research Letters*, *34*(18). https://doi.org/https://doi.org/10.1029/2007GL030502

Jacobson, M. Z. (2002). Control of fossil-fuel particulate black carbon and organic matter, possibly the most effective method of slowing global warming. *Journal of Geophysical Research: Atmospheres*, *107*(D19), ACH 16-11-ACH 16-22. https://doi.org/https://doi.org/10.1029/2001JD001376

Junge, C. E. (1958). Atmospheric Chemistry. In H. E. Landsberg & J. Van Mieghem (Eds.), *Advances in Geophysics* (Vol. 4, pp. 1-108). Elsevier. https://doi.org/https://doi.org/10.1016/S0065-2687(08)60484-7

Kanakidou, M. (2013). Atmospheric Aerosols and Climate Impacts. In *Aerosol Science* (pp. 181-206). https://doi.org/https://doi.org/10.1002/9781118682555.ch8

Kaufman, Y. J., Tanré, D., & Boucher, O. (2002). A satellite view of aerosols in the climate system. *Nature*, *419*(6903), 215-223. https://doi.org/10.1038/nature01091

Koch, D., & Delgenio, A. (2010). Black carbon semi-direct effects on cloud cover: Review and synthesis. *Atmospheric Chemistry and Physics*, *10*. https://doi.org/10.5194/acp-10-7685-2010

Köhler, H. (1936). The nucleus in and the growth of hygroscopic droplets [10.1039/TF9363201152]. *Transactions of the Faraday Society*, *32*(0), 1152-1161. https://doi.org/10.1039/TF9363201152

Kommalapati, R. R., & Valsaraj, K. T. (2009). Atmospheric Aerosols and Their Importance. In *Atmospheric Aerosols* (Vol. 1005, pp. 1-10). American Chemical Society. https://doi.org/doi:10.1021/bk-2009-1005.ch001

10.1021/bk-2009-1005.ch001

Konovalov, I. B., Golovushkin, N. A., Beekmann, M., & Andreae, M. O. (2021). Insights into the aging of biomass burning aerosol from satellite observations and 3D atmospheric modeling: evolution of the aerosol optical properties in Siberian wildfire plumes. *Atmos. Chem. Phys.*, *21*(1), 357-392. https://doi.org/10.5194/acp-21-357-2021

Laskin, A., Laskin, J., & Nizkorodov, S. A. (2015). Chemistry of Atmospheric Brown Carbon. *Chemical Reviews*, *115*(10), 4335-4382. https://doi.org/10.1021/cr5006167

Leahy, L. V., Anderson, T. L., Eck, T. F., & Bergstrom, R. W. (2007). A synthesis of single scattering albedo of biomass burning aerosol over southern Africa during SAFARI 2000. *Geophysical Research Letters*, *34*(12). https://doi.org/https://doi.org/10.1029/2007GL029697

LeBlanc, S. E., Pilewskie, P., Schmidt, K. S., & Coddington, O. (2015). A spectral method for discriminating thermodynamic phase and retrieving cloud optical thickness and effective

radius using transmitted solar radiance spectra. *Atmos. Meas. Tech.*, *8*(3), 1361-1383. https://doi.org/10.5194/amt-8-1361-2015

LeBlanc, S. E., Redemann, J., Flynn, C., Pistone, K., Kacenelenbogen, M., Segal-Rosenheimer, M., Shinozuka, Y., Dunagan, S., Dahlgren, R. P., Meyer, K., Podolske, J., Howell, S. G., Freitag, S., Small-Griswold, J., Holben, B., Diamond, M., Wood, R., Formenti, P., Piketh, S., . . . Namwoonde, A. (2020). Above-cloud aerosol optical depth from airborne observations in the southeast Atlantic. *Atmos. Chem. Phys.*, *20*(3), 1565-1590. https://doi.org/10.5194/acp-20-1565-2020

Lee, H. J., Aiona, P. K., Laskin, A., Laskin, J., & Nizkorodov, S. A. (2014). Effect of Solar Radiation on the Optical Properties and Molecular Composition of Laboratory Proxies of Atmospheric Brown Carbon. *Environmental Science & Technology*, *48*(17), 10217-10226. https://doi.org/10.1021/es502515r

Levy, R. C., Remer, L. A., & Dubovik, O. (2007). Global aerosol optical properties and application to Moderate Resolution Imaging Spectroradiometer aerosol retrieval over land. *Journal of Geophysical Research: Atmospheres*, *112*(D13). https://doi.org/https://doi.org/10.1029/2006JD007815

Li, J., Ge, X., He, Q., & Abbas, A. (2021). Aerosol optical depth (AOD): spatial and temporal variations and association with meteorological covariates in Taklimakan desert, China. *PeerJ*, *9*, e10542. https://doi.org/10.7717/peerj.10542

Lim, K.-S. S., Fan, J., Leung, L. R., Ma, P.-L., Singh, B., Zhao, C., Zhang, Y., Zhang, G., & Song, X. (2014). Investigation of aerosol indirect effects using a cumulus microphysics parameterization in a regional climate model. *Journal of Geophysical Research: Atmospheres*, *119*(2), 906-926. https://doi.org/https://doi.org/10.1002/2013JD020958

Lin, Y.-C., Yu, M., Xie, F., & Zhang, Y. (2022). Anthropogenic Emission Sources of Sulfate Aerosols in Hangzhou, East China: Insights from Isotope Techniques with Consideration of Fractionation Effects between Gas-to-Particle Transformations. *Environmental Science & Technology*, *56*(7), 3905-3914. https://doi.org/10.1021/acs.est.1c05823

Liu, J., Zheng, Y., Li, Z., Flynn, C., & Cribb, M. (2012). Seasonal variations of aerosol optical properties, vertical distribution and associated radiative effects in the Yangtze Delta region of China. *Journal of Geophysical Research: Atmospheres*, *117*(D16), n/a-n/a. https://doi.org/10.1029/2011jd016490

Luo, J., Zhang, Y., & Zhang, Q. (2020). The Ångström Exponent and Single-Scattering Albedo of Black Carbon: Effects of Different Coating Materials. *Atmosphere*, *11*(10), 1103. https://www.mdpi.com/2073-4433/11/10/1103

Ma, P.-L., Rasch, P. J., Fast, J. D., Easter, R. C., Gustafson Jr, W., Liu, X., Ghan, S. J., & Singh, B. (2014). Assessing the CAM5 physics suite in the WRF-Chem model: Implementation, resolution sensitivity, and a first evaluation for a regional case study. *Geoscientific Model Development*, *7*(3), 755-778.

Mallet, M., Solmon, F., Nabat, P., Elguindi, N., Waquet, F., Bouniol, D., Sayer, A. M., Meyer, K., Roehrig, R., Michou, M., Zuidema, P., Flamant, C., Redemann, J., & Formenti, P. (2020). Direct and semi-direct radiative forcing of biomass-burning aerosols over the southeast Atlantic (SEA) and its sensitivity to absorbing properties: a regional climate modeling study. *Atmos. Chem. Phys.*, *20*(21), 13191-13216. https://doi.org/10.5194/acp-20-13191-2020

Mayer, H. (1999). Air pollution in cities. *Atmospheric Environment*, *33*(24), 4029-4037. https://doi.org/https://doi.org/10.1016/S1352-2310(99)00144-2

McMurry, P. H. (2003). AEROSOLS | Observations and Measurements. In J. R. Holton (Ed.), *Encyclopedia of Atmospheric Sciences* (pp. 20-34). Academic Press. https://doi.org/https://doi.org/10.1016/B0-12-227090-8/00048-8

Moosmüller, H., Engelbrecht, J. P., Skiba, M., Frey, G., Chakrabarty, R. K., & Arnott, W. P. (2012). Single scattering albedo of fine mineral dust aerosols controlled by iron concentration. *Journal of Geophysical Research: Atmospheres*, *117*(D11). https://doi.org/https://doi.org/10.1029/2011JD016909

Morrison, H., & Gettelman, A. (2008). A New Two-Moment Bulk Stratiform Cloud Microphysics Scheme in the Community Atmosphere Model, Version 3 (CAM3). Part I: Description and Numerical Tests. *Journal of Climate*, *21*(15), 3642-3659. https://doi.org/10.1175/2008jcli2105.1

Nascimento, J. P., Bela, M. M., Meller, B. B., Banducci, A. L., Rizzo, L. V., Vara-Vela, A. L., Barbosa, H. M. J., Gomes, H., Rafee, S. A. A., Franco, M. A., Carbone, S., Cirino, G. G., Souza, R. A. F., McKeen, S. A., & Artaxo, P. (2021). Aerosols from anthropogenic and biogenic sources and their interactions – modeling aerosol formation, optical properties, and impacts over the central Amazon basin. *Atmos. Chem. Phys.*, *21*(9), 6755-6779. https://doi.org/10.5194/acp-21-6755-2021

Nel, A. (2005). Air Pollution-Related Illness: Effects of Particles. *Science*, *308*(5723), 804-806. https://doi.org/doi:10.1126/science.1108752

Nichols, J. L., Owens, E. O., Dutton, S. J., & Luben, T. J. (2013). Systematic review of the effects of black carbon on cardiovascular disease among individuals with pre-existing disease. *International Journal of Public Health*, *58*(5), 707-724. https://doi.org/10.1007/s00038-013-0492-z

Niemand, M., Möhler, O., Vogel, B., Vogel, H., Hoose, C., Connolly, P., Klein, H., Bingemer, H., DeMott, P., Skrotzki, J., & Leisner, T. (2012). A Particle-Surface-Area-Based Parameterization of Immersion Freezing on Desert Dust Particles. *Journal of the Atmospheric Sciences*, *69*(10), 3077-3092. https://doi.org/10.1175/jas-d-11-0249.1

Pilinis, C., & Pandis, S. N. (1995). Physical, Chemical and Optical Properties of Atmospheric Aerosols. In T. Kouimtzis & C. Samara (Eds.), *Airborne Particulate Matter* (pp. 99-124). Springer Berlin Heidelberg. https://doi.org/10.1007/978-3-540-49145-3_4

Pistone, K., Redemann, J., Doherty, S., Zuidema, P., Burton, S., Cairns, B., Cochrane, S., Ferrare, R., Flynn, C., Freitag, S., Howell, S. G., Kacenelenbogen, M., LeBlanc, S., Liu, X., Schmidt, K. S., Sedlacek Iii, A. J., Segal-Rozenhaimer, M., Shinozuka, Y., Stamnes, S., . . . Xu, F. (2019). Intercomparison of biomass burning aerosol optical properties from in situ and remote-sensing instruments in ORACLES-2016. *Atmos. Chem. Phys.*, *19*(14), 9181-9208. https://doi.org/10.5194/acp-19-9181-2019

Pöschl, U. (2005). Atmospheric Aerosols: Composition, Transformation, Climate and Health Effects. *Angewandte Chemie International Edition*, *44*(46), 7520-7540. https://doi.org/https://doi.org/10.1002/anie.200501122

Rajesh, T. A., & Ramachandran, S. (2020). Extensive and intensive properties of aerosol over distinct environments: Influence of anthropogenic emissions and meteorology. *Journal of Atmospheric and Solar-Terrestrial Physics*, *202*, 105223. https://doi.org/https://doi.org/10.1016/j.jastp.2020.105223

Ramachandran, S. (2018). *Atmospheric Aerosols: Characteristics and Radiative Effects*. CRC Press. https://doi.org/10.1201/9781315152400

Ramanathan, V., Crutzen, P. J., Kiehl, J. T., & Rosenfeld, D. (2001). Aerosols, Climate, and the Hydrological Cycle. *Science*, *294*(5549), 2119-2124. https://doi.org/doi:10.1126/science.1064034

Ramaswamy, V., Boucher, O., Haigh, J., Hauglustaine, D., Haywood, J., Myhre, G., Nakajima, T., Shi, G. Y., & Solomon, S. (Eds.). (2001). *Radiative forcing of climate change* (Vol. 18). Cambridge University Press. http://www.ipcc.ch/ipccreports/tar/wg1/pdf/TAR-06.PDF.

Ramo, R., Roteta, E., Bistinas, I., van Wees, D., Bastarrika, A., Chuvieco, E., & van der Werf, G. R. (2021). African burned area and fire carbon emissions are strongly impacted by small fires undetected by coarse resolution satellite data. *Proc Natl Acad Sci U S A*, *118*(9). https://doi.org/10.1073/pnas.2011160118

Redemann, J., Wood, R., Zuidema, P., Doherty, S. J., Luna, B., LeBlanc, S. E., Diamond, M. S., Shinozuka, Y., Chang, I. Y., Ueyama, R., Pfister, L., Ryoo, J. M., Dobracki, A. N., da Silva, A. M., Longo, K. M., Kacenelenbogen, M. S., Flynn, C. J., Pistone, K., Knox, N. M., . . . Gao, L. (2021). An overview of the ORACLES (ObseRvations of Aerosols above CLouds and their intEractionS) project: aerosol–cloud–radiation interactions in the southeast Atlantic basin. *Atmos. Chem. Phys.*, *21*(3), 1507-1563. https://doi.org/10.5194/acp-21-1507-2021

Reid, J. S., Jonsson, H. H., Smith, M. H., & Smirnov, A. (2001). Evolution of the vertical profile and flux of large sea-salt particles in a coastal zone. *Journal of Geophysical Research: Atmospheres*, *106*(D11), 12039-12053. https://doi.org/https://doi.org/10.1029/2000JD900848

Remer, L. A., Kaufman, Y. J., Tanré, D., Mattoo, S., Chu, D. A., Martins, J. V., Li, R.-R., Ichoku, C., Levy, R. C., Kleidman, R. G., Eck, T. F., Vermote, E., & Holben, B. N. (2005). The MODIS Aerosol Algorithm, Products, and Validation. *Journal of the Atmospheric Sciences*, *62*(4), 947-973. https://doi.org/https://doi.org/10.1175/JAS3385.1

Rosenfeld, D. (1999). TRMM observed first direct evidence of smoke from forest fires inhibiting rainfall. *Geophysical Research Letters*, *26*(20), 3105-3108. https://doi.org/https://doi.org/10.1029/1999GL006066

Russell, P. B., Redemann, J., Schmid, B., Bergstrom, R. W., Livingston, J. M., McIntosh, D. M., Ramirez, S. A., Hartley, S., Hobbs, P. V., Quinn, P. K., Carrico, C. M., Rood, M. J., Öström, E., Noone, K. J., von Hoyningen-Huene, W., & Remer, L. (2002). Comparison of Aerosol Single Scattering Albedos Derived by Diverse Techniques in Two North Atlantic Experiments. *Journal of the Atmospheric Sciences*, *59*(3), 609-619. https://doi.org/10.1175/1520-0469(2002)059<0609:Coassa>2.0.Co;2

Ryoo, J. M., Pfister, L., Ueyama, R., Zuidema, P., Wood, R., Chang, I., & Redemann, J. (2021). A meteorological overview of the ORACLES (ObseRvations of Aerosols above CLouds and their intEractionS) campaign over the southeastern Atlantic during 2016–2018: Part 1 – Climatology. *Atmos. Chem. Phys.*, *21*(22), 16689-16707. https://doi.org/10.5194/acp-21-16689-2021

Sa'id, R. S., & Garba, S. (2018). Interpolation for Aerosol Optical Depth at Four Wavelengths over Ilorin from Observed Aeronet Data. *IOP Conference Series: Earth and Environmental Science*, *173*(1), 012014. https://doi.org/10.1088/1755-1315/173/1/012014

Saide, P. E., Thompson, G., Eidhammer, T., da Silva, A. M., Pierce, R. B., & Carmichael, G. R. (2016). Assessment of biomass burning smoke influence on environmental conditions for

multi-year tornado outbreaks by combining aerosol-aware microphysics and fire emission constraints. *J Geophys Res Atmos*, *121*(17), 10294-10311. https://doi.org/10.1002/2016JD025056

Sakaeda, N., Wood, R., & Rasch, P. J. (2011). Direct and semidirect aerosol effects of southern African biomass burning aerosol. *Journal of Geophysical Research: Atmospheres*, *116*(D12). https://doi.org/https://doi.org/10.1029/2010JD015540

Santer, B. D., Taylor, K. E., Wigley, T. M. L., Johns, T. C., Jones, P. D., Karoly, D. J., Mitchell, J. F. B., Oort, A. H., Penner, J. E., Ramaswamy, V., Schwarzkopf, M. D., Stouffer, R. J., & Tett, S. (1996). A search for human influences on the thermal structure of the atmosphere. *Nature*, *382*(6586), 39-46. https://doi.org/10.1038/382039a0

Schepanski, K. (2018). Transport of Mineral Dust and Its Impact on Climate. *Geosciences*, *8*(5), 151. https://www.mdpi.com/2076-3263/8/5/151

Schmid, B., Michalsky, J., Halthore, R., Beauharnois, M., Harrison, L., Livingston, J., Russell, P., Holben, B., Eck, T., & Smirnov, A. (1999). Comparison of aerosol optical depth from four solar radiometers during the Fall 1997 ARM Intensive Observation Period. *Geophysical Research Letters*, *26*, 2725-2728. https://doi.org/10.1029/1999GL900513

Schuster, G. L., Dubovik, O., & Holben, B. N. (2006). Angstrom exponent and bimodal aerosol size distributions. *Journal of Geophysical Research: Atmospheres*, *111*(D7). https://doi.org/https://doi.org/10.1029/2005JD006328

Sedlacek, A. J., III, Lewis, E. R., Onasch, T. B., Zuidema, P., Redemann, J., Jaffe, D., & Kleinman, L. I. (2022). Using the Black Carbon Particle Mixing State to Characterize the Lifecycle of Biomass Burning Aerosols. *Environmental Science & Technology*, *56*(20), 14315-14325. https://doi.org/10.1021/acs.est.2c03851

Segal-Rosenheimer, M., Russell, P. B., Schmid, B., Redemann, J., Livingston, J. M., Flynn, C. J., Johnson, R. R., Dunagan, S. E., Shinozuka, Y., Herman, J., Cede, A., Abuhassan, N., Comstock, J. M., Hubbe, J. M., Zelenyuk, A., & Wilson, J. (2014). Tracking elevated pollution layers with a newly developed hyperspectral Sun/Sky spectrometer (4STAR): Results from the TCAP 2012 and 2013 campaigns. *Journal of Geophysical Research: Atmospheres*, *119*(5), 2611-2628. https://doi.org/https://doi.org/10.1002/2013JD020884

Seidel, D. J., Ao, C. O., & Li, K. (2010). Estimating climatological planetary boundary layer heights from radiosonde observations: Comparison of methods and uncertainty analysis. *Journal of Geophysical Research: Atmospheres*, *115*(D16). https://doi.org/https://doi.org/10.1029/2009JD013680

Shinozuka, Y., Saide, P. E., Ferrada, G. A., Burton, S. P., Ferrare, R., Doherty, S. J., Gordon, H., Longo, K., Mallet, M., Feng, Y., Wang, Q., Cheng, Y., Dobracki, A., Freitag, S., Howell, S. G., LeBlanc, S., Flynn, C., Segal-Rosenhaimer, M., Pistone, K., . . . Zuidema, P. (2020). Modeling the smoky troposphere of the southeast Atlantic: a comparison to ORACLES airborne observations from September of 2016. *Atmos. Chem. Phys.*, *20*(19), 11491-11526. https://doi.org/10.5194/acp-20-11491-2020

Sinyuk, A., Holben, B. N., Eck, T. F., Giles, D. M., Slutsker, I., Korkin, S., Schafer, J. S., Smirnov, A., Sorokin, M., & Lyapustin, A. (2020). The AERONET Version 3 aerosol retrieval algorithm, associated uncertainties and comparisons to Version 2. *Atmos. Meas. Tech.*, *13*(6), 3375-3411. https://doi.org/10.5194/amt-13-3375-2020

Song, X., & Zhang, G. J. (2011). Microphysics parameterization for convective clouds in a global climate model: Description and single-column model tests. *Journal of Geophysical Research: Atmospheres*, *116*(D2). https://doi.org/https://doi.org/10.1029/2010JD014833

Stier, P., Schutgens, N. A. J., Bellouin, N., Bian, H., Boucher, O., Chin, M., Ghan, S., Huneeus, N., Kinne, S., Lin, G., Ma, X., Myhre, G., Penner, J. E., Randles, C. A., Samset, B., Schulz, M., Takemura, T., Yu, F., Yu, H., & Zhou, C. (2013). Host model uncertainties in aerosol radiative forcing estimates: results from the AeroCom Prescribed intercomparison study. *Atmos. Chem. Phys.*, *13*(6), 3245-3270. https://doi.org/10.5194/acp-13-3245-2013

Takemura, T. (2020). Return to different climate states by reducing sulphate aerosols under future CO2 concentrations. *Scientific Reports*, *10*(1), 21748. https://doi.org/10.1038/s41598-020-78805-1

Tang, I. N., Tridico, A. C., & Fung, K. H. (1997). Thermodynamic and optical properties of sea salt aerosols. *Journal of Geophysical Research*, *102*, 23269-23275.

Tariq, S., Qayyum, F., Ul-Haq, Z., & Mehmood, U. (2022). Long-term spatiotemporal trends in aerosol optical depth and its relationship with enhanced vegetation index and meteorological parameters over South Asia. *Environmental Science and Pollution Research*, *29*(20), 30638-30655. https://doi.org/10.1007/s11356-021-17887-4

Thompson, G., & Eidhammer, T. (2014). A Study of Aerosol Impacts on Clouds and Precipitation Development in a Large Winter Cyclone. *Journal of the Atmospheric Sciences*, *71*(10), 3636-3658. https://doi.org/10.1175/jas-d-13-0305.1

Tomasi, C., & Lupi, A. (2017). Primary and Secondary Sources of Atmospheric Aerosol. In *Atmospheric Aerosols* (pp. 1-86). https://doi.org/https://doi.org/10.1002/9783527336449.ch1

Trenberth, K. E., Fasullo, J. T., & Kiehl, J. (2009). Earth's Global Energy Budget. *Bulletin of the American Meteorological Society*, *90*(3), 311-324. https://doi.org/10.1175/2008bams2634.1

Turpin, B. J., Huntzicker, J. J., Larson, S. M., & Cass, G. R. (1991). Los Angeles summer midday particulate carbon: primary and secondary aerosol. *Environmental Science & Technology*, *25*(10), 1788-1793.

Twomey, S. (1974). Pollution and the planetary albedo. *Atmospheric Environment (1967)*, *8*(12), 1251-1256. https://doi.org/https://doi.org/10.1016/0004-6981(74)90004-3

Twomey, S. (1977). The Influence of Pollution on the Shortwave Albedo of Clouds. *Journal of Atmospheric Sciences*, *34*(7), 1149-1152. https://doi.org/10.1175/1520-0469(1977)034<1149:Tiopot>2.0.Co;2

Val Martin, M., Logan, J. A., Kahn, R. A., Leung, F. Y., Nelson, D. L., & Diner, D. J. (2010). Smoke injection heights from fires in North America: analysis of 5 years of satellite observations. *Atmos. Chem. Phys.*, *10*(4), 1491-1510. https://doi.org/10.5194/acp-10-1491-2010

van der Werf, G. R., Randerson, J. T., Giglio, L., Collatz, G. J., Mu, M., Kasibhatla, P. S., Morton, D. C., DeFries, R. S., Jin, Y., & van Leeuwen, T. T. (2010). Global fire emissions and the contribution of deforestation, savanna, forest, agricultural, and peat fires (1997–2009). *Atmos. Chem. Phys.*, *10*(23), 11707-11735. https://doi.org/10.5194/acp-10-11707-2010

Vermote, E., Ellicott, E., Dubovik, O., Lapyonok, T., Chin, M., Giglio, L., & Roberts, G. J. (2009). An approach to estimate global biomass burning emissions of organic and black carbon from MODIS fire radiative power. *Journal of Geophysical Research: Atmospheres*, *114*(D18). https://doi.org/https://doi.org/10.1029/2008JD011188

Wang, K., Zhang, Y., Zhang, X., Fan, J., Leung, L. R., Zheng, B., Zhang, Q., & He, K. (2018). Fine-scale application of WRF-CAM5 during a dust storm episode over East Asia:

Sensitivity to grid resolutions and aerosol activation parameterizations. *Atmospheric Environment*, *176*, 1-20. https://doi.org/https://doi.org/10.1016/j.atmosenv.2017.12.014

Wang, W., Yu, J., Cui, Y., He, J., Xue, P., Cao, W., Ying, H., Gao, W., Yan, Y., Hu, B., Xin, J., Wang, L., Liu, Z., Sun, Y., Ji, D., & Wang, Y. (2018). Characteristics of fine particulate matter and its source in an industrialized coastal city, Ningbo, Yangtze River Delta, China. *Atmos. Res.*, *203*, 105.

Wang, X., Heald, C. L., Sedlacek, A. J., de Sá, S. S., Martin, S. T., Alexander, M. L., Watson, T. B., Aiken, A. C., Springston, S. R., & Artaxo, P. (2016). Deriving brown carbon from multiwavelength absorption measurements: method and application to AERONET and Aethalometer observations. *Atmos. Chem. Phys.*, *16*(19), 12733-12752. https://doi.org/10.5194/acp-16-12733-2016

Waquet, F., Peers, F., Ducos, F., Goloub, P., Platnick, S., Riedi, J., Tanré, D., & Thieuleux, F. (2013). Global analysis of aerosol properties above clouds. *Geophysical Research Letters*, *40*(21), 5809-5814. https://doi.org/https://doi.org/10.1002/2013GL057482

Wood, R. (2012). Stratocumulus Clouds. *Monthly Weather Review*, *140*(8), 2373-2423. https://doi.org/10.1175/mwr-d-11-00121.1

Zaveri, R. A., & Peters, L. K. (1999). A new lumped structure photochemical mechanism for large-scale applications. *Journal of Geophysical Research: Atmospheres*, *104*(D23), 30387-30415. https://doi.org/https://doi.org/10.1029/1999JD900876

Zhang, G. J., & McFarlane, N. A. (1995). Sensitivity of climate simulations to the parameterization of cumulus convection in the Canadian climate centre general circulation model. *Atmosphere-Ocean*, *33*(3), 407-446. https://doi.org/10.1080/07055900.1995.9649539

Zhang, J., & Zuidema, P. (2019). The diurnal cycle of the smoky marine boundary layer observed during August in the remote southeast Atlantic. *Atmos. Chem. Phys.*, *19*(23), 14493-14516. https://doi.org/10.5194/acp-19-14493-2019

Zhang, J., & Zuidema, P. (2021). Sunlight-absorbing aerosol amplifies the seasonal cycle in low-cloud fraction over the southeast Atlantic. *Atmos. Chem. Phys.*, *21*(14), 11179-11199. https://doi.org/10.5194/acp-21-11179-2021

Zhang, Y., Chen, Y., Fan, J., & Leung, L.-Y. R. (2015). Application of an Online-Coupled Regional Climate Model, WRF-CAM5, over East Asia for Examination of Ice Nucleation Schemes: Part II. Sensitivity to Heterogeneous Ice Nucleation Parameterizations and Dust Emissions. *Climate*, *3*(3), 753-774. https://www.mdpi.com/2225-1154/3/3/753

Zhang, Y., Zhang, X., Wang, K., He, J., Leung, L. R., Fan, J., & Nenes, A. (2015). Incorporating an advanced aerosol activation parameterization into WRF-CAM5: Model evaluation and parameterization intercomparison. *Journal of Geophysical Research: Atmospheres*, *120*(14), 6952-6979. https://doi.org/https://doi.org/10.1002/2014JD023051

Zheng, G., Sedlacek, A. J., Aiken, A. C., Feng, Y., Watson, T. B., Raveh-Rubin, S., Uin, J., Lewis, E. R., & Wang, J. (2020). Long-range transported North American wildfire aerosols observed in marine boundary layer of eastern North Atlantic. *Environment International*, *139*, 105680. https://doi.org/https://doi.org/10.1016/j.envint.2020.105680

Zuidema, P., Redemann, J., Haywood, J., Wood, R., Piketh, S., Hipondoka, M., & Formenti, P. (2016). Smoke and Clouds above the Southeast Atlantic: Upcoming Field Campaigns Probe Absorbing Aerosol's Impact on Climate. *Bulletin of the American Meteorological Society*, *97*(7), 1131-1135. https://doi.org/10.1175/bams-d-15-00082.1

Zuidema, P., Sedlacek III, A. J., Flynn, C., Springston, S., Delgadillo, R., Zhang, J., Aiken, A. C., Koontz, A., & Muradyan, P. (2018). The Ascension Island Boundary Layer in the Remote Southeast Atlantic is Often Smoky. *Geophysical Research Letters*, *45*(9), 4456-4465. https://doi.org/https://doi.org/10.1002/2017GL076926